Transport and Chemical Phenomena in a Solar Thermochemical Reactor to Split Carbon Dioxide and Water to Produce Synthesis Gas

A Dissertation

SUBMITTED TO THE FACULTY OF
UNIVERSITY OF MINNESOTA
BY

Rohini Bala Chandran

IN PARTIAL FULFILLMENT OF THE REQUIREMENTS
FOR THE DEGREE OF
DOCTOR OF PHILOSOPHY

Dr. Jane H. Davidson, Advisor

October 2015

Acknowledgements

I owe my deepest gratitude to my advisor, Prof. Jane H. Davidson, for her expert academic guidance, encouragement and support. Her infectious curiosity and quest for clarity has made me push my own boundaries and significantly improved my scholarship as a researcher, a writer and a speaker. Thank you Jane, for facilitating the best graduate school experience that I could have hoped for.

I express my greatest appreciation to Prof. Thomas R. Chase for collaborating on this project. His meticulous and careful problem solving approach has taught me a great deal about solving design problems. I thank Prof. Wojciech Lipinski for recruiting me on this project and providing the initial guidance in my research. I am grateful to Prof. Francis A. Kulacki for taking interest in my graduate and professional career.

This research was made possible by the computing resources provided by Minnesota Supercomputing Institute at the University of Minnesota and I am grateful for that. I acknowledge the financial support by the U.S. Department of Energy's Advanced Research Projects Agency—Energy (DOE ARPA-E, award no. DE-AR0000182) to the University of Minnesota and the Doctoral Dissertation Fellowship from the University of Minnesota.

Many thanks are due to the researchers of the Solar Energy Laboratory for the constructive discussions and criticisms. Special thanks to Stephen Sedler for providing me with the reactor figures in this dissertation and for being great company in ME 301. I am very thankful to my officemates and ARPAE comrades—Stephen Sedler, Peter

Krenzke, Daniel Thomas, Brandon Hathaway, Adam Gladen, Robert Smith, Aayan Banerjee, Luke Venstrom, Daniel Keene, and Lindsey Yue for being sounding boards and wonderful colleagues.

I am lucky to have made precious friends in school—Ranga, Durbha, Meenakshi, Shruthi, Thaseem, Savio, Aditi, Praggy, Thavil, Raja, Janani and Aswin, to share the assignments, the bike rides, the coffees, the good and the bad times. Special shout out to Aruna, Jomes and KP for lending ears at crisis times.

I am extremely grateful to my parents and grandparents for nurturing me with unconditional affection and good education. I can't be thankful enough for the enormous encouragement from Ram, Asha, the "Besant Nagar" extended family and my in-laws.

Finally and most importantly, I want to thank Piyush, my best friend, my better half and my rock. The last few years wouldn't have been as delightful without you. Your incredible patience, love and companionship throughout my graduate studies will never be forgotten.

Dedication

To all my teachers for inspiring me in countless ways.

To Amma, Appa, Patti and Thatha, for the innumerable sacrifices they've made.

Abstract

Numerical study of a solar thermochemical reactor for isothermal reduction and oxidation of cerium dioxide is presented with the goal of accomplishing effective gas phase heat recovery and efficient gas utilization — the two most important attributes for achieving high fuel conversion efficiency in the reactor. Models were applied in tandem with and/or compared to experiments to interpret physical processes in the reactor and for validation.

To achieve gas phase heat recuperation, a counterflow, ceramic heat exchanger filled with alumina reticulated porous ceramic was designed to operate at 1773 K. The focus of the modeling was selection of the morphology of the reticulated porous ceramic/ foam to balance heat transfer and pressure drop. Foam morphologies of 5–30 pores per inch (PPI) with porosities of 65–90% were considered. Large pore sizes, or equivalently low PPI, augment radiative penetration and reduce pressure drop. Solid phase conduction is the dominant mode of heat transfer over a majority of the heat exchanger length. Consequently, lower porosity improves the overall heat exchange at the penalty of increased pressure drop. The tradeoff in heat transfer performance and pressure drop point to use of higher porosity, 85–90%, and large pore sizes to optimize the solar-to-fuel efficiency. The final design is a 1.4 m long heat exchanger filled with 10 and 5 PPI, 85% porous, alumina foam in the annulus and center tube. This design recuperates more than 90% of the sensible energy of the reactant and product gases with less than 15 kPa pressure drop through the bed of ceria and heat exchanger.

Motivated by the need to investigate the influence of transport processes on reactor performance, especially on the temperature distribution and the reaction rates, a transient, three-dimensional computational model of the reactor was developed. A hybrid Monte Carlo/finite volume approach was used to model radiative transport in the reactor surfaces and in the participating media. The chemical kinetics of the cyclic, gas-solid reactions were modeled by obtaining the best fit reaction rate coefficients from global rate data from a bench top reactor at 1773 K. For a solar input of 4.2 kW and gas flow rates of 0.67×10^{-4} mol s^{-1} g_{ceria}^{-1}, the model predicts nearly isothermal cycling at an average temperature of 1791 K. Results elucidate that spatial variations in temperature, species concentration and reaction rate are interrelated and more pronounced along the gas flow direction. Carbon monoxide is produced continuously at 3.6×10^{-4} mol s^{-1}, translating to 100 W of stored chemical energy. The overall reaction rates are driven by gas phase advection and the intrinsic material thermodynamics, rather than surface kinetics.

The numerical modeling framework developed in this dissertation is robust and conducive to study other thermochemical processes in a high temperature solar reactor.

Contents

List of Tables

List of Figures

Nomenclature

Symbols

a	specific surface area, $m^2\ m^{-3}$
A	pre-exponential factor, s^{-1} or area, m^2
C	Concentration ratio
C_E	Ergun coefficient, m^{-1}
d	diameter, m
D	mass diffusivity, $m^2\ s^{-1}$
E	activation energy, kJ $mol^{-1}\ K^{-1}$
F_L	heat loss fraction
G	incident radiation in a control volume, W m^{-2}
$\overline{h}$	molar enthalpy, J mol^{-1}
h	enthalpy, J kg^{-1}
HHV	higher heating value, J mol^{-1}
I	radiation intensity, W $m^{-2}\ sr^{-1}$
I_b	black body radiation, W m^{-2}
k_{ox}	oxidation rate constant, $mol_O\ mol_{ceria}^{-1}\ s^{-1}$
k_{d,CO_2}	dissociation rate constant, $mol_{CO}\ mol_{ceria}^{-1}\ s^{-1}$
k	thermal conductivity, W $m^{-1}\ K^{-1}$
K	permeability, m^2 or equilibrium constant
L	length, m
M	molecular mass, kg mol^{-1}
$\dot{m}$	mass flow rate, kg s^{-1}
n	reaction order
$\dot{n}$	molar flow rate, mol s^{-1}
$\hat{n}$	unit normal vector
Pe	Peclet Number, $\frac{U_{avg}L}{D_{i,eff}}$
p	pressure, Pa
q''	heat flux, W m^{-2}
q_{solar}	solar input power per unit mass of ceria, W g^{-1}
$\boldsymbol{q}$	heat flux vector, W m^{-2}
$\dot{Q}$	power, W
Re	Reynolds number
R_u	universal rate constant, J $mol^{-1}\ K^{-1}$
r	radial position, m or mm
$\dot{r}$	volumetric mass source/sink, kg $m^{-3}\ s^{-1}$
$\hat{r}, \hat{s}$	direction vectors
S_m'''	momentum source, kg $m^{-2}\ s^{-1}$
S_q'''	energy source term, W m^{-3}
$\dot{S}$	energy source, W m^{-3}

T	temperature, K
t	time, s
$\boldsymbol{u}$	velocity vector, m s^{-1}
U	overall heat loss coefficient, W m^{-2} K^{-1}
V	volume, m^3
X	species mole fraction
Y	species mass fraction
z	axial coordinate, m

Greek

β	extinction coefficient [m^{-1}]
δ	ceria nonstoichiometery
ε	heat exchanger effectiveness
η	efficiency
κ	absorption coefficient, m^{-1}
ω	scattering albedo
ϕ	porosity
Φ	scattering phase function
μ	viscosity , kg m^{-1} s^{-1}
ρ	density, kg m^{-3}
σ	scattering coefficient, m^{-1}
Ω	solid angle, sr
τ	half-cycle time, s
ζ	optical thickness
Γ	surface of a volume, m^2

Subscripts

amb	ambient conditions
bed	ceria bed
c	cold side of the heat exchanger
ceria	ceria material
CeO_2	ceria
chem	heat transfer due to chemical reactions
comp	compressor
d, diss	dissociation reaction of CO_2
eff	effective value of transport properties
eq	equilibrium
f	fluid region or fiber
h	hot side of the heat exchanger
i	general index
in	inlet
ins	insulation
loss	heat losses due to convection and conduction
out	outlet
ox	oxidation half-cycle or oxidizer flow

p	pertaining to particle or pore scale features
particle	single ceria particle
pump	pumping power
rad	radiative heat transfer
rd	reduction half-cycle
ref	reference conditions
rerad	heat losses due to thermal emission from a hot surface
s	solid region
$s \rightarrow E$	solar to electric conversion efficiency
sep	energetic cost of gas separation
sg	pertaining to sweep gas flow
solar	incident solar power
th	thermal
t	pertinent to time
w	wall

Subscripts

$'$	per unit mass of ceria
$\bar{\ }$	over bar indicates time-averaged/area-averaged/bulk mean values

Other

$\langle \ \rangle$	volume-averaged or spatially averaged quantities
CFD	computational fluid dynamic
OD	outer diameter
PPI	pores per inch
HX	heat exchanger
RE	reactive element
RMSE	root mean square error
RPC	reticulate porous ceramic

Chapter 1
Introduction & Background

Developing carbon neutral energy sources is critical to address the global energy challenges of the future and reduce the anthropogenic emissions of greenhouse gases. Petroleum is the largest share, 35% of the world's primary energy consumption followed by natural gas (28%) and coal (25%) [1]. Solar radiation is unmatched in its abundance as a sustainable source of energy, yet intermittent and unevenly distributed. Therefore, we must develop technologies to efficiently capture, store and transport solar energy for large scale and long term consumption. Chemical bonds are one of the most effective mediums of storing energy because of their high energy densities. Green plants make complex hydrocarbons with sunlight, carbon dioxide and water —can we take a *leaf* from nature's book? If we could convert products of fuel combustion back to hydrocarbons with high energy densities, we would also come out even in a global sense.

A particularly promising approach is to use concentrated sunlight to split water and carbon dioxide to produce hydrogen and synthesis gas, a mixture of carbon monoxide and hydrogen via metal oxide redox cycles. Excellent reviews of solar redox cycles are available in recent publications [2–4]. The products can be combusted directly, used in a fuel cell, or further processed to liquid fuels [5,6]. The present study focuses on redox cycles utilizing cerium dioxide (ceria) as an oxygen transfer agent. Ceria can be partially reduced at temperatures greater than 1600 K, which is attainable with concentrated solar power, in a low oxygen partial pressure environment (typically less than 10 Pa),

$$\mathrm{CeO}_{2-\delta_{\mathrm{ox}}} \rightarrow \mathrm{CeO}_{2-\delta_{\mathrm{rd}}} + \frac{\Delta\delta}{2}\mathrm{O}_2 \qquad (1)$$

Under these conditions, Ce^{4+} ions transition to Ce^{3+} defects and create oxygen vacancies to maintain electroneutrality (2:1 ratio for the number of cerium atoms in the 3+ oxidation state to the released oxygen atoms) and concurrently release O_2 [7]. The concentration of the oxygen vacancies created per unit mole of ceria is represented by the nonstoichiometry, δ in eq. (1). Ceria retains its cubic fluorite lattice structure up to nonstoichiometries of 0.25 without melting or phase change [7,8]. Retention of the solid phase facilitates rapid diffusion of oxygen atoms within the ceria lattice and allows for the separation of reaction products from the solid.

$$\mathrm{CeO}_{2-\delta_{\mathrm{rd}}} + \Delta\delta\ \mathrm{H_2O} \rightarrow\ \mathrm{CeO}_{2-\delta_{\mathrm{ox}}} + \Delta\delta\mathrm{H_2} \tag{2a}$$

$$\mathrm{CeO}_{2-\delta_{\mathrm{rd}}} + \Delta\delta\ \mathrm{CO_2} \rightarrow\ \mathrm{CeO}_{2-\delta_{\mathrm{ox}}} + \Delta\delta\ \mathrm{CO} \tag{2b}$$

The reduced ceria when reoxidized with CO_2 and/or H_2O produces CO and/or H_2 via the exothermic[1] reactions 2 (a) and (b). The amount of fuel produced in a cycle is proportional to the difference in the concentration of oxygen vacancies between the reduced and oxidized states of ceria, $\Delta\delta = \delta_{\mathrm{rd}} - \delta_{\mathrm{ox}}$, which depends on the difference in the temperature and oxygen partial pressure in each step.

Ceria Thermodynamics

Figure 1.1 reveals the thermodynamic equilibrium states of ceria as a function of O_2 partial pressure at various temperatures (1473—1973 K). The functional dependence of δ_{eq} on T and p_{O_2} is obtained from experimental data reported by Panlener et al. [9] for the relative partial molar enthalpy and partial molar entropy. The isotherms in the plot

[1] The exothermicity of the oxidation reaction shown in eq. (2) depends on the temperature and the oxidation state of ceria.

[2] This chapter is based on the article Bala Chandran R., De Smith R. M., and Davidson J.

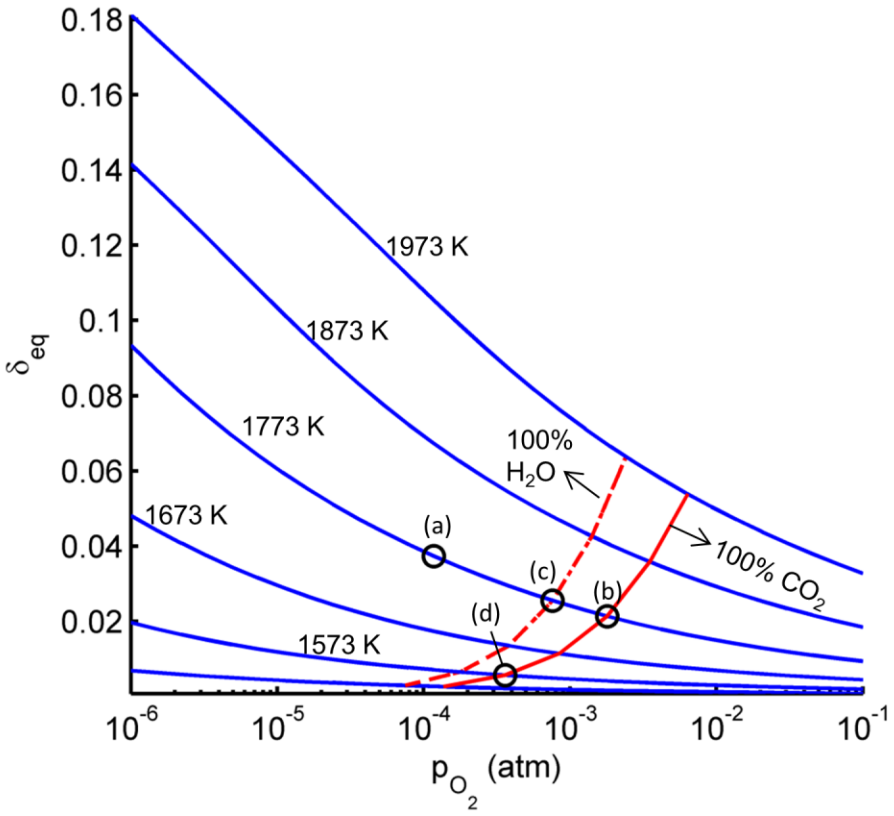

Figure 1.1 State diagram for undoped ceria with the isothermal plots for the equilibrium state for a range of oxygen partial pressures. The equilibrium states for oxidation with 100% CO_2 (solid red lines) and 100% H_2O (dashed red lines) at a total pressure of 1 atm are also shown at various temperatures. Where these lines cross the isothermal lines is the minimum extent to which the reduced ceria can be reoxidized.

(blue lines) depict that high temperatures and low oxygen partial pressures leads to large deviations from stoichiometry. Hence during reduction the upper limit for the ceria nonstoichiometry, δ_{rd} in eq. (1), is set by the operating reactor temperature and the oxygen partial pressure. The solid red line in the plot depicts the thermodynamic minimum for the oxidation nonstoichiometry, δ_{ox} , with 100% CO_2. The same features are indicated by the dashed red lines when pure steam is the oxidizer. The plot makes evident two possible ways to effect a swing in ceria nonstoichiometry: (1) an isothermal or the "pressure swing" cycle and (2) a "temperature swing" cycle. In an isothermal ceria

cycle, the driving potential to produce fuel is generated by maintaining low O_2 partial pressures during reduction that can be achieved by passing an inert gas over the ceria [10–15] or by creating a subatmospheric pressure via vacuum pumping [16–19]. For example, consider the reduction step at 1773 K and an oxygen partial pressure of 10^{-4} atm (10 Pa). The maximum reduction nonstoichiometry at these conditions is $\delta_{\mathrm{rd}} = 0.037$, indicated by (a) in the figure. During oxidation, the lowest oxidation state possible is $\delta_{\mathrm{ox}} = 0.021$ for CO_2 oxidation. For reoxidation of ceria with steam, the equilibrium oxidation state is higher ($\delta_{\mathrm{ox}} = 0.025$) as steam dissociation is less favored compared to CO_2 at higher temperatures, which results in a lower oxygen partial pressure. Therefore, during cycling the oxidation state of ceria moves from (a) to (b) or (a) to (c) depending upon the oxidizer and $\Delta\delta$ = 0.016 and 0.012 for CO_2 and H_2O splitting.

An alternative to an isothermal ceria cycle is the temperature swing cycle in which reaction (2) is carried out after cooling the ceria by hundreds of degrees [10,16]. Consider a representative cycle from (a) to (d) in Figure 1.1. Reduction occurs at 1773 K at 10^{-4} atm oxygen partial pressure and oxidation at 1573 K with CO_2. The maximum possible $\Delta\delta$ for the temperature swing cycle is 0.032 and double that of the nonstoichiometry swing obtained if reduction and oxidation take place at 1773 K. Reoxidation of ceria is thermodynamically favored at lower temperatures.

Isothermal Redox Cycle in Ceria

Although the temperature swing cycle is favored from the material thermodynamics of ceria, a key barrier is the need for solid state heat recuperation, which has proven to be challenging to achieve. Periodic heating and cooling of the reactive material leads to irreversible heat losses and requires recovery of the sensible heat of the

ceria [10,16,20]. Reactor concepts proposed to implement this cycle require moving components that are subjected to large thermal gradients [21,22] and present difficulties for reactor design and operation. On the other hand, the isothermal cycle eliminates the need for solid phase heat recovery between the reaction steps, reduces thermal stresses in the reactor components and simplifies the overall reactor design relative to the two-temperature operation [20,23–25,15].

The focus of this thesis is on the pressure swing, isothermal ceria cycle. In an isothermal cycle, the onus of heat recovery shifts from the solid to the gas phase. Relative to the temperature swing cycle, the oxidizer is heated to higher temperatures. Moreover, a lower oxygen partial pressure is required in the reduction step and/or higher oxidizer concentration is needed for the second step (eq. (2)). These factors highlight the significance of gas phase heat recovery for isothermal cycles. Prior analyses of isothermal cycles showcase the dramatic impacts of gas phase heat recovery on the overall process efficiency [23,25,15,26]. For example, Venstrom et al. [15] illustrate a near doubling of the process efficiency from 3.7% to 7% when the effectiveness of heat recovery increases from 90% to 95%. The challenge for efficient fuel production in this cycle relies on effectively utilizing the sweep gas and oxidizer while still maintaining high fuel production rates.

The present literature pertinent to isothermal ceria cycles covers thermodynamic analysis of the process [20,23,25] and a procedure to optimize operating conditions —gas flow rates and cycle times, based on controlled experiments in a bench top differential reactor to measured global reaction rates. Design of a heat recovery system to operate at high temperatures of 1773 K with close coupling to a solar reactor with oxidizing

environments presents a formidable task and has not been addressed in prior work. The only ceria based solar reactor [11,13] that has been tested implements the temperature swing cycle and produces fuel intermittently with a reported efficiency of 1.7%. Device level characterization of the transient, three dimensional (3-D) transport processes in a solar reactor for redox cycles in ceria is inadequate in the scientific literature. Previous numerical transport models for isothermal and temperature swing ceria based solar reactors include heat transfer analyses precluding the transients of chemical reactions [21,22,27] and investigations of the coupled transport processes modeling surface kinetics in only the reduction step [28–30]. Moreover, the reaction kinetics of the oxidation of ceria by CO_2 at high temperatures has not been examined prior to this work.

The goal of this research has been to apply computational modeling to guide the design of a 4 kW reactor prototype (see Figure 1.2) at the University of Minnesota, implementing an isothermal ceria cycle at nearly 1773 K for splitting CO_2 and H_2O. Numerical models are developed for the gas phase heat recovery system to optimize its design and also of the 4 kW prototype to simulate the coupled transport processes including radiation and the heterogeneous chemical reactions in ceria during isothermal cycling. Model results are used to illustrate the heat transfer–mass transport–chemistry coupling in the solar thermochemical reactor and to assist interpretation of experimental data.

The reactor has a cylindrical receiver cavity lined with six tubular reactive elements each integrated with a ceramic heat exchanger. Concentrated sunlight enters the cavity through an open circular aperture. Each reactive element is a concentric assembly of two alumina tubes, which contain the active redox material, and are integrated with a

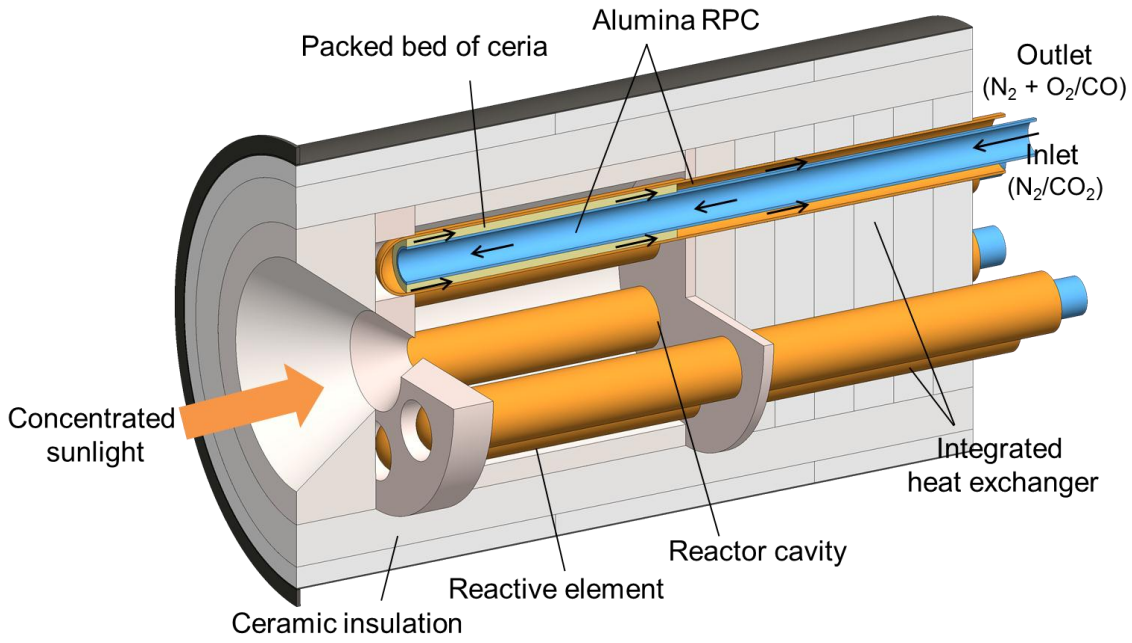

Figure 1.2 Schematic of the reactor prototype designed at the University of Minnesota with reactive elements integrated with counter flow heat exchangers to implement the isothermal ceria redox cycle. Arrows indicate flow direction. Figure is not to scale.

gas phase heat exchanger. Within the solar cavity, the annulus of each reactive element is filled with porous ceria particles. The particle bed provides high surface area for chemical reactions (~ 10^5 m^2 m^{-3}), and facilitates rapid gas diffusion at reasonably low pressure drop (< 20 kPa) [15] . The tubular assemblies extend beyond the solar cavity to integrate seamlessly with a counterflow tubular heat exchanger filled with alumina reticulated porous ceramic (RPC) to provide high heat transfer surface and effective radiative transport. Gas at ambient temperature enters the heat exchanger through the inner tube, is pre-heated by the hot gases leaving the reactor and reverses flow direction at the closed end of the tube assembly nearest the aperture before flowing over the ceria particles. The reactor is designed for operation at about 1773 K within the ceria bed. During reduction, an inert sweep gas (N_2 with 10 ppm trace O_2) passes through the ceria bed. During oxidation, the gas flow is switched to pure CO_2. Fuel is produced continuously by

alternating the gas flows such that half the reactive elements are reduced while the other half is oxidized. The gas flow rates and cycling periods are set to maximize reactor thermal efficiency and fuel productivity [15,31]. More details on the reactor and its operation are included in Chapters 2–4.

The thesis comprises numerical modeling work and evaluation of experimental data central to developing the heat exchanger and to evaluating the transport and chemical processes in the complete reactor. Chapter 2 presents a paper published in the International Journal of Heat and Mass Transfer. This paper is a computational fluid dynamic (CFD) model developed to optimize the design of the counterflow heat exchanger integrated with the reactive elements in the reactor prototype. The model explores the impacts of the morphology of alumina RPC and heat exchanger size on thermal performance, pressure drop and overall process efficiency. Chapter 3 comprises my contributions to a paper that has been submitted to the Journal of Solar Energy and Engineering. An extension of the model developed in Chapter 2 is presented here and applied to experimental data from reactor tests in an indoor high flux solar simulator at the University of Minnesota to characterize the thermal performance of the heat exchanger and the reactive material during steady periodic operation. Chapter 4 presents a transient, 3-D model of the prototype reactor that couples radiative heat exchanger, heat and mass transfer and gas-solid chemical reactions in ceria. Model results facilitate an understanding of the combined interactions of all these transport processes on the overall reactor performance. Chapter 5 presents concluding remarks and suggestions for future work.

Chapter 2

Model of an Integrated Solar Thermochemical Reactor/Reticulated Ceramic Foam Heat Exchanger for Gas-Phase Heat Recovery[2]

The efficiency of solar thermochemical cycles to split water and carbon dioxide depends in large part on highly effective gas phase heat recovery. To accomplish this goal, we present the design and analysis of the thermal and hydrodynamic performance of a counter-flow, tube-in-tube alumina heat exchanger operating at temperatures of 1773 K and integrated with a solar thermochemical reactor for isothermal production of syngas via the ceria redox cycle. The heat exchanger tubes are filled with alumina RPC to enhance heat transfer. The effects of RPC morphology and heat exchanger size on heat transfer, pressure drop, and process solar-to-fuel efficiency are explored by coupling a computational fluid dynamic model of the heat exchanger, including radiative transport, with the overall reactor energy balance. We examine pore densities of 10, 20 and 30 PPI, and porosities of 65–90%. The 10 PPI foam yields the best heat transfer performance and lowest pressure drop, as the larger pores enhance radiative heat transfer and decrease fluid phase drag forces. Although lower porosity is preferred to improve solid phase conduction in the RPC, the tradeoff in heat transfer and pressure drop point to use of higher porosity foam. Optimization for solar-to-fuel reactor efficiency is achieved with 85–90% porosity, 10 PPI RPC.

[2] This chapter is based on the article Bala Chandran R., De Smith R. M., and Davidson J. H., 2015, "Model of an integrated solar thermochemical reactor/reticulated ceramic foam heat exchanger for gas-phase heat recovery," Int. J. Heat Mass Transf., **81**, pp. 404–414.

Introduction

Water and carbon dioxide splitting via thermochemical metal oxide reduction/oxidation cycles driven by concentrated solar energy is a promising means of storing solar energy in chemical bonds via the production of hydrogen or synthesis gas (a mixture of H_2 and CO). The products can be used directly in fuel cells or in the case of synthesis gas converted to liquid transportation fuels. In the present work we consider the non-stoichiometric cerium dioxide (ceria) cycle with a focus on the design of an integrated reactor/heat exchanger for gas-phase heat recovery. The ceria redox cycle consists of an endothermic reduction step (equation (1)) and an exothermic oxidation step with CO_2 and/or H_2O (equations (2a) and (2b)).

$$CeO_{2-\delta_{ox}} \rightarrow CeO_{2-\delta_{rd}} + 0.5\left(\delta_{rd} - \delta_{ox}\right)O_2 \tag{1}$$

$$CeO_{2-\delta_{rd}} + \left(\delta_{rd} - \delta_{ox}\right)CO_2 \rightarrow \left(\delta_{rd} - \delta_{ox}\right)CO + CeO_{2-\delta_{ox}} \tag{2a}$$

$$CeO_{2-\delta_{rd}} + \left(\delta_{rd} - \delta_{ox}\right)H_2O \rightarrow \left(\delta_{rd} - \delta_{ox}\right)H_2 + CeO_{2-\delta_{ox}} \tag{2b}$$

Fuel production is related directly to the change in the number of oxygen vacancies, or equivalently non-stoichiometry of ceria, between reduction and oxidation $\left(\delta_{rd} - \delta_{ox}\right)$. Chemical thermodynamics favors reduction at high temperature (1673–1873 K) and low O_2 partial pressure, and reoxidation at a lower temperature, typically 1073–1273 K [7,32]. However, this approach creates the need for solid phase heat recovery to achieve high reactor efficiencies [16,21,33]. Another option is to carry out the process isothermally or with a much smaller swing in temperature between reduction and oxidation (~100–200 K).

[15,23,25,26]. Isothermal or “near isothermal” cycling eliminates or decreases the requirement for solid-phase heat recovery of the ceria and simplifies the design of reactor components due to reduced thermal stresses. However, in comparison with the larger temperature swing cycle, isothermal cycling requires a lower oxygen partial pressure during reduction to produce an equivalent amount of fuel. For both cycling options, the overall process solar-to-fuel efficiency is improved dramatically with effective gas phase heat recuperation of any inert sweep gas used to maintain a low O_2 partial pressure during reduction and of the oxidizing gas (H_2O or CO_2) [15,16,21,23,33,34]. To date, demonstrations of the ceria redox cycle in prototype reactors [11–13,35] have not included gas phase heat recovery.

The major challenges of designing a gas phase heat recovery system are operation at temperatures as high as 1773 K in a highly oxidizing environment and close coupling of the heat exchanger with the solar reactor. The extreme operating temperature and the requirement for chemical compatibility with ceria and the oxidizing gases constrain the choice of materials for construction. While metals provide high thermal conductivity, the long-term service temperatures of even superalloys are no more than 1223 K due to corrosion and the onset of creep [36,37]. Ceramic materials are an excellent alternative because they can withstand temperatures of 1773–2773 K [36–39]. Heat exchanger designs using ceramic materials have been developed for solar receivers [40], coal or oil fired steam turbines [38] and hydrogen production from sulfuric acid [37,41–43]. The prior work has focused on silicon carbide (SiC) due to its high mechanical strength (tensile strength of 250 MPa at 1773 K), low coefficient of thermal expansion

(5.5×10^{-6} K^{-1}), and high thermal conductivity (~25 W m^{-1} K^{-1} at 1773 K) as compared to other ceramics [38,44]. However, SiC oxidizes at the conditions anticipated in a reactor for reduction and oxidation of ceria [45–47] and has been observed to react vigorously with ceria at high temperatures [48]. In view of these factors, the present study considers the use of alumina tubes (tensile strength of 13 MPa, thermal expansion of 8.6×10^{-6} K^{-1} and thermal conductivity of 6 W m^{-1} K^{-1} at 1773 K) to contain the ceria in the reactor and as the material of construction of the heat exchanger. This approach mitigates the risk of mechanical failure due to differential thermal expansion. From the perspective of thermal design, the challenge is to provide high heat transfer surface area and effective radiative transport. Here we explore the use of open cell, reticulated porous ceramic foam (RPC) as an effective solution.

We evaluate the impact of foam morphology (pore size and porosity) on heat transfer and pressure drop via a computational fluid dynamic (CFD) model of a counter flow tube-in-tube heat exchanger filled with RPC. Radiation has a strong impact on thermal transport, and the optical thickness of the RPC is low by design to reduce temperature gradients in the heat exchanger. Thus, the numerical model extends the scope of existing models of heat transfer for foam heat exchangers, which are largely restricted to metallic foams and either neglect radiative heat transfer [49–52] or model radiation with the diffusion approximation [53], thus restricting the results to large optical thicknesses[3] (> 10) [54,55]. Although radiative transport has been included in heat transfer models for ceramic foams used as volumetric solar receivers [56,57], the prior work is specific to silicon carbide foams for operational temperatures less than 1473 K.

[3] Optical thickness is discussed more elaborately in the following sections in this Chapter.

The CFD model of the heat exchanger is coupled to an energy balance of a prototype solar reactor with the objective of sizing the heat exchanger in conjunction with selection of the mass of redox active material to achieve maximum solar-to-fuel efficiency.

Integrated Reactor/Heat Exchanger Design

Effective heat recovery for this application requires that the heat exchanger integrate directly with the solar reactor to eliminate thermal losses as gases flow to/from the reactor and the heat exchanger [58,59]. Here we consider the integrated solar reactor/heat exchanger design illustrated in Figure 2.1(a). The cavity receiver is lined circumferentially with tubular reactive elements that contain the active redox material. In a $3kW_{th}$ prototype under development, there are six reactive elements and the cavity has a diameter to length ratio of about 0.9 (length equals 0.347 m) to maximize effective emissivity. The cavity is made of layers of ceramic insulation, which are chosen by considering the service temperature and thermal conductivity of commercially available materials. Concentrated sunlight enters the cavity through an aperture and is absorbed by the reactive elements. Each reactive element consists of concentric, high purity (99.8%) alumina tubes. The outer tube has a closed spherical cap at the end located near the front of the reactor cavity. As shown in Figure 2.1 (b), the annular gap is filled with 5 mm long and 5 mm diameter cylindrical porous ceria particles with micro-meter sized pores, and an internal porosity of ~70%. The overall bed void fraction is 0.4. The porous particle bed provides high surface area for chemical reactions ($\sim 10^5$ m^2 m^{-3}), facilitates rapid gas diffusion and yields acceptable pressure drop of less than 0.2 atm through each reactive element for the anticipated gas flow rates [15]. Each tube assembly extends through the

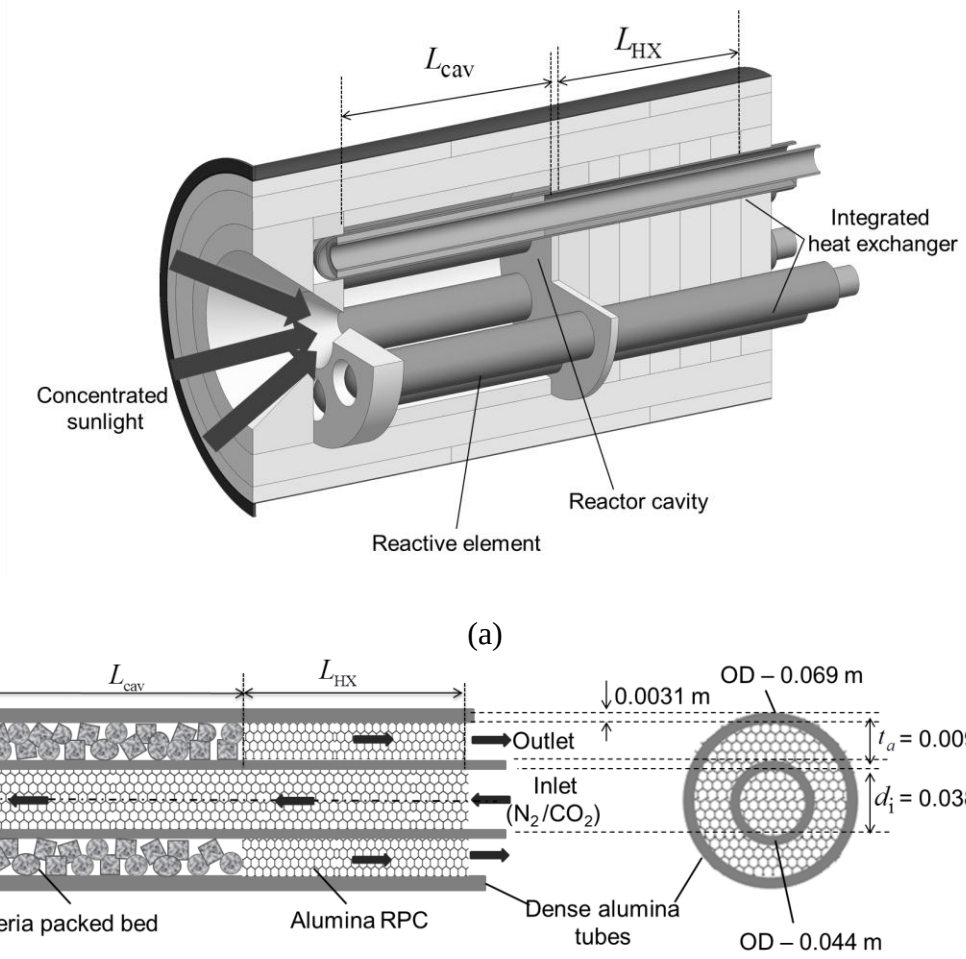

Figure 2.1 Schematic of (a) reactor prototype with reactive elements integrated with counter flow heat exchangers and (b) expanded cross-sectional views of the reactive element connected to the heat exchanger with specified geometric dimensions. Figures are not to scale.

rear of the cavity to form a tube-in-tube counter-flow heat exchanger (Figure 2.1 (b)). In the insulated heat exchanger, both the tube and annulus are filled with inert alumina RPC. Gases enter the inner tube of the heat exchanger at near ambient conditions (in the case of water splitting, the oxidizer enters as steam), flow through reactive element and then return to the heat exchanger through the annulus. During reduction, an inert sweep gas (such as N_2 or Ar) is passed through the tubes (the sweep gas may be used in concert with a vacuum pump) to achieve low partial pressures of O_2 over the ceria particles (see

Figure 2.1 (b)). During oxidation, the gas flow is switched to a flow of steam and/or CO_2. In both steps of the cycle, heat is recovered from the gases leaving the reactor to preheat the gases entering the bed of ceria particles. The heat exchanger is well insulated to reduce thermal losses.

The reactor/heat exchanger design enables cyclic operation in either a continuous mode in which, for equal reduction and oxidation times, half of the reactive elements undergo reduction while the other half produce fuel, or a batch mode in which all reactive elements are simultaneously reduced and then reoxidized.

Analysis Approach

Heat Exchanger Model

To characterize the effects of the porosity and pore size (quantified in terms of pores per inch, PPI) of the alumina RPC on heat transfer and pressure drop, we model the counterflow heat exchanger in Ansys Fluent (15.0). The two-dimensional, axisymmetric numerical domain with boundary conditions is shown in Figure 2.2. For both reduction and oxidation, gas is assumed to be ideal and compressible. Steady-state continuum transport equations are applied for fluid flow and heat transfer. The RPC is considered homogenous and isotropic.

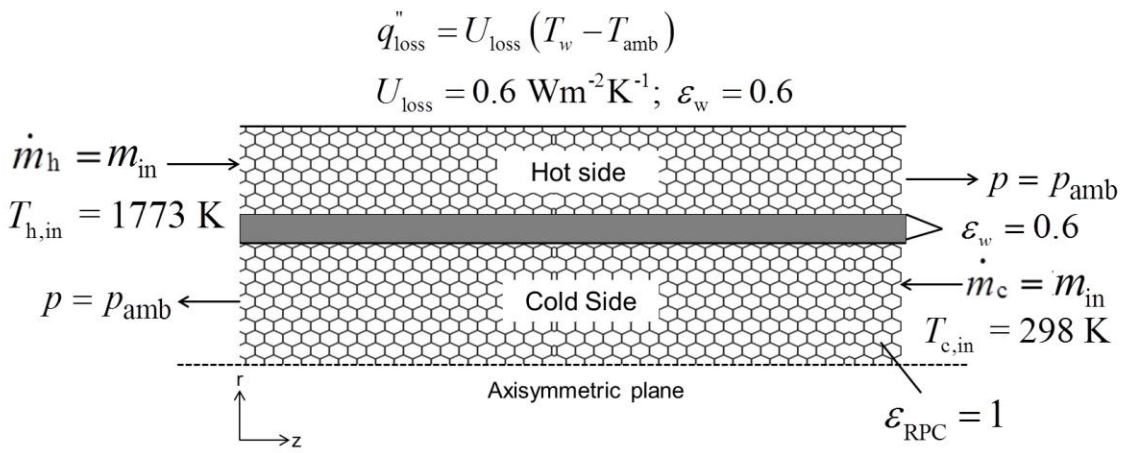

Figure 2.2 Numerical model domain of the heat exchanger with boundary conditions (figure is not to scale).

The mass and momentum conservation equations in the fluid phase are given by:

$$\nabla \cdot \left(\rho_{\text{f}} \boldsymbol{u}\right) = 0, \tag{3}$$

$$\nabla \cdot \left(\rho_{\text{f}} \boldsymbol{u}\boldsymbol{u}\right) = -\nabla p + \nabla \cdot \left(\mu \nabla \boldsymbol{u}\right) \underbrace{- \frac{\mu}{K}\boldsymbol{u} - \rho_{\text{f}} C_E \left|\boldsymbol{u}\right| \boldsymbol{u}}_{S'''_{\text{m}}}. \tag{4}$$

The source term in the momentum equation, S'''_{m}, includes the pressure drop due to viscous forces from the pore walls and the inertial drag as given by the extended Darcy–Brinkman–Forchheimer formulation [60].

A local thermal non-equilibrium formulation results in energy transport equations for the fluid and solid phases, given in equations (5) and (6).

$$\nabla \cdot \left(\rho_{\text{f}} \boldsymbol{u} h_{\text{f}}\right) = \nabla \cdot \left(k_{\text{f,eff}} \nabla T_{\text{f}}\right) + \underbrace{h_{\text{sf}} a_{\text{sf}} \left(T_{\text{s}} - T_{\text{f}}\right)}_{S'''_{\text{q}}}, \tag{5}$$

$$\nabla \cdot \left(k_{\text{s,eff}} \nabla T_{\text{s}}\right) - \nabla \cdot \boldsymbol{q}_{\text{rad}} \underbrace{- h_{\text{sf}} a_{\text{sf}} \left(T_{\text{s}} - T_{\text{f}}\right)}_{S'''_{\text{q}}} = 0. \tag{6}$$

The rate of heat transfer between the solid and fluid phases, S'''_{q}, is expressed in terms of the specific surface area and the interfacial heat transfer coefficient. A user-defined scalar transport equation is modeled in Fluent to implement equation (6) on the same mesh

generated for the fluid phase. The source terms, S_{m}''' and S_{q}''', are appropriately implemented by enforcing the positivity criterion [61,62]. Within the dense alumina inner tube, the steady-state conduction equation is solved and the wall surfaces of the tube are treated as opaque with a surface emissivity of 0.6 [63].

The alumina RPC is treated as an absorbing-scattering-emitting homogenous medium with isotropic, gray, diffuse radiative properties. The extinction coefficient is obtained using the geometric optics model proposed for RPC by Hsu and Howell [64,65]. The optical thickness, $\zeta = \beta l$, for the tube and annulus are defined using the foam extinction coefficient (β) with the gap spacing, t_{a} , and inner diameter, d_{i} , as the respective length scales. Optical thickness is 1 to 8 for the annulus and 5 to15 for the tube, depending on the PPI and porosity of the RPC. Within the annulus, ζ is not large enough to apply the Rosseland diffusion approximation [53] that typically requires optical thickness to be greater than 30. Additionally, alumina RPCs are more scattering than absorbing based on prior measurements and an inverse radiation analysis [66]. Therefore, the spherical harmonics (P_1) approximation of the radiative transport equation is well suited for this application as it allows for both scattering and absorption in the medium [67]. For an isotropically scattering medium, a Laplace equation of the form shown in equation (7) applies, where *G* is the radiation incident on the representative elemental volume.

$$\nabla \cdot \left(\frac{1}{\beta} \nabla G \right) - 3\beta (1-\omega)\left(G - 4\sigma T_{\mathrm{s}}^{4} \right) = 0, \tag{7}$$

$$G = \int_{0}^{4\pi} I(\boldsymbol{r}, \hat{s}) d\Omega. \tag{8}$$

The radiative source term in equation (6) is then evaluated as

$$\nabla \cdot \boldsymbol{q}_{\text{rad}} = \beta(1-\omega)(4\pi I_b - G). \tag{9}$$

The effective transport properties of the RPC depend on the three dimensional foam morphology, including the pore size distribution, strut diameter, connectivity of the solid struts, and cross-sectional area of nodes at the intersection of struts. The average diameter of the pores, d_{p}, strut/fiber diameter, d_{f}, and the specific surface area, a_{sf}, are related to the PPI and porosity of the foam [49,68,69] by

$$d_{\text{p}} = \frac{0.0254}{\text{PPI}}, \tag{10}$$

$$d_{\text{f}} = 1.18\sqrt{\frac{1-\phi}{3\pi}}\frac{d_{\text{p}}}{1-e^{-\left(\frac{1-\phi}{0.04}\right)}}, \tag{11}$$

$$a_{\text{sf}} = \frac{3\pi d_{\text{f}}\left(1-e^{-((1-\phi)/0.04)}\right)}{\left(0.59 d_p\right)^2}. \tag{12}$$

The empirical correlation obtained by Bhattacharya et al. [68,69] for metallic foams is used to determine permeability, K. The inertial coefficient (C_{E}) is calculated using the Ergun model [70].

$$\frac{K}{{d_p}^2} = 0.00073(1-\phi)^{-0.224}\left(\frac{d_f}{d_p}\right)^{-1.11}, \tag{13}$$

$$C_E = \frac{0.3 a_{\text{sf}}}{\phi^3}. \tag{14}$$

The values of K and C_{E} determined from equations (13) and (14) are within 15% of values predicted using the empirical correlations provided in [71–73].

The interfacial heat transfer coefficient is determined using the correlation developed by Zukauskas et al. [74] for an arrangement of staggered cylinders subjected to crossflow,

$$h_{\mathrm{sf}} = \frac{Nu_{\mathrm{sf}} k_{\mathrm{f}}}{d},$$
$$Nu_{sf} = 0.76\,\mathrm{Re}_d^{\,0.4}\,\mathrm{Pr}^{0.37}\left(1 \le \mathrm{Re}_d \le 40\right). \tag{15}$$

The local pore-scale Reynolds number, Re_d, is defined using a length scale based on the fiber diameter [49],

$$d = d_{\mathrm{f}}\left(1 - e^{\frac{-(1-\phi)}{0.04}}\right). \tag{16}$$

The heat transfer coefficient obtained from equation (15) is within 10% of estimated values for silicon carbide foams using tomographic images [73] and numerical simulations on ceramic foam structures [75].

The fluid phase effective thermal conductivity is given by $k_{\mathrm{f,eff}} = \phi k_f$. Of the various correlations that were considered for $k_{\mathrm{s,eff}}$ [68,76–78], Coquard et al. [79] and Kamuito [80] establish that the analytical expression obtained by Schuetz and Glicksman [78] for polyurethane foams is the most applicable, as it adequately (within 30% of experimental measurements) represents thermal conductivities of open cellular structures. The lower limit for $k_{\mathrm{s,eff}}$ in equation (17) is used in the model to obtain a conservative estimate of the heat transfer performance.

$$0.8\left(1-\phi\right)\frac{k_s}{3} < k_{\mathrm{s,eff}} < \left(1-\phi\right)\frac{k_s}{3}. \tag{17}$$

The extinction coefficient, β, and the scattering albedo, ω, are representative of the extent of attenuation and scattering of radiative intensity in a medium. These

coefficients have been evaluated for 10, 20, 30 and 65 PPI alumina RPCs at only one porosity (70%) [66]. Spectral radiative properties of partially stabilized, reticulate zirconia and SiC foams have been obtained using a combination of experiments and inverse numerical techniques [65]. Thus, in the absence of available data to relate optical transport properties of alumina RPC as a function of foam PPI and porosity, we apply the correlations provided for zirconia foams [65]. The extinction coefficient determined from [65] are within 25% of the predictions in [66]. A modified constant has been used in the geometric optics model to determine β in [65], equation (18), and a range of 0.81–0.999 was obtained for the scattering albedo.

$$\beta = \frac{4.4(1-\phi)}{d_{\mathrm{p}}}. \tag{18}$$

The lower limit for scattering albedo, $\omega = 0.81$, is employed in the model and the sensitivity of heat transfer performance to ω was evaluated for $0.81 \le \omega \le 0.999$. The overall heat transfer coefficient changed less than 10% over this range.

The boundary conditions are shown in Figure 2.2. The mass flow rate and temperature of the gases are specified at the inlets of the hot (annulus) and cold (inner channel) sides of the heat exchanger. For the present simulations, the hot side inlet is fixed at 1773 K, which is the intended operating temperature of the reactor and the cold side inlet is fixed at 298 K. The results are presented for CO_2 splitting and N_2 sweep gas. The gases are assumed to be maintained at a uniform composition in the heat exchanger—N_2 with 10 ppm O_2 during reduction and a mixture comprising CO_2 and CO during oxidation. The inter-species transport is not modeled and the thermophysical properties (viscosity, thermal conductivity and specific heat) of the gas mixture are based

on the local temperature [81,82], using a mixing rule with mole fraction as weighting function for the pure species. The surface emissivity of RPC alumina at the gas inlets and outlets is assumed to be 1—a reasonable selection considering the high temperatures near the reactor and roughness in the pore surfaces. The gases are stipulated to leave the domain at atmospheric pressure. A no-slip boundary condition is imposed on all solid walls. Temperature and heat flux continuity is imposed at the wall-fluid interfaces. In the prototype heat exchanger, the RPC is bonded to the alumina tubes but the model does not capture the effect of contact resistance. It is anticipated that in the presence of radiation, the effect of contact resistance between the tube wall and the RPC will be much less significant than it would be at lower temperature. The net heat flux on the tube wall surfaces (inner and outer) are evaluated as the sum of heat fluxes on the fluid and solid surfaces and by imposing thermal equilibrium at the boundary,

$$q_w^{"} = k_{\mathrm{s,eff}} \left.\frac{\partial T_\mathrm{s}}{\partial r}\right|_{r=r_w} + k_{\mathrm{f,eff}} \left.\frac{\partial T_\mathrm{f}}{\partial r}\right|_{r=r_\mathrm{w}}, \qquad T_\mathrm{s}\big|_{r=r_\mathrm{w}} = T_\mathrm{f}\big|_{r=r_\mathrm{w}} = T_\mathrm{w}\big|_{r=r_\mathrm{w}}. \tag{19}$$

These equations are implemented by using boundary profile user-defined functions in Fluent on the respective surfaces. For the outer tube surface, conduction losses through the insulation material surrounding the heat exchanger, $q_{\mathrm{loss}}^{"}$, are modeled as

$$q_{\mathrm{loss}}^{"} = U_{\mathrm{loss}}(T_w - T_{\mathrm{amb}}), \tag{20}$$

where U_{loss} is determined from 3-D simulations of steady-state conduction through the insulation surrounding the heat exchanger. For the incident radiation, Marshak's condition [57,67] for direction integrated radiative heat flux is imposed at all wall boundaries.

The heat exchanger performance is quantified by the overall heat transfer coefficient, U_{i}, and pressure drop, Δp_{HX}. The heat transfer coefficient is evaluated based on the inner channel surface area (A_{i}),

$$U_{\mathrm{i}} = \frac{\dot{m}_c \left(h_{\mathrm{c,out}} - h_{\mathrm{c,in}} \right)}{A_{\mathrm{i}} \left(\bar{T}_{\mathrm{c}} - \bar{T}_{\mathrm{h}} \right)}, \tag{21}$$

where $\bar{T}_{\mathrm{c}}$ and $\bar{T}_{\mathrm{h}}$ are the bulk mean temperatures of the cold and hot side streams respectively, and the numerator is the rate of energy transferred to the cold stream or the heat duty of the heat exchanger. The impact of foam morphology on U_{i} and Δp_{HX} is examined for 10, 20 and 30 PPI and porosities varying from 65 to 90%.

The conjugate heat transfer model was solved in Fluent with a structured/mapped mesh of quadrilateral elements. A maximum of 12000 (60 radial × 200 axial) elements were created, with finer elements close to the solid walls. The pressure and velocity fields are coupled using the PISO algorithm in Fluent [83]. A second order upwind method was applied for the advection terms in the momentum, energy (fluid and solid phase), and incident radiation equations. Large magnitudes of source terms in the energy transport equations, due to the interfacial heat transfer between the solid and fluid phases and radiation, were resolved by using an under-relaxation factor of 0.985 for the energy equations. The under-relaxation factor was selected by progressive reduction of values from 1 until smooth convergence of the residuals was obtained. The local thermal non-equilibrium formulation for energy transport and the nature of heat flux boundary conditions necessitate numerous iterations (up to 20000) to achieve a steady-state solution. To speed the solution, the mesh was partitioned and verified to ensure load balancing on eight nodes on an Intel Xeon X5690 (4.1 GHz, 12 GB) core [62,83]. The

governing equations were solved in a sequential manner with the globally scaled residual values for convergence set to 10^{-10} for all transport equations, including radiative transfer. Additionally, the gas bulk mean temperatures at the cold side and hot side exits were monitored to be constant for 100 iterations after the solution converged.

Integrated Reactor/Heat Exchanger

The design of the reactor and heat exchanger is specified by determining the mass of ceria, the RPC morphology and the length of the heat exchanger that provide the best efficiency. The mass of ceria contained within the reactive elements and the effectiveness of gas phase heat recuperation (and thus heat exchanger design) are linked through an overall energy balance on the system:

$$q_{\text{solar}} = \frac{\sigma T_R^4}{CI} q_{\text{solar}} + F_L q_{\text{solar}} \left(1 - \frac{\sigma T_R^4}{CI}\right) + \bar{\dot{n}}_f{}' \Delta H_r|_{T_R} + \dot{n}_{\text{sg}}{}' \left(\frac{\tau_{\text{rd}}}{\tau_{\text{rd}} + \tau_{\text{ox}}}\right)\left[\bar{h}_{\text{sg}}(T_R) - \bar{h}_{\text{sg}}(T_{\text{sg,out}})\right] + \dot{n}_{\text{ox}}{}' \left(\frac{\tau_{\text{ox}}}{\tau_{\text{rd}} + \tau_{\text{ox}}}\right)\left[\bar{h}_{\text{ox}}(T_R) - \bar{h}_{\text{ox}}(T_{\text{ox,out}})\right]. \quad (22)$$

Each term in the energy balance is evaluated per unit mass of ceria and is averaged over a cycle to account for the switching in the gas compositions. The total solar energy input to the reactor, $\dot{Q}_{\text{solar}}$, is held fixed at 3 kW_{th} in this study and thus the total mass of ceria that can be utilized in the prototype (split between the six reactive elements) is given by

$$m_{CeO_2} = \frac{3000\ \text{W}}{q_{\text{solar}}}. \quad (23)$$

The first term on the right hand side of equation (22) represents reradiation losses from the cavity, assuming a black cavity receiver and a concentration ratio (C) of 3000 (3 MW m^{-2}), a good choice for operation at 1773 K [23]. The second term represents

convective losses from the reactor as a fraction (F_L) of the absorbed solar input. Here, the temperature dependent loss fraction, F_L, is assumed to be 0.2, which is consistent with the heat losses reported in [84].

The third term represents the power requirement of producing the fuel, where $\Delta H_r|_{T_R}$ is the enthalpy change of the CO_2 splitting reaction, evaluated at the isothermal reactor temperature of 1773 K. The mass-specific fuel production rate averaged over one cycle, $\bar{\dot{n}}_f'$, is 0.078 μmol s^{-1} g^{-1} based on measured data obtained in a small scale reactive element at 1773 K, and 1 bar for reduction and oxidation periods (τ_{rd} and τ_{ox}) of 100 s each [8]. The key to applying this mass specific rate to the larger reactive element is the application of chemical similitude, as detailed by Venstrom et al. [15]. The three relevant dimensionless parameters for similitude are the aspect ratio (the ratio of the ceria particle bed length to its radius), the Peclet number (the ratio of the characteristic gas diffusion time to the gas residence time), and the Damköhler number (the ratio of the gas residence time to the characteristic reaction time). Matching the Damköhler number is most important for similitude in this problem; for data reported in [15], with similar Damköhler the average fuel production rate was constant even with a three-fold difference in aspect ratio and a factor of 20 difference in Peclet numbers. In the present analysis, we match the Damköhler number by matching the ceria-mass-specific sweep gas and CO_2 flow rates used in the prior experiments. The mass-specific flow rates of sweep gas and oxidizer are fixed at $\dot{n}_{\mathrm{sg}}' = 1\times10^{-4}$ mol s^{-1} g^{-1} and $\dot{n}_{\mathrm{ox}}' = 3.3\times10^{-5}$ mol s^{-1} g^{-1} based on the data and optimization procedure presented in [15].

The fourth and fifth terms in equation (22) represent the sensible heating requirements of the sweep gas (during reduction) and oxidizer (during oxidation), which depend on the heat exchanger effectiveness during reduction and oxidation, respectively.

$$\varepsilon_{\mathrm{rd}} = \frac{\left(\bar{h}_{\mathrm{sg}}(T_{\mathrm{sg,out}}) - \bar{h}_{\mathrm{sg}}(T_{\mathrm{amb}})\right)}{\left(\bar{h}_{\mathrm{sg}}(T_R) - \bar{h}_{\mathrm{sg}}(T_{\mathrm{amb}})\right)} \tag{24a}$$

$$\varepsilon_{\mathrm{ox}} = \frac{\dot{n}_{\mathrm{ox,in}}\left(\bar{h}_{\mathrm{ox,in}}(T_{\mathrm{ox,out}}) - \bar{h}_{\mathrm{ox,in}}(T_{\mathrm{amb}})\right)}{\dot{n}_{\mathrm{ox,out}}\left(\bar{h}_{\mathrm{ox,out}}(T_R) - \bar{h}_{\mathrm{ox,out}}(T_{\mathrm{amb}})\right)} \tag{24b}$$

The CFD model of the heat exchanger is implemented to solve for the temperatures of the sweep gas and oxidizer after they are preheated in the heat exchanger, $T_{\mathrm{sg,out}}$ and $T_{\mathrm{ox,out}}$. The values of the total flow rates of sweep gas and oxidant and the corresponding effectivenesses of the heat exchanger are determined by iteration between the heat exchanger model and the reactor energy balance. The convergence criterion is that the heat recovery effectiveness changes by less than 0.1% between iterations, corresponding to a change in ceria mass of less than 100 g.

This iterative procedure is carried out for a range of RPC morphologies and heat exchanger lengths to identify the ceria mass and heat exchanger geometry that maximizes solar-to-fuel efficiency for the assumed values of mass-specific fuel production, flow rates, and cycle duration. The time-averaged solar-to-fuel efficiency is defined as:

$$\eta = \frac{\bar{\dot{n}}_f \times HHV_f}{\dot{Q}_{\mathrm{solar}} + \dot{Q}_{\mathrm{pump}}} = \frac{\left(\bar{\dot{n}}_f{}' \times m_{\mathrm{CeO_2}}\right) \times HHV_f}{q_{\mathrm{solar}} \times m_{\mathrm{CeO_2}} + \dot{Q}_{\mathrm{pump,rd}} + \dot{Q}_{\mathrm{pump,ox}}}. \tag{25}$$

The numerator is the product of the average CO production rate over a cycle and the higher heating value of the fuel. The denominator includes the fixed solar input of 3 $\mathrm{kW_{th}}$ plus the pumping power requirement, $\dot{Q}_{\mathrm{pump}}$, which is the sum of pumping power for

reduction $\dot{Q}_{\text{pump,rd}}$ and oxidation $\dot{Q}_{\text{pump,ox}}$. Prior reports [11,13,35] of experimentally determined solar-to-fuel efficiency have not included pumping power explicitly but rather lump pumping power with the parasitic power required for inert gas separation via cryogenic air separation, which delivers the sweep gas at a fixed pressure of 8 bars [85]. This approach does not capture the tradeoff in heat transfer and pumping power of the heat exchanger in overall process efficiency. In this analysis, the theoretical minimum energy requirements for producing sweep and oxidizer gases are considered assuming that the outlet streams are recycled [23]. These energy overheads are small (< 45W) compared to the other terms in the denominator and therefore neglected here. The authors acknowledge that the theoretical minimum work needed to produce the inert gas is less than the current industrial standard for air separation and thus efforts to reduce the amount of sweep gas required for the redox cycle are warranted.

The thermal equivalent of pumping power is,

$$\dot{Q}_{\text{pump},j} = \frac{\bar{\dot{n}}_j \left(\frac{\gamma_j}{\gamma_j - 1} \right) \bar{R} T_0 \left[\left(\frac{p_{\text{atm}} + \Delta p_j}{p_{\text{atm}}} \right)^{\frac{\gamma_j - 1}{\gamma_j}} - 1 \right]}{\eta_{\text{th-e}} \eta_{\text{comp}}}. \tag{26}$$

The numerator is the average isentropic pumping power required to overcome the pressure drop Δp_j across both the heat exchanger (determined by the heat exchanger model) and the reactive element. The pressure drop across the reactive element is determined by applying the Darcy–Forchheimer formulation [60], assuming negligible flow through the micrometer sized internal pores of ceria particles, with the packed bed permeability ($K_{\text{RE}} = 2.5 \times 10^{-8}\,\text{m}^2$) and inertial coefficient ($C_{\text{E,RE}} = 3281\,\text{m}^{-1}$) estimated

from the Carmen–Kozeny [60] and Ergun [70] models respectively. The reactive element length is varied to accommodate the required mass of ceria. The denominator accounts for the isentropic efficiency of the compressor, η_{comp} = 0.8 [86], and converts the pumping power to a solar thermal equivalent with a thermal-to-electric efficiency of $\eta_{th\text{-}e}$ = 0.2 [87]. As will be shown by the results, pumping power is an important consideration for both inert and oxidizing gases. This statement is particularly true when using gas flow rates commensurate with measured rates of reaction rather than assumed idealistic models for flow, such as the counterflow model used in several thermodynamic analyses [23,26].

Table 1 lists the fixed parameters used in the reactor efficiency calculation.

Table 1 Parameters fixed in the reactor energy balance and efficiency calculation

Parameter	Value
T_R	1773 K
T_{amb}	298 K
C	3000
I	1000 W m^{-2}
F_L	0.2
$\bar{\dot{n}}_f'$	0.078 μmol s^{-1} g^{-1}
$\bar{\dot{n}}_{sg}'$	50 μmol s^{-1} g^{-1}
$\bar{\dot{n}}_{ox}'$	16 μmol s^{-1} g^{-1}
$\dot{Q}_{input}$	3000 W
$\eta_{th\text{-}e}$	0.2
η_{comp}	0.8
τ_{rd}	100 s
τ_{ox}	100 s
p_{amb}	100 kPa

Results

Effect of Morphology

As a first step in the specification of foam morphology, the influence of porosity and PPI on the overall heat transfer coefficient and pressure drop was explored for a fixed mass flow rate of sweep gas (1.8×10^{-3} kg s^{-1}), corresponding to a mass of ~3800 g of ceria, and 1.4 m long heat exchanger. The overall heat transfer coefficient is insensitive to flow rate over the range relevant to this study (1×10^{-3} kg s^{-1} to 5×10^{-3} kg s^{-1}) as the flow is laminar ($80 < \mathrm{Re}_{d_i} < 500$). The inlet temperature on the hot side of the heat exchanger is 1773 K in accordance with the high temperature required for reduction of ceria. The inlet gas temperature is anticipated to influence the heat recovery effectiveness, due to the significance of radiation.

The results shown in Figure 2.3 for 10, 20 and 30 PPI for 65% ≤ ϕ ≤ 90% suggest that the 10 PPI foam provides the best performance for all porosities considered. For reference, results are also provided for a heat exchanger without foam, indicated by dashed lines in the plots. First, consider the heat transfer performance (Figure 2.3 (a)). The overall heat transfer coefficients for foam filled heat exchangers are at least twenty times greater than the tubular heat exchanger without RPC, and increase as porosity and PPI are decreased. The 10 PPI foam delivers higher overall heat transfer than the 20 and 30 PPI foam due to enhanced radiative transport in the larger pores. This enhancement in heat transfer with lower PPI is achieved even with a reduction in specific surface area for heat exchange between the solid and the fluid phases (e.g., a_{sf} = 1587 m^{-1} and 3174 m^{-1} for 10 and 20 PPI foams at 85% porosity). From this result we infer that even for the 10 PPI foam, the thermal resistance to interfacial heat transfer is low compared to the conductive and radiative resistances (pore-scale Re_d < 25 and k_f/k_s > 0.01 for all cases considered). Even though the penetration of radiation improves for higher porosities, the lowest porosity of 65% yields the greatest heat transfer for all PPI due to improved conduction of the RPC solid phase. For the flow rates considered here, conduction and radiation are more significant than convective heat transfer.

As shown in Figure 2.3 (b), the 10 PPI foam also provides the lowest pressure drop due to the reduction in viscous and inertial drag forces in the larger pores. Increasing porosity also reduces pressure drop due to higher foam permeability and reduced inertial losses. Although Figure 2.3 (a) supports the choice of low porosities to augment thermal performance, Figure 2.3 (b) makes evident the corresponding penalty due to higher pressure drop.

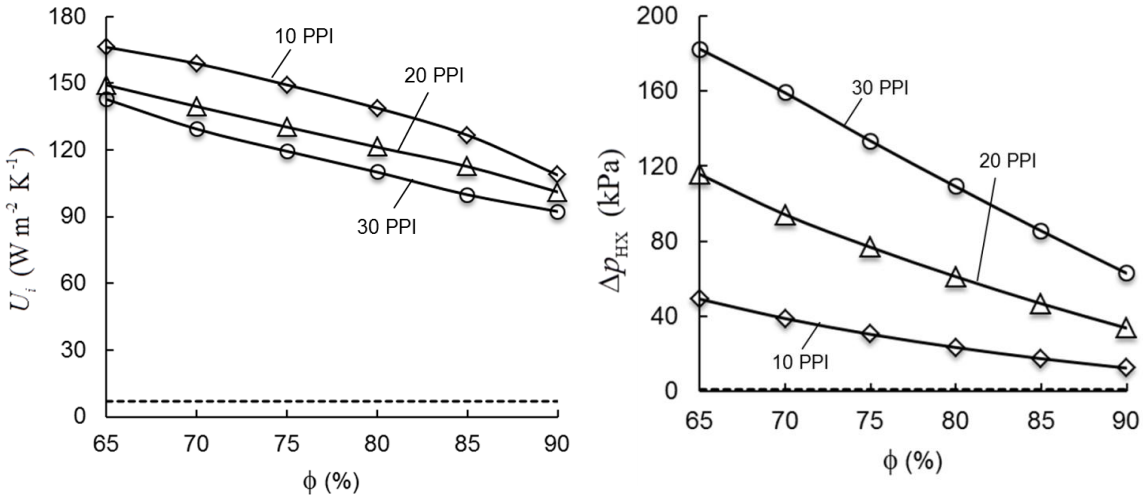

(a) (b)

Figure 2.3 Effect of foam PPI and ϕ (%) on (a) U_i and (b) Δp_{HX} for fixed sweep gas flow rate of 1.8×10^{-3} kg s^{-1} and a 1.4 m long heat exchanger. Simulations are performed at selected porosities shown by the markers (lines are drawn as a visual aid). Dashed line indicates results for an empty tube-in-tube heat exchanger.

To illustrate the relative contributions of radiative transport, conduction in the solid phase and fluid phase convection, the axial variation of heat fluxes at the inner tube inner wall is depicted in Figure 2.4 for 10 and 20 PPI RPC with 65% and 90% porosities. Radiative transport is most significant near the hot side inlet (z = 0) and decreases with decreasing temperature as heat is transferred from the hot gas exiting the reactor to the cold side gas flowing into the reactor. For both 65 and 90% porosity, radiative heat transfer is enhanced in the larger pores of the 10 PPI foam because the extinction coefficient decreases (equation (18)), which in turn augments the rate of diffusion of thermal radiation in the medium (equation (7)). Because β also decreases with increasing porosity (equation (18)), the radiative heat flux is highest for $\phi = 90\%$. The conductive flux is similar in magnitude for the 10 and 20 PPI foams, but is improved with decreased porosity because of the increase in average effective thermal conductivity,

$\bar{k}_{s,eff}$. For example, the average effective thermal conductivity increases from 0.3 W m^{-1} K^{-1} for 90%, 10 PPI to

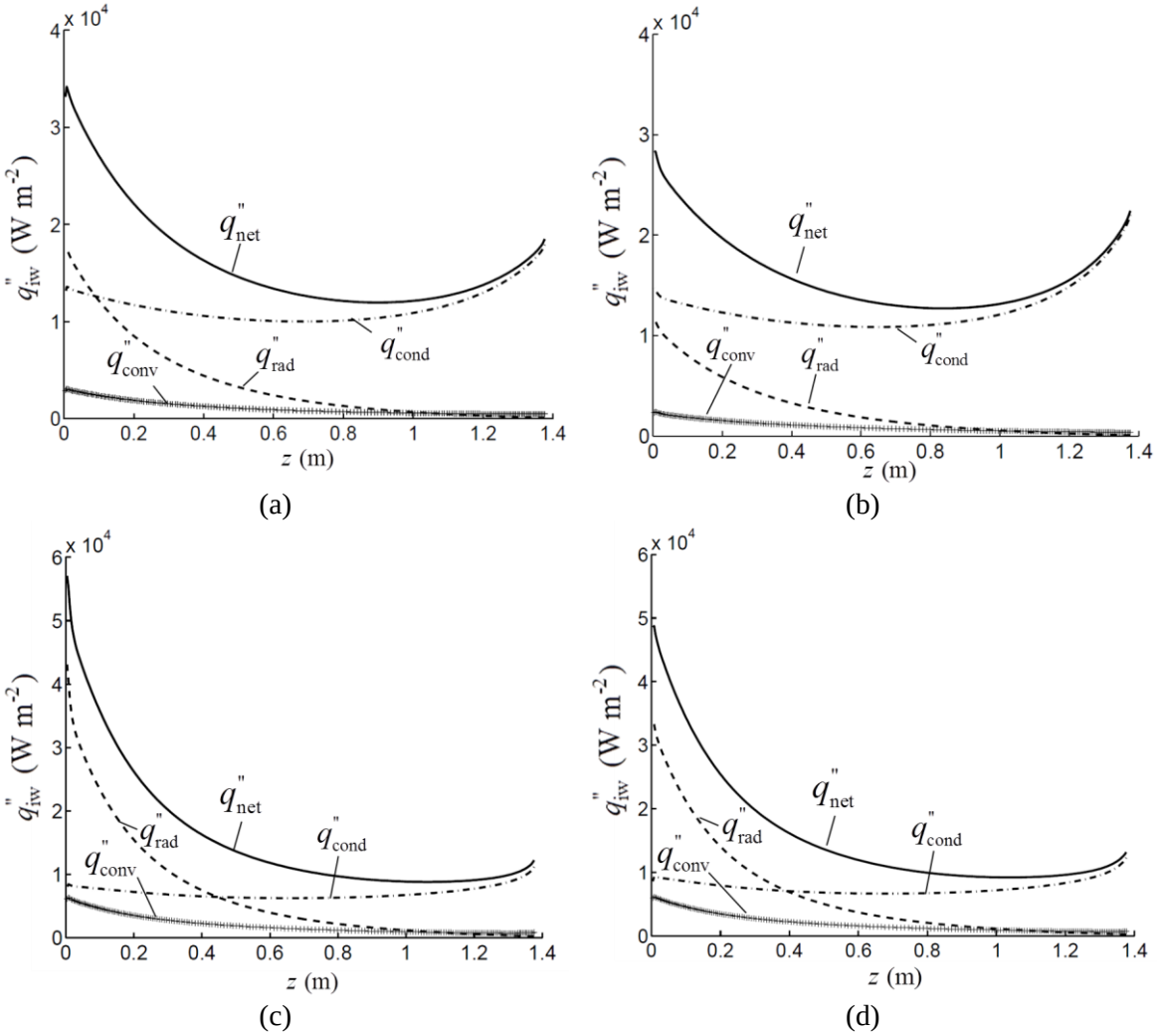

Figure 2.4 Axial variation of heat fluxes at the inner tube inner wall, during reduction with gas flow rate of 1.8×10^{-3} kg s^{-1}, in a 1.4 m long heat exchanger filled with RPC morphologies of 65% porosity, (a) 10 PPI and (b) 20 PPI ; 90% porosity, (c) 10 PPI and (d) 20 PPI.

1 W m^{-1} K^{-1} for 65%, 10 PPI. The conductive fluxes increase slightly near the cold side inlet (z = 1.4 m) due to increase in $k_{s,eff}$ as the gases cool down. The reduction in viscous and inertial drag associated with the higher porosity results in a near doubling of convective fluxes at $\phi = 90\%$ as compared to 65% porosity, but even in this case heat

transfer is predominately driven by conduction and radiation. As conductive heat transfer overshadows radiation and convection over a majority of the heat exchanger length for all PPI, the effect of weakened solid phase conduction at high porosities is to decrease the overall heat transfer coefficient despite better radiation and convection.

Figure 2.5(a) and 2.5 (b) show the cold side gas phase radial temperature distributions normalized by the inner tube inner wall temperature, T_{iw}, at two axial locations, z = 0.1 and 0.7 m for 10 and 20 PPI foams with $\phi = 65\%$ and $\phi = 90\%$. The solid and gas phase temperatures are within 3 K for the 10 PPI foam and even closer for larger PPI. Therefore, only the gas phase temperatures are shown in the plots. The radial temperature distributions are relatively uniform at z = 0.1 m (Figure 2.5 (a)) due to enhanced radiative transport in the hotter section of the heat exchanger. At both axial locations, the 10 PPI foam with 65% porosity exhibits the most uniform temperature distribution due to better solid phase conduction. At z = 0.7 m, the shape of the temperature profiles (Figure 2.5 (b)) is influenced more by solid phase conduction and hence the profiles are steeper for $\phi = 90\%$ due to the diminished thermal conductivity, $k_{s,eff}$, for both pore sizes. The radial temperature profiles are largely unaltered with changes in pore size as $k_{s,eff}$ remains constant.

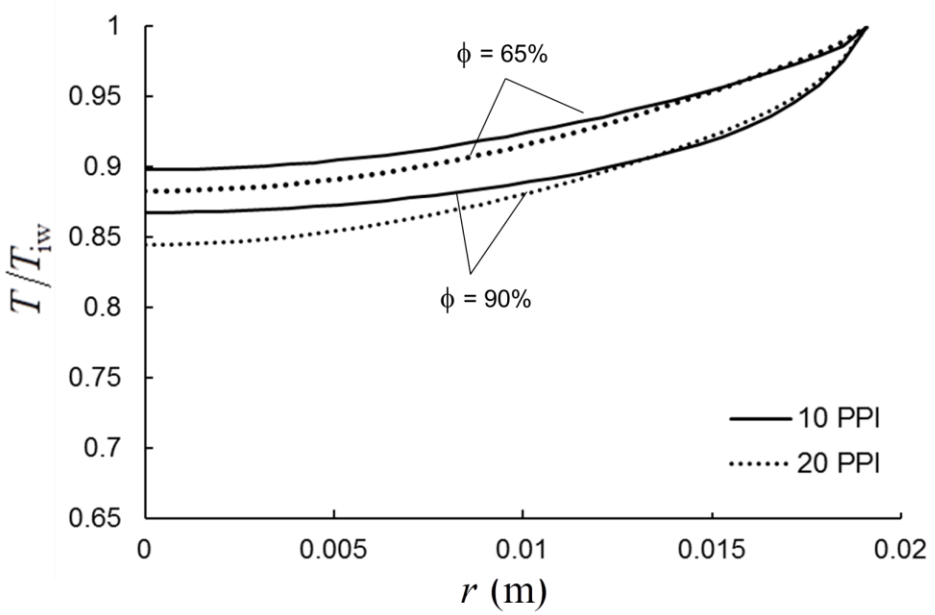

(a)

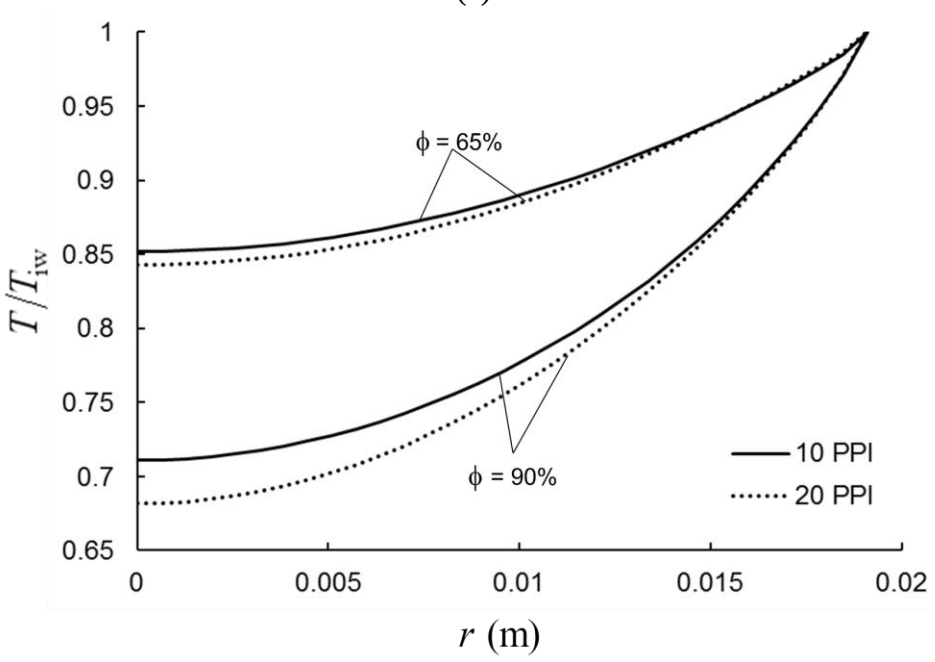

(b)

Figure 2.5 Normalized radial temperature profiles of the gases on the heat exchanger cold side, where, T_i is the inner tube inner wall temperature, for L_{HX} = 1.4 m and sweep gas flow rate of 1.8×10^{-3} kg s^{-1} for 10 and 20 PPI foams with 65% and 90% porosities at (a) z = 0.1 m and (b) z = 0.7 m.

The axial bulk-mean gas temperatures are shown in Figure 2.6 for 10 PPI, 90% porous foam. For the assumed sweep gas flow rate of 1.8×10^{-3} kg s^{-1} and $L_{HX} = 1.4$ m, the cold-side gas leaves the heat exchanger and enters the reactor at 1320 °C, resulting in heat recovery effectiveness of 87%. For the same operating conditions, the predicted heat exchanger effectiveness is 90% for the 10 PPI, 65% porous foam. With only a modest increase in heat recuperation in the low porosity foam, there is a heavy penalty in the pressure drop (49 kPa versus 13 kPa for $\phi = 90\%$).

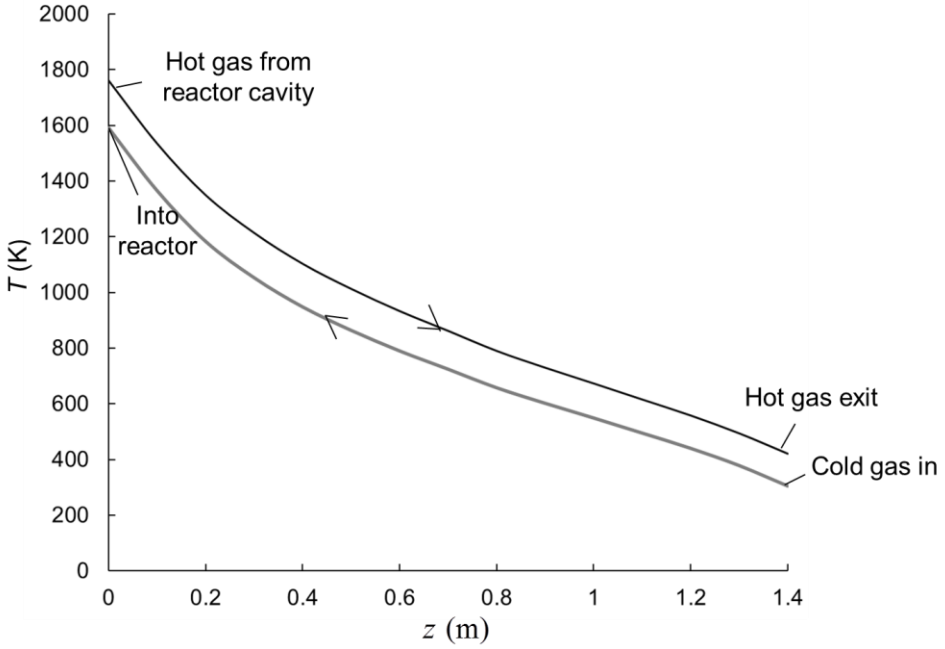

Figure 2.6 Bulk mean gas temperatures at various axial locations in a 1.4 m long heat exchanger with 10 PPI and 90% porous RPC for sweep gas flow rate of 1.8×10^{-3} kg s^{-1}.

In summary, we down selected 10 PPI foam for further evaluation as it provides the best balance of heat transfer and pressure drop. Larger pore sizes, for example a 5 PPI foam (nominal pore diameter of 5.1 mm) may provide an additional benefit in the inner tube but are likely unsuitable for the narrow annular gap (9.6 mm). The selection of porosity and overall heat exchanger length require consideration of reactor efficiency.

Optimization of solar-to-fuel efficiency

Table 2 lists the results of the parametric study of the impact of the porosity of the 10 PPI RPC and the length of each heat exchanger on the heat exchanger effectiveness and the design (i.e., the mass of ceria) and the operation (total gas flow rates, pumping power, fuel production and efficiency) of the 3 kW_{th} prototype reactor. The power available for chemistry, and thus the total mass of ceria, which determines the mass flow rates and the rate of fuel production, is highly sensitive to the effectiveness of heat recovery. For example, a 1.4 m long heat exchanger with 10 PPI, 65% porosity RPC provides the highest heat exchanger effectiveness (89% for reduction, and 92% for oxidation) and thermal duty (3.56 kW for reduction, and 1.89 kW during oxidation) of the options considered, and yields CO at an average rate of 394 $\mu mol\ s^{-1}$ with 5100 g of ceria in the reactor. With 90% porosity, the heat exchanger effectiveness decreases only slightly to 86% for reduction and 91% for oxidation, yet fuel production is reduced by more than 18%. This dramatic result demonstrates the significance of sensible heating of the reduction and oxidation gases in the overall energy budget. However, as shown by comparison of the solar-to-fuel efficiency for these two examples, the benefit of improved fuel production with 65% porosity RPC is offset by an increase in pumping power. The solar-to-fuel efficiency of the integrated reactor/heat exchanger is improved from 1.9 to 2.4% with the increase in porosity from 65% to either 85 or 90%. If pumping power were not included in the calculation of solar-to-fuel efficiency, the predicted efficiencies would increase monotonically with decreasing porosity due to both higher fuel production and improved effectiveness of heat recuperation. Without accounting for

the pumping power, the predicted efficiency is 3.7% and 3.0% for porosities of 65% and 90% respectively.

Table 2 Summary of results of parametric study of RPC porosity and heat exchanger length

L (m)	ϕ (%)	m_{ceria} (kg)	Δp_{RE} (kPa)		Δp_{HX} (kPa)		ε (%)		$\dot{\bar{n}}_f$ (μmol-s^{-1})	Heat duty (kW)		η (%)
			$\Delta p_{RE,rd}$	$\Delta p_{RE,ox}$	$\Delta p_{HX,rd}$	$\Delta p_{HX,ox}$	ε_{rd}	ε_{ox}		Rd	Ox	
0.35	65	2.9	6.9	2.2	8.4	2.1	79.8	86.4	223	1.82	1.00	1.9
0.35	75	2.7	6.3	2.0	4.7	1.3	78.5	86.1	212	1.70	0.97	1.9
0.35	80	2.6	6.1	1.9	3.5	1.0	77.4	85.8	203	1.63	0.94	1.8
0.35	85	2.5	5.6	1.8	2.4	0.7	76.5	85.6	197	1.53	0.89	1.8
0.35	90	2.4	5.1	1.7	1.0	0.5	74.5	84.9	184	1.45	0.85	1.7
0.35	100	0.9	0.9	0.4	0.0	0.0	33.1	54.8	69	0.22	0.20	0.7
0.7	65	3.9	11.3	3.3	26.5	6.3	85.3	89.8	301	2.64	1.44	2.1
0.7	75	3.7	10.4	3.1	14.7	3.7	84.3	89.5	284	2.47	1.36	2.2
0.7	80	3.6	9.6	2.9	10.4	2.7	83.7	89.5	277	2.34	1.30	2.2
0.7	85	3.4	8.8	2.7	7.1	1.9	82.9	89.3	266	2.30	1.25	2.2
0.7	90	3.2	8.1	2.5	4.7	1.3	81.2	88.7	245	2.06	1.17	2.1
0.7	100	1	1.0	0.4	0.0	0.0	40.6	54.0	75	0.31	0.21	0.7
1.4	65	5.1	17.5	4.7	72.8	12.5	89.3	91.8	394	3.56	1.89	1.9
1.4	75	4.8	15.9	4.2	40.8	9.7	88.4	91.5	370	3.33	1.79	2.1
1.4	80	4.6	15.2	4.2	28.0	7.2	88.1	91.4	362	3.23	1.74	2.3
1.4	85	4.4	14.1	4.0	20.6	5.1	87.3	91.3	346	3.10	1.66	2.4
1.4	90	4.1	12.5	3.6	13.0	3.0	86.2	90.9	322	2.82	1.54	2.4
1.4	100	1.1	1.2	0.5	0.0	0.0	45.5	60.3	83	0.38	0.27	0.8

Solar-to-fuel efficiency is plotted in Figure 2.7(a) for heat exchanger lengths from 0.35 to 1.4 m and for RPC porosities from 65 to 90%. For reference, the efficiency is also provided for heat exchangers without RPC (i.e. ϕ = 100%). Without RPC, efficiencies are less than half those achieved with RPC. The trends observed in Figure 2.7(a) are explained by the tradeoff in the power of fuel produced ($\dot{\bar{n}}_f HHV_f$) and the pumping power that must be supplied by solar energy, Q_{pump} , shown Figure 2.7 (b). For all heat exchanger lengths, the power of the fuel and the pumping power decrease with increasing

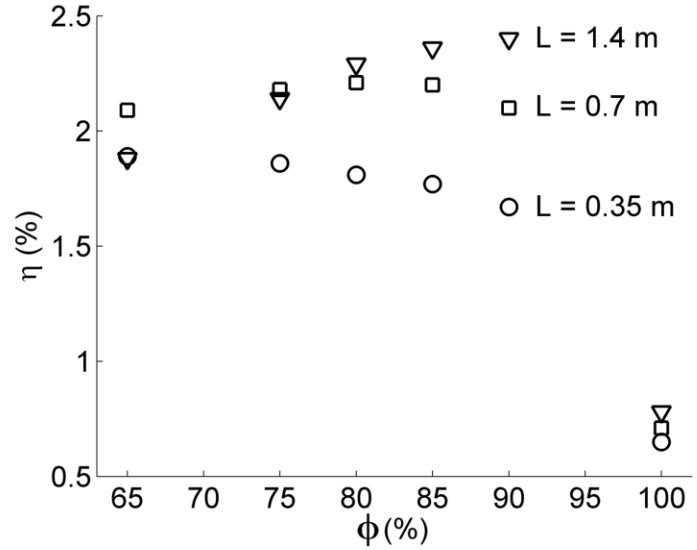

(a)

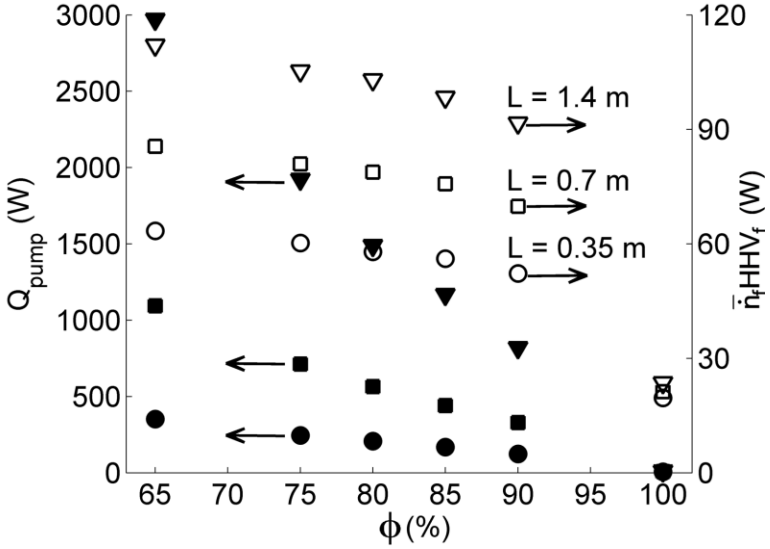

(b)

Figure 2.7. The impact of porosity for 10 PPI foam on (a) solar-to-fuel efficiency, and (b) pumping power requirement (Q_{pump}) and power content in fuel ($\dot{\bar{n}}_f \text{HHV}$). The 100% porosity data indicate the absence of RPC foam in the heat exchanger.

porosity. When the heat exchanger length is decreased, the pumping power is reduced due to a decrease in the mass of ceria accompanied by a decrease in gas flow rates (see Table 2) as well as the reduction in length. For a 1.4 m-long heat exchanger, pumping power decreases from 2971 W at ϕ = 65% to 820 W for ϕ = 90% and the reactor efficiency increases from 1.9% to 2.4%. If the heat exchanger length is halved to 0.7 m,

the highest efficiency of 2.2% is achieved with lower porosity (75% and 85%). The cost savings of decreasing the heat exchanger from 1.4 m to 0.7 m might outweigh the minimal drop in efficiency. If the heat exchanger is 0.35 m-long, the optimal RPC porosity shifts to the lowest porosities considered (65–75%) and the efficiency is 1.9%. Even at the lowest porosity of 65%, the pumping power (352 W) is $1/10^{th}$ of the pumping power for a 1.4 m long heat exchanger. As the length of the heat exchanger is reduced, the reactor efficiency is driven more by the effectiveness of heat recovery and fuel production than changes in the pumping power. Thus, the optimal porosity is shifted to lower values.

Conclusion

In this chapter, we analyze a counterflow heat exchanger comprising two concentric alumina tubes filled with reticulate porous alumina foam as a means of providing effective gas-phase heat recovery at 1773 K for a solar thermochemical process to split CO_2 via the isothermal cerium dioxide redox cycle. A steady state, conjugate heat transfer numerical model is developed to evaluate the impact of pore size and porosity of the alumina RPC and heat exchanger length on heat transfer and pressure drop. The numerical model of the heat exchanger is coupled with an overall process energy balance of the solar reactor to select the heat exchanger design and reactor operating conditions which optimize solar-to-fuel efficiency. Foam morphologies of 10, 20 and 30 PPI with porosities from 65 to 90% are considered.

The results of the CFD model highlight the significance of radiative and conductive transport in the heat exchanger. Large pores (low PPI) and high porosity minimize pressure drop and facilitate radiative transport due to improved penetration of

thermal radiation in the RPC. However, at temperatures below 700 °C, solid phase conduction dominates heat transfer, and for this reason the lowest porosity RPC yields the highest overall heat transfer coefficient. Thus while lower PPI foam is always preferred, selection of the porosity of the RPC requires consideration of the tradeoff between effectiveness of heat recovery and pressure drop on overall solar-to fuel efficiency of the integrated heat exchanger/reactor. Depending upon the heat exchanger length, which affects heat recovery effectiveness and pumping power, the RPC porosity required to optimize solar-to-fuel efficiency shifts. The longest heat exchanger studied (1.4 m) with 10 PPI, yields the highest efficiency of all the cases examined in this paper, 2.4% at 90 % porosity. Halving the length of the heat exchanger to 0.7 m only marginally decreases the efficiency to 2.2% at a reduced porosity of 75–85%. Finally, for the shortest length of 0.35 m, the highest efficiency attained is 1.9% at the lowest porosity of 65%. The fact that the mass of reactive material, RPC morphology and heat exchanger length are mutually dependent parameters to optimize process efficiency reinforces the sensitivity of solar-to-fuel efficiency to effectiveness of heat recovery and pressure drop (includes the reactive element) in recuperator.

In conclusion, the proposed counter-flow, tubular heat exchanger filled with alumina RPC shows the potential to provide adequate heat transfer and acceptable pressure drop for this application.

Chapter 3

Effect of Flow Rates on Operation of a Solar Thermochemical Reactor for Splitting CO_2 via the Isothermal Ceria Redox Cycle[4]

A prototype 4 kW_{th} solar thermochemical reactor for the continuous splitting of carbon dioxide via the isothermal ceria redox cycle is demonstrated. These first tests of the new reactor showcase both the innovation of continuous on-sun fuel production in a single reactor and remarkably effective heat recovery of the sensible heat of the reactant and product gases. Thermal impacts of gas flow selection are explored by coupling measured temperatures with a CFD model to calculate internal temperature distributions of the reactive material and estimate the gas phase heat recovery during steady periodic reactor operation.

Reactor

Cutaway views of the reactor and integrated gas phase heat recovery heat exchangers are shown in Figure 3.1. The solar receiver is a cylindrical cavity lined with six tubular assemblies. The tubular assemblies are referred to as reactive elements because they contain packed beds of ~500g of ceria pellets each, the active redox material. The reactive elements are each integrated with a ceramic tube-in-tube heat exchanger to enable gas-phase heat recovery [88,89]. The redox cycle is implemented at approximately 1773 K by alternating the flow of gases through each reactive

[4] This chapter contains my contributions from the article that has been submitted to the Journal of Solar Energy Engineering: Hathaway B. J., Bala Chandran R., Sedler S. J., Thomas D., Gladen A., Chase T. R., and Davidson J. H., 2015, "Effect of Flow Rates on Operation of a Solar Thermochemical Reactor for Splitting CO_2 via the Isothermal Ceria Redox Cycle," J. Sol. Energy Eng., *Submitted, 2015*.

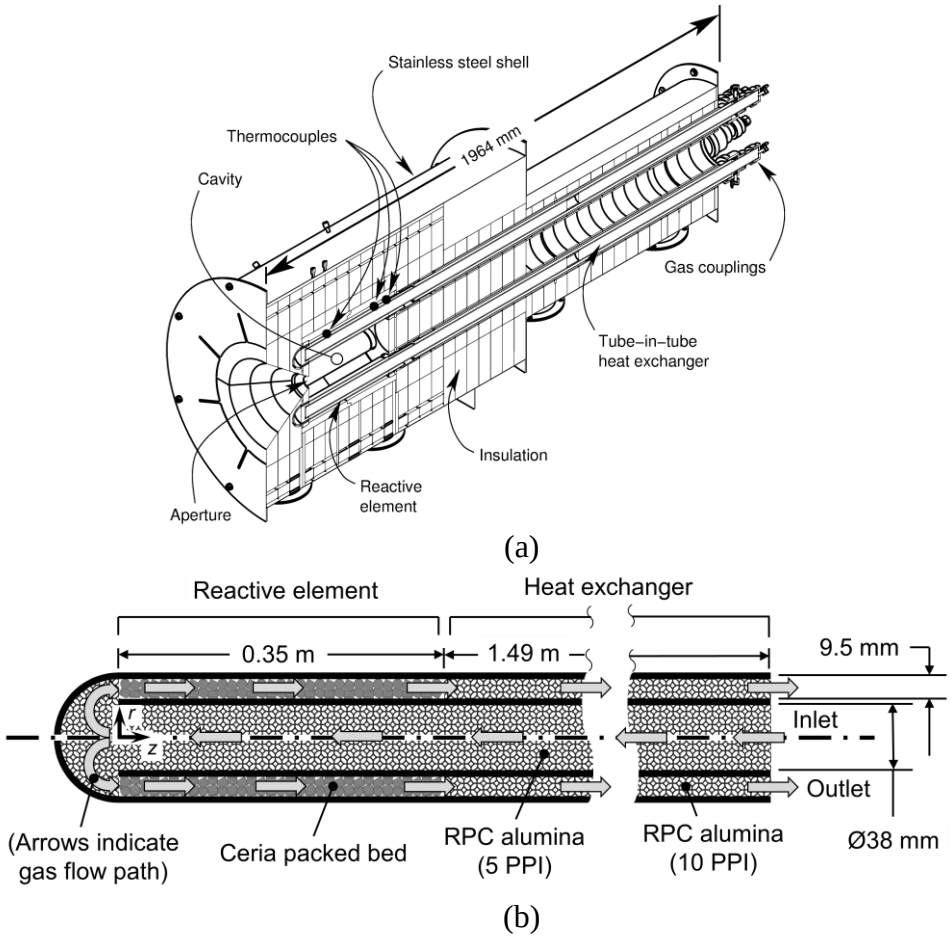

Figure 3.1 Cutaway views of the solar reactor and heat exchanger: (a) CAD model of the reactor showing the various functional components; (b) details of the reactive element and heat exchanger assembly. (Aspect ratio distorted to clarify structure of reactive element.)

element/heat exchanger assembly. During reduction an inert sweep gas flows through the centre channel of the heat exchanger and reactive element, reverses direction at the closed end of the tube assembly, flows over the ceria particles and then flows out through the annulus of the heat exchanger (see Figure 3.1 (b)). The gas flow is switched to CO_2 or steam for oxidation after 100 s of reduction. Fuel is produced continuously by operating pairs of elements in opposite half-cycle reactions, which leads to half of the reactive elements reducing and the other half oxidizing for equal durations.

The design of the cavity, the reactive elements, the heat exchangers, and supporting components are explained below. The cavity is 347 mm long and 305 mm in diameter. Concentrated sunlight enters the cavity through an open 48 mm diameter circular aperture and is absorbed by the reactive elements. For the reported experiments, the aperture intercepts 4 kW at a nominal concentration of 2200 suns, providing an approximate absorption efficiency of 75%. Each reactive element is an assembly of two concentric dense high purity (99%) alumina tubes. The outer tube has a closed spherical end at the front. The inner tube is open-ended to allow gases to flow through to the annulus.

The portion of the annulus of each reactive element that is within the solar cavity is filled with cylindrical ceria particles. The criteria for selecting particles are described in [90]. The particles are made of fibers using a proprietary process. The average particle length and diameter are 5.0 mm. The mean diameter and length of the fibers are 6 ± 16 μm and 62 ± 27 μm. The internal particle porosity is 81%, measured via porosimetry and the specific surface area is 0.14 $m^2 g^{-1}$, which is measured using Brunauer–Emmett–Teller **(**BET) krypton adsorption that applies the theory of multilayer adsorption of gas molecules on a solid surface. The void fraction of the packed bed is 45%.

The concentric tube heat exchangers were designed to provide an effectiveness of 92% during oxidation (for a flow rate of 0.34 mol $s^{-1} g^{-1}$ CO_2 with a pressure drop of 5 kPa), and 87% during reduction (for flow rate of 1 mol $s^{-1} g^{-1}$ N_2 and pressure drop of 18 kPa) [89]. Both flow passages are filled with reticulated porous alumina foams to enhance radiative and convective heat transfer. The foam in the annulus has a fluid

accessible[5] porosity of 85–90% and 10 PPI (mean pore diameter of 2.5 mm). The foam in the inner tube is 85–90% porous and 5 PPI (mean pore diameter of 5.1 mm). In the present work, we report measured steady state performance of the heat exchanger.

The insulation system, sized using a 3-D, steady-state analysis, is designed to restrict the conduction heat losses from the reactor cavity to about 450 W, assuming a cavity surface temperature of 1773 K. The reactor is housed in a 1.5 mm thick, stainless steel shell to protect the insulation.

Transient Model of integrated reactive element/heat exchanger

Temperatures are measured on the outer surfaces of the integrated reactive element/heat exchanger. Therefore, interpretation of the experimental data is aided by a numerical model, which provides the temperature distributions along the flow path of the gases in the reactive element and the heat exchanger. The model predictions of the gas temperatures are used to determine the sensible heating requirements and also to estimate the temperature swings in the gases/ceria during cycling.

A model of the heat exchanger described by Bala Chandran et al. [89] (described in Chapter 2) is expanded to include the transient convective and radiative heat transfer within the reactive element as gas flows are switched during redox cycling. The expanded model is coupled to the experiment by applying the transient, axial profiles of temperatures measured along the outer tube wall of the reactive element and the heat exchanger, $T_w(z,t)$, as time-dependent boundary conditions. The computational domain is two-dimensional, axisymmetric (Figure 3.1) and comprises the tube-in-tube reactive

[5] Fluid accessible porosity has characteristic pore scale lengths on the order of millimeters as compared to the micrometer pores in the struts of the alumina RPCs.

element with the packed bed of ceria particles in the annulus and is connected to the counter flow heat exchanger filled with RPC alumina.

The packed bed of ceria and the alumina RPC in the heat exchanger are treated as homogeneous, and isotropic. The effective transport properties are determined as functions of the material morphology — $\phi_{\text{bed}}, \phi_{\text{particle}}, d_{\text{ceria}}$, in the bed of ceria particles, and PPI and ϕ_{RPC} of the alumina RPC in the heat exchanger, from existing correlations [58,89]. The techniques applied to model the continuum transport in the packed bed of ceria particles are detailed in [58].

The transient, mass conservation equation in the porous medium is given by,

$$\frac{\partial \rho_f}{\partial t} + \nabla \cdot \left(\rho_f \boldsymbol{u}\right) = 0, \tag{1}$$

and the species transport equation is solved for a mixture of O_2, CO_2 and N_2,

$$\frac{\partial \left(\phi \rho_f Y_i\right)}{\partial t} + \nabla \cdot \left(\rho_f \boldsymbol{u} Y_i\right) = \nabla \cdot \left(D_{i,\text{eff}} \nabla Y_i\right), \tag{2}$$

where i = O_2, CO_2 and the additive law of species mass fractions is used to determine Y_{N_2}.

The transient, momentum conservation equation for fluid flow in the porous medium is given in eq.(3), where, ϕ is the inter-particle void space in the ceria packed bed/ the fluid accessible porosity in the alumina RPC [60].

$$\begin{aligned} &\frac{1}{\phi}\frac{\partial}{\partial t}\left(\rho_f \boldsymbol{u}\right) + \frac{1}{\phi^2}\nabla \cdot \left(\rho_f \boldsymbol{u}\boldsymbol{u}\right) \\ &\qquad = -\nabla p + \frac{1}{\phi}\nabla \cdot \left(\mu \nabla \boldsymbol{u}\right) - \frac{\mu}{K}\boldsymbol{u} - \rho_f C_E |\boldsymbol{u}| \boldsymbol{u} \end{aligned} \tag{3}$$

The extended Darcy-Brinkman-Forchheimer formulation [60] for momentum transport utilized here includes the pressure drop due to the presence of walls and interfaces confining the porous medium, shear stresses from the pore walls and the

inertial drag forces. The species transport equation is modeled to simulate N_2 (with 10 ppm O_2) and CO_2 flows during reduction and oxidation, without accounting for chemical reactions. The temperature field is not greatly affected by the energy sinks/sources from the chemical reactions as the sensible energy requirement is ten-fold, based on experimentally measured rates of CO production [15,58].

Heat transfer through the packed bed and the RPC alumina is modeled by assuming local thermal equilibrium (eq. (4)),

$$\frac{\partial}{\partial t}\left(\phi_{\text{eff}}\rho_f \sum_i Y_i h_{if} + \left(1-\phi_{\text{eff}}\right)\rho_s h_s\right) + \nabla\cdot\left(\rho_f \boldsymbol{u}\sum_i Y_i h_{if}\right) = \nabla\cdot\left(\left(k_{\text{s,eff}} + k_{\text{f,eff}}\right)\nabla T\right) - \nabla\cdot q_{\text{rad}}. \quad (4)$$

The transient energy storage terms for the fluid and solid phases are determined using the effective volume fraction, ϕ_{eff} in the packed bed of ceria and alumina RPC. The radiative source term, $\nabla\cdot q_{\text{rad}}$, is determined using the P_1 method [67] by evaluating the incident radiation on a control volume as detailed in [89] and Chapter 2. To model radiative transport, the porous medium is treated as an absorbing-scattering-emitting homogenous medium with isotropic, gray, diffuse radiative properties. The annulus thickness and inner tube diameter are used as the length scales to evaluate the optical thickness (see Chapter 2). It is reasonable to apply the P_1 approximation as optical thicknesses are greater than 1 for the packed bed and alumina RPC inside the centre channel and annulus (1, 2.5 and 5 respectively) [67].

In the dense alumina tube walls (outer and inner tube), the transient, two dimensional (2-D), conduction equation is solved and the wall surfaces are treated as

opaque and grey, with a surface emissivity (spectrally weighted at 1773 K) of 0.6 obtained from experimental data [63] at temperatures up to 2200 K.

The model is used to simulate steady-periodic operation for sweep gas and oxidizer flow rates of 0.67×10^{-4} mol s^{-1} g^{-1}. The time dependent mass flow rate and the composition of the gases are specified as step inputs at the inlet to simulate the reduction and oxidation half-cycles as,

$$\dot{m}_{in}(t) = \begin{cases} \dot{m}_{\mathrm{rd}} = 0.931\ \mathrm{g\ s^{-1}} & t \in (0, t_{\mathrm{rd}}] \\ \dot{m}_{\mathrm{ox}} = 1.45\ \mathrm{g\ s^{-1}} & t \in (t_{\mathrm{rd},} t_{ox}] \end{cases} \tag{5}$$

$$X_{\mathrm{O_2,in}}\,(t), X_{\mathrm{CO_2,in}}(t) = \begin{cases} 10^{-5}, 0 & t \in (0, t_{\mathrm{rd}}] \\ 0{,}1 & t \in (t_{\mathrm{rd},} t_{ox}] \end{cases} \tag{6}$$

The spatial temperature profile of the outer tube wall in the reactive element is obtained by linear interpolation of the temperature measurements at any two axial locations and a third order polynomial equation (R^2=0.996) is used to fit the measured axial temperature profiles in the heat exchanger. The gases enter the inner tube of the integrated reactive element/heat exchanger at 300 K and are stipulated to leave the heat exchanger annulus at atmospheric pressure (1 atm). Temperature dependent [81,82], thermophysical properties (specific heat, thermal conductivity and viscosity) of the gas mixture are obtained by applying the ideal gas mixing law for the pure species. Mass diffusivity of the gas is obtained from kinetic theory for rigid spheres [91]. On the solid walls, a no slip boundary condition is imposed for the velocity field and continuity of temperature and heat flux is implemented. The effect of contact resistance between the tube walls and the porous ceria particles and alumina RPC is not modeled due to the predominance of radiative heat transfer at high temperatures. For the incident radiation, Marshak's

condition for direction integrated radiative heat flux is imposed at all wall boundaries [67].

The field variables $(\boldsymbol{u}, p, T \; and \; Y_i)$ in the numerical domain are initialized to the steady-state values obtained when 100% CO_2 flows through the reactive element/heat exchanger, where, $T_w(z)$ is equal to the wall temperatures measured at the end of the oxidation step. The model is solved using Ansys Fluent 15.0 with a mesh of quadrilateral elements except within a small region inside the domed end of the reactive element where a combination of quadrilateral and triangular elements are used. A maximum of 20,000 elements is used with grid refinement close to the solid walls. A first-order, Euler implicit scheme is used for time integration with a time step of 1 s. For a spatially refined mesh with ~40,000 elements the average temperature results changed by less than 2%. The SIMPLE algorithm couples the pressure and the velocity fields [83], with second order upwinding for the advection terms in the momentum, energy and incident radiation equations. The governing equations are solved in a sequential manner with the globally scaled residual values for convergence set to 10^{-10} for all transport equations, including radiative transfer. At every time step up to 35 iterations are performed to satisfy mass conservation and to ensure that the changes in volumetric average of the temperatures of the ceria bed and alumina RPC are less than 0.1 K.

Heat Exchanger Performance Evaluation

The reactor was operated at steady-state at gas flow rates of 0.67×10^{-4} mol s^{-1} g^{-1} to provide data required for the numerical simulations to evaluate the temperature distribution in the gases in the packed bed of ceria and the heat exchanger during steady-cycling. Figure 3.2 presents the spatial averages of the measured wall temperatures and

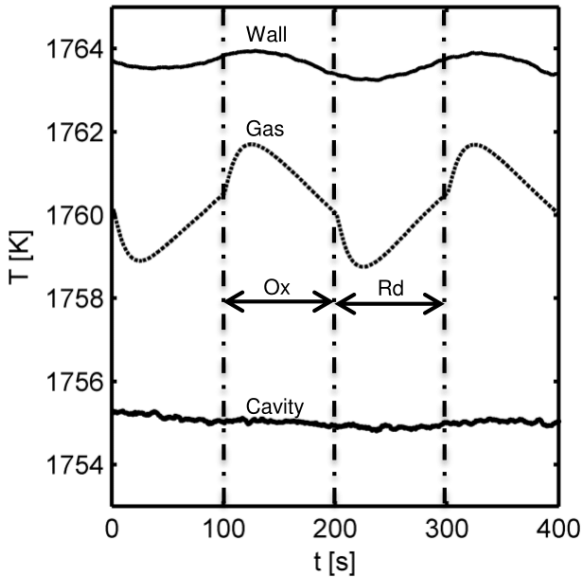

Figure 3.2 Temperatures in the reactive element for two cycles of steady-periodic reactor operation with 0.67×10^{-4} mol s^{-1} g^{-1} of sweep gas and CO_2. Spatially averaged, measured wall surface temperatures, model predicted bulk gas temperatures and measured cavity temperature are shown. Oxidation and reduction half cycles are abbreviated as 'Ox' and 'Rd'.

the simulated bulk mean gas temperatures in the packed bed of ceria for two representative cycles during steady-periodic operation. The spatially averaged reactive element surface temperature is 1763 ± 0.7 K with temperatures increasing during reduction and decreasing during oxidation. This is due to the relatively higher thermal capacity of the oxidizer as compared to sweep gas, i.e. $\dot{n}\bar{c}_{p,ox} \sim 1.5\dot{n}\bar{c}_{p,sg}$. The average cavity surface temperatures are stable at 1755 K. Using the measured wall temperatures along the length of the reactive element as boundary conditions, the CFD model predicts the bulk mean temperatures of the gases in the ceria bed. The gas temperatures drop in the first 20 s of reduction and increase from 1759 to 1761 K during the remaining reduction period. And, during oxidation, the temperature decreases from a peak value of 1762 to 1760 K. A small but thermodynamically favorable temperature swing of 1 K is obtained between the end states of reduction and oxidation. Due to the relatively small

swing in non-stoichiometry of 0.0031, the cycle-averaged energy sink/source (15/7 W) during reduction/oxidation are small and hence the internal energy changes are driven more by the convective heat transfer rates. The sensible heating loads during reduction and oxidation are evaluated from the spatial distribution of the bulk gas temperatures along the flow path in the integrated reactive element/heat exchanger (see Figure 3.3). As the spatial variations of the gas temperatures maintain similar trends throughout cycling, the profile is described at a single time instant during onset of reduction. Sweep gas enters the centre channel at ambient temperature and is preheated to the desired operating temperature of 1773 K before coming in contact with the ceria particles. Due to mixing in the porous media and effective radiative transport, heat transfer within the ceria bed facilitates the gas temperatures to be within 15 K of the outer tube walls. The gas cools down to 1715 K before leaving the ceria bed (see subplot in Figure 3.3). High heat transfer rates are achieved between the hot and cold sides as a result of enhanced heat transfer surface area in the RPCs and rapid radiative transport at temperatures greater than 1000 K [89]. As predicted by design calculations [89] and prior measurements in a prototype [88], we are able to achieve highly effective gas phase heat recovery. The effectiveness,

$$\varepsilon_{\{\mathrm{sg,ox}\}} = \frac{\bar{h}_{\{\mathrm{sg,ox}\}}\left(T_{\mathrm{c,out}}\right) - \bar{h}_{\{\mathrm{sg,ox}\}}(T_{\mathrm{amb}})}{\bar{h}_{\{\mathrm{sg,ox}\}}\left(T_{\mathrm{h,in}}\right) - \bar{h}_{\{\mathrm{sg,ox}\}}(T_{\mathrm{amb}})}, \tag{7}$$

varies steady-periodically due to the cycling of gases with different thermal capacitances. It increases from 90% to 93% during reduction and drops to 90% at the end of oxidation. During a steady reduction-oxidation cycle, $T_{\mathrm{c,out}}$ varies from 1540 K to 1577 K and $T_{\mathrm{h,in}}$ is in the range of 1715–1713 K. Therefore using the equation,

$$\dot{Q}_{\{\mathrm{sg,ox}\}} = \frac{\dot{n}\bar{c}_{\mathrm{p},\{\mathrm{sg,ox}\}}}{2}\left(T_{\mathrm{h,in}} - T_{\mathrm{c,out}}\right), \tag{8}$$

the cycle-averaged power required, per reactive element, for sensible heating is 86 W and 166 W. The net power for sensible heating predicted from the measured temperatures is only 50 W more than the estimates projected by the steady-state heat exchanger model [89] (less than 3% difference on the predictions of the effectiveness), which assumes 1773 K for the hot side inlet temperature. Because of the very slight differences in the steady-state heat exchanger model predictions and the measured values, the model was applied to evaluate the sensible heating requirements for the two other gas flow rates explored in the experimental tests (not discussed here).

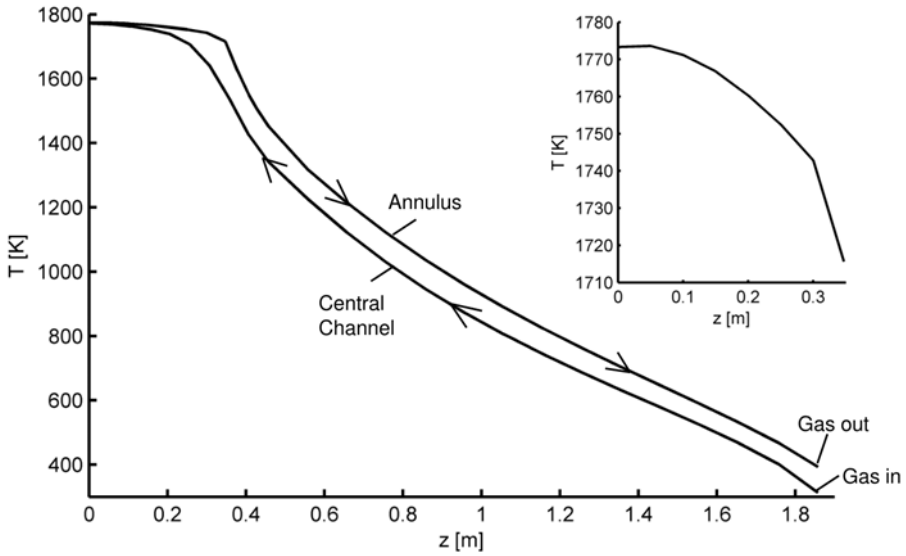

Figure 3.3 Axial variation of model predicted bulk gas temperatures along its flow path in the central channel and the annulus at the onset of reduction with a sweep gas flow rate of 0.67×10^{-4} mol s^{-1} g^{-1}. Subplot shows the axial temperature variation in the packed bed of ceria.

The model predictions for the pressure drop between the gas inlet and outlet is 6.4 kPa and 8.5 kPa during reduction and oxidation, which matches well with the measured data (6.2 kPa and 9.2 kPa). By using a mass transport limited, thermodynamic

model presented by De Smith [92], the fuel production rates can be obtained for a specified set of operating conditions for a differential reactor comprising ~1 g of ceria. Compared to operation at atmospheric pressure, the measured pressure drops results in a less than 3% decrease in the fuel production rate. The predicted gas outlet temperatures — 410 K and 395 K during reduction and oxidation, are within 5% of the measured outlet gas temperatures of 400 and 390 K. This agreeable comparison of model results against experimental measurements instills confidence in the model formulation and the correlations applied for effective transport properties in the reactive element/heat exchanger.

In sum, these first tests of the new reactor showcase both the innovation of continuous on-sun fuel production (not presented here) in a single reactor and remarkably effective heat recovery of the sensible heat of the reactant and product gases. High effectiveness of 90–93% are measured during steady periodic cycling, validating the design of the heat exchanger previously tested only at small scale [88].

Chapter 4

Model of Transport and Chemical Kinetics in a Solar Thermochemical Reactor to Split Carbon Dioxide

Solar thermochemical reactors to carry out the nonstoichiometric reduction and oxidation of cerium dioxide (ceria) produce hydrogen and carbon monoxide from water and carbon dioxide. Here we present a computational model of a prototype solar thermochemical reactor that implements an isothermal, pressure-swing nonstoichiometric ceria redox cycle. Unique features of the reactor are continuous production of fuel and highly effective gas-phase heat recovery. The transient three dimensional model couples radiation heat transfer to cyclic heat and mass transport processes and chemical kinetics for carbon dioxide splitting within a fixed bed of porous ceria particles. Reaction rate coefficients are extracted from small-scale experiments in an infrared furnace. The predicted radiative flux, velocity, temperature and species concentration fields during steady-periodic operation provide insight to the effects of transport processes and optical properties on fuel production and efficiency of conversion of sunlight to fuel. For a solar input of 4.2 kW, reduction carried out in a nitrogen flow of 0.67×10^{-4} mol s^{-1} g_{ceria}^{-1} and oxidation at the same molar flow rate of CO_2, the reactor achieves nearly isothermal cycling at 1791 K with continuous CO production of 3.6×10^{-4} mol s^{-1}. The overall reaction rates are driven by advective mass transport rates and the intrinsic material thermodynamics. Heat recovery of more than 90% of the sensible heat of the reactant and product gases is achieved. Predicted fuel production rates compare favorably (within 20%) to measured data.

Introduction

A sustainable approach to produce synthetic fuels and to store solar energy in chemical form is to use concentrated sunlight to split water and carbon dioxide via thermochemical metal-oxide redox cycles. Excellent reviews of solar redox cycles are available in recent publications [2–4]. The products, hydrogen and carbon monoxide, can be combusted directly, used in a fuel cell, or further processed to liquid fuels, hence providing a pathway to convert the abundant yet intermittently available energy from the sun into a storable and transportable fuel.

In the present study we consider conversion of sunlight to fuel via the cerium dioxide (ceria) redox cycle [7,93]. Ceria undergoes partial reduction in an endothermic reaction at temperatures above 1600 K in a low oxygen partial pressure environment (eq. 1). Hydrogen and carbon monoxide are produced via the exothermic reactions (2a,b) when the reduced ceria is reoxidized with H_2O and CO_2.

$$\mathrm{CeO}_{2-\delta_{\mathrm{ox}}} = \mathrm{CeO}_{2-\delta_{\mathrm{rd}}} + \frac{\delta_{\mathrm{rd}} - \delta_{\mathrm{ox}}}{2}\,\mathrm{O}_2 \tag{1}$$

$$\mathrm{CeO}_{2-\delta_{\mathrm{rd}}} + (\delta_{\mathrm{rd}} - \delta_{\mathrm{ox}})\,\mathrm{H_2O} = \mathrm{CeO}_{2-\delta_{\mathrm{ox}}} + (\delta_{\mathrm{rd}} - \delta_{\mathrm{ox}})\,\mathrm{H_2} \tag{2a}$$

$$\mathrm{CeO}_{2-\delta_{\mathrm{rd}}} + (\delta_{\mathrm{rd}} - \delta_{\mathrm{ox}})\,\mathrm{CO_2} = \mathrm{CeO}_{2-\delta_{\mathrm{ox}}} + (\delta_{\mathrm{rd}} - \delta_{\mathrm{ox}})\,\mathrm{CO} \tag{2b}$$

Fuel is produced in proportion to the change in the non-stoichiometry between reduction and oxidation, $\delta_{\mathrm{rd}} - \delta_{\mathrm{ox}}$. In the present study, we investigate a “nearly isothermal”, pressure swing redox cycle [20,23–25,15]. The driving potential to produce fuel is generated at approximately 1773 K by maintaining low O_2 partial pressures during reduction (~10 Pa) via an inert sweep gas. The isothermal redox cycle is an alternative to the “temperature swing” cycle in which reaction (2) is carried out after cooling the ceria by hundreds of degrees to produce a larger difference in nonstoichiometry [10–12,20,35].

Although the temperature swing cycle is favored by the material thermodynamics [9], it requires recovery of the sensible heat of the ceria to avoid irreversible heat losses during cycling [10,16,20]. However, solid phase heat recovery has proven difficult to implement in solar thermochemical reactors. Proposed reactor concepts for solid phase heat recovery require moving components that are subjected to large thermal gradients [21,22,94,95]. The isothermal cycle eliminates the need for solid phase heat recovery between the reaction steps, reduces thermal stresses in the reactor components and simplifies the overall reactor design. The efficiency of both isothermal and temperature swing cycles will gain from gas phase heat recovery.

At the University of Minnesota, we have developed a 4 kW_{th} solar reactor prototype with integrated gas phase heat recovery to implement the isothermal ceria redox cycle and have demonstrated continuous, production of CO from CO_2 [31]. Prior publications present the supporting analyses for design and operation of the reactor [14,15,31] and the gas heat recovery system [59,89]. In the present study, we present a transient, three-dimensional (3-D) numerical model of the reactor that couples heat and mass transport processes with the chemical reactions for splitting CO_2. Surface reaction rate coefficients are extracted from experimental data for an isothermal bench top reactor [15]. Prior numerical transport models for isothermal and temperature swing ceria-based reactors are limited in scope to heat transfer analyses [21,22,27] or only consider kinetics for the reduction step [28–30].

Reactor

The reactor (Figure 4.1) has a cylindrical receiver cavity lined with six tubular reactive elements each integrated with a ceramic heat exchanger. Concentrated sunlight enters the 347 mm long, 305 mm diameter cavity through an open 42 mm diameter aperture. Each reactive element is a concentric assembly of two alumina tubes. Within the solar cavity, the annulus is filled with 590 g of 5 mm cylindrical, ceria particles. The particles are 75% porous and the void fraction in the packed bed is 45%. The tubular assemblies extend beyond the solar cavity to integrate with a tubular heat exchanger. The heat exchanger tubes are filled with alumina reticulate porous ceramic (RPC) to enhance heat transfer [89]. The alumina RPC has a fluid accessible porosity of 85–90% and pore densities of 10 and 5 PPI (pores per inch) in the annulus and centre channel of the heat exchanger, respectively. During reduction, an inert N_2 sweep gas is passed through the heat exchanger and then through the ceria bed. The inlet gas is preheated by the hot gases leaving the reactive element. During oxidation, the gas flow is switched to pure CO_2. Fuel is produced continuously by alternating the gas flows between reactive elements. The design gas flow rates and cycling period are set to maximize reactor thermal efficiency and fuel productivity [15,31]. The design flow rates are 0.67×10^{-4} mol s^{-1} g_{ceria}^{-1} of N_2 and CO_2 for a 200 s cycle equally split between reduction and oxidation. The reactor is well insulated to reduce thermal losses to the ambient. Based on operation of the reactor, thermal losses are anticipated to equal 35% of the absorbed solar energy [31].

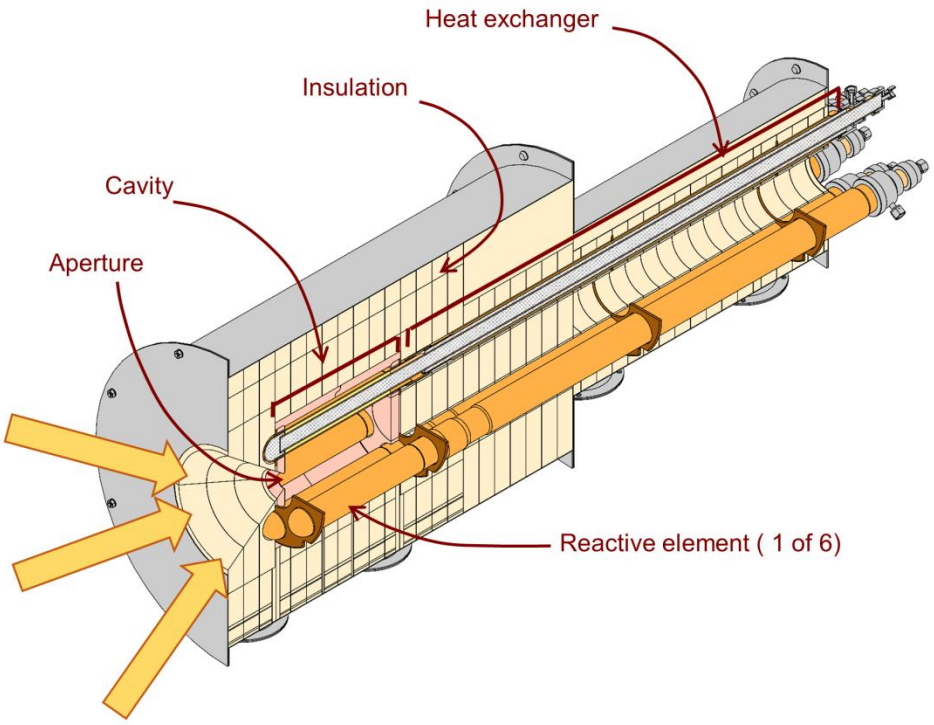

(a)

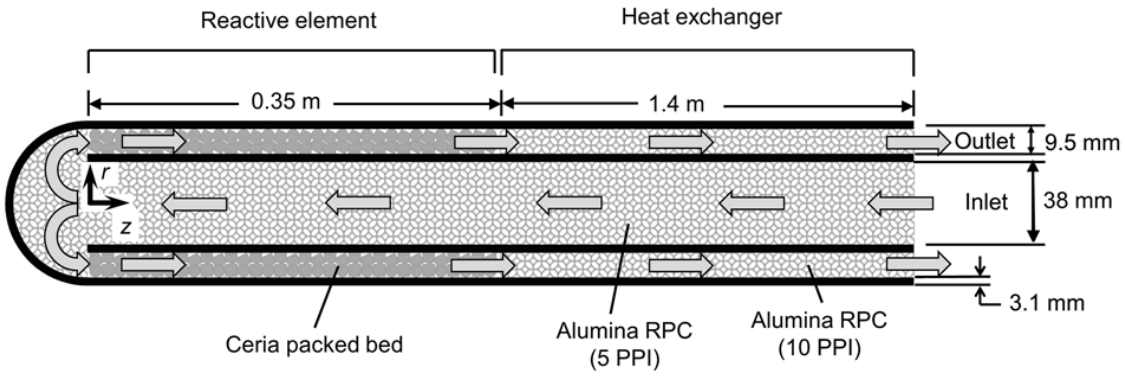

(b)

Figure 4.1 Cross section of the solar reactor: (a) overview showing the cavity and integrated heat exchanger and (b) details of the reactive element and heat exchanger assembly. Arrows indicate gas flow direction. (The aspect ratio is distorted to better visualize the reactive element.)

Approach

Reactor Model

The transient, 3-D model is developed in Ansys Fluent 15.0 [96]. To make the problem more tractable, the computational domain is a 60° angular sector of the reactor cavity with two adjacent reactive elements in opposing states of reduction and oxidation (Figure 4.2). These two reactive elements will be referred to as "RE1" and "RE2" in the rest of this chapter. Symmetry conditions are applied on the planes AB and AC supported by two assumptions. Incident radiation is distributed uniformly at the aperture. Thermal losses are modeled by a uniformly distributed overall loss coefficient as shown in Figure 2. The modeled length of the reactive element (Figure 4.1 (b)) extends to z = 0.38 m. Inclusion of the entire length of the heat exchanger would greatly increase the computing time. To address this issue, the reactor model is used in conjunction with a separate CFD model of the heat exchanger [89]. Iterations are performed between the two models until the changes in the inlet and outlet temperatures of the 3-D model are less than 2%.

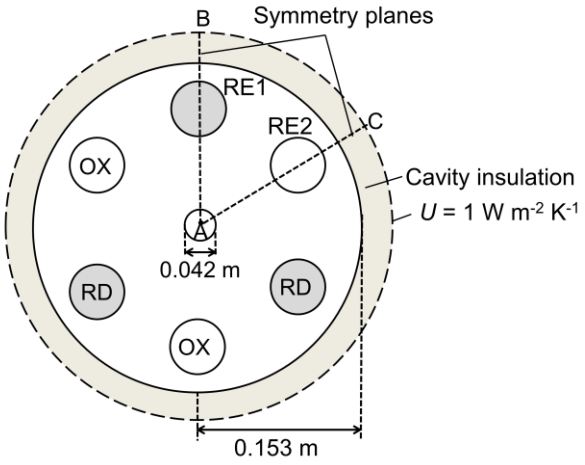

Figure 4.2 Computational domain viewed from the aperture showing the symmetry planes. Two of the six reducing (RD) and oxidizing (OX) reactive elements (RE1 and RE2) are simulated in the model. Figure is not to scale.

Radiative heat transfer is incorporated via a combination of Monte Carlo ray tracing for the incident solar radiation and a discrete ordinates model [97,98] to simulate emitted radiation. As a base reference case, the porous cavity surface is assumed to be black, and the alumina tube surfaces are treated as opaque, grey-diffuse with an assumed emissivity of 0.7 based on available data for alumina at temperatures up to 2200 K [99]. As discussed briefly in the results, a second case is considered for more reflective materials. The incident solar power is 4.2 kW with a concentration of 3000 suns (1 sun = 1 kW m^{-2}) and a half cone angle of 37.7° at the aperture to match the test conditions in the University of Minnesota high flux simulator [100]. The input power is selected based on an overall energy balance on the reactor [15,89].

The collision based Monte Carlo simulation launches at least 10^7 rays from the reactor aperture and tracks the absorbed component of the incident solar radiation on at the surface of the cavity and reactive elements. Because the optical properties are assumed to be temperature independent, the solar ray-tracing step can be decoupled from the fluid flow, heat and mass transfer in the reactive elements. The absorbed solar energy is incorporated as volumetric heat sources across thin slices of the reactor surfaces. The aperture is assumed to be cold and black for the emitted radiation from the solar cavity. The finite volume method for radiation computes the emitted radiation from the heated reactor surfaces and yields computational advantages by using the same spatial mesh as the CFD solver [101]. In addition to the spatial domain, the angular domain of 4π steradians is divided into discrete, non-overlapping solid angles (Ω_i) and the radiative transport equation is integrated over the volume element, V, and solid angle Ω_i as,

$$\int_{\Omega_i}\int_{\Gamma} I\,\hat{s}\cdot\hat{n}\,d\Gamma\,d\Omega_i = \int_{\Omega_i}\int_{V}(\kappa I_b - \beta I)\,dV\,d\Omega_i + \int_{\Omega_i}\int_{V}\frac{\sigma}{4\pi}\int_{4\pi}\Phi\left(\hat{s}',\hat{s}\right)I\left(\hat{s}'\right)d\Omega'\,dV\,d\Omega_i. \tag{3}$$

Pixelization is included on the control angles that do not align with the control volume faces [96,102] to divide the intensities into outgoing and incoming components. The air in the cavity is treated as non-participating.

The ceria particles and the alumina RPC are assumed homogenous and isotropic. The gases are ideal and incompressible. Using the superficial or the Darcy velocity, the Reynolds number based on the centre channel hydraulic diameter is less than 700 and the pore-scale Reynolds number in the packed bed of ceria and RPC alumina is less than 60. Transient, continuum transport equations are solved with effective transport properties determined from published correlations for packed beds [103] and RPCs [49,68,78] (see Table 3). The permeability[6] for flow of gases through the particle is much lower than that for flow around the mm-sized ceria particles; 10^{-13} vs. 10^{-8} m^2. Therefore, the model simulates gas flow around the particles yielding the volume-averaged mass and momentum conservation equation as,

$$\frac{\partial\rho_f}{\partial t} + \nabla\cdot\left(\rho_f\boldsymbol{u}\right) = \sum_i \dot{r}_i, \tag{4}$$

$$\frac{1}{\phi}\frac{\partial}{\partial t}\left(\rho_f\boldsymbol{u}\right) + \frac{1}{\phi^2}\nabla\cdot\left(\rho_f\boldsymbol{u}\boldsymbol{u}\right) = -\nabla p + \frac{1}{\phi}\nabla\cdot\left(\mu\nabla\boldsymbol{u}\right) - \frac{\mu}{K}\boldsymbol{u} - \rho_f C_E|\boldsymbol{u}|\boldsymbol{u}\,. \tag{5}$$

The pressure drop due to the presence of walls and interfaces confining the porous medium, shear stresses from the pore walls and the inertial drag forces are included in eq. (5) [103]. The porosity in eq. (5) equals ϕ_{bed} in the packed bed of ceria and ϕ_{RPC} for

[6] Permeability for the flow gases through a particle is computed using the formulation given in Table 3 for packed beds with a length scale of 10 μm.

Table 3 Effective transport properties for the packed bed of ceria and alumina RPC.

Effective Transport Property	Equation	Value
	Packed bed $\phi_{\text{bed}} = 0.45$; $\phi_{\text{particle}} = 0.75$; $d_{\text{ceria}} = 5\times10^{-3}$ m	
K (m^2)	$\frac{\phi_{\text{bed}}^3 d_{\text{ceria}}^2}{180(1-\phi_{\text{bed}})^2}$ [103]	4.2×10^{-8}
C_E (m^{-1})	$\frac{1.8\,(1-\phi_{\text{bed}})}{\phi_{\text{bed}}^3 d_{\text{ceria}}}$ [103]	2112.5
$k_{\text{s,eff}}$ at 1773 K (W m^{-1} K^{-1})	$k_s(1-\phi_{\text{bed}})(1-\phi_{\text{particle}})$ [103]	0.12
β(m^{-1})	$\frac{3(1-\phi_{\text{bed}})}{d_{\text{ceria}}}$ [104,105]	330
ω (-)	1	1
	Alumina RPC $\phi_{\text{RPC}} = 0.85$; 10/5 PPI RPCs	
K (m^2)	$0.0073(1-\phi_{\text{RPC}})^{-0.224}\left(\frac{d_f}{d_p}\right)^{-1.11} d_p^2$ $d_p = \frac{0.0254}{\text{PPI}}$; $d_f = 1.18\sqrt{\frac{1-\phi_{\text{RPC}}}{3\pi}}\frac{d_p}{1-e^{-\frac{1-\phi_{\text{RPC}}}{0.04}}}$ [68,69]	5.8×10^{-8}/2.3×10^{-7}
C_E (m^{-1})	$\frac{0.3a_{sf}}{\phi_{\text{RPC}}^2}$; $a_{sf} = \frac{3\pi d_f\left(1-e^{-\frac{1-\phi_{\text{RPC}}}{0.04}}\right)}{0.59 d_p^2}$ [68,69]	775/387
$k_{\text{s,eff}}$ at 1773 K (W m^{-1} K^{-1})	$\frac{0.8k_s}{3}(1-\phi_{\text{RPC}})$ [78]	0.25
β(m^{-1})	$\frac{4.4(1-\phi_{\text{RPC}})}{d_{\text{p}}}$ [65]	260/520
ω (-)	0.81 [66]	0.81

the alumina RPC. The species conservation equation is

$$\frac{\partial\left(\phi_{\text{eff}}\rho_f Y_i\right)}{\partial t} + \nabla\cdot\left(\rho_f \boldsymbol{u} Y_i\right) = \nabla\cdot\left(D_{i,\text{eff}}\nabla Y_i\right) + \dot{r}_i, \tag{6}$$

where, $\dot{r}_i$ is the rate of production/consumption of species i = O_2, CO and CO_2. The binary mass diffusivities, D_{ij} , of the gases are obtained by applying the Chapman-

Enskog theory [91] and the diffusion coefficient for species *i* in the multicomponent mixture is,

$$D_i = \frac{1 - X_i}{\sum_{j \neq i} \frac{X_i}{D_{ij}}}. \tag{7}$$

Effective diffusivity is ϕD_i and the inter-particle void fraction is considered in the particle bed.

Heat transfer through the packed bed and the RPC alumina is modeled by assuming local thermal equilibrium:

$$\frac{\partial}{\partial t}\left(\phi_{\text{eff}}\rho_f \sum_i Y_i h_{if} + (1-\phi_{\text{eff}})\rho_s h_s\right) + \nabla \cdot \left(\rho_f \boldsymbol{u} \sum_i Y_i h_{if}\right) = \nabla \cdot \left(\left(k_{\text{s,eff}} + k_{\text{f,eff}}\right)\nabla T\right) - \nabla \cdot \boldsymbol{q}_{\text{rad}} + \dot{S}_{\text{rxn,\{rd/ox\}}} \tag{8}$$

For the packed bed and the alumina RPC, the differences in the gas/solid temperatures between the thermal equilibrium and non-equilibrium formulations are expected to be less than 10% and 3% respectively, based on the dimensionless numbers that compare the thermal resistances for solid phase conduction, interfacial heat transfer and fluid phase conduction [106]. Moreover, the temperature variation over the system dimension, i.e. the thickness of the annulus and the radius of the centre channel, is expected to be larger than the pore level difference in the solid and fluid phase temperatures [107]. The transient energy storage terms for the fluid and solid phases are determined using the effective volume fraction,

$$\phi_{\text{eff}} = 1 - \left(1 - \phi_{\text{particle}}\right)(1 - \phi_{\text{bed}}), \tag{9}$$

in the packed bed and $\phi_{\text{eff}} = \phi_{RPC}$ in the alumina RPC. The energy sink/source terms due to chemical reactions in the packed bed of ceria (eq. (5) and (6)),

$$S_{\mathrm{rxn,rd}} = -\frac{\dot{r}_{\mathrm{O_{2,ceria}}}}{M_{\mathrm{O_2}}}\bar{h}_{O_{2,\mathrm{ceria}}}(\delta), \tag{10}$$

$$S_{\mathrm{rxn,ox}} = \frac{\dot{r}_{\mathrm{O_{2,ceria}}}}{M_{\mathrm{O_2}}}\bar{h}_{O_{2,\mathrm{ceria}}}(\delta) - \frac{\dot{r}_{\mathrm{CO,diss}}}{M_{\mathrm{CO}}}\bar{h}_{\mathrm{diss}}(T), \tag{11}$$

with the absolute values of the reaction enthalpies. For the expected range of ceria nonstoichiometry (0.02–0.04 at 1773 K), the energy required for the reduction of ceria, $\bar{h}_{\mathrm{O_{2,ceria}}}$, is 910–860 kJ $\mathrm{mol_{ceria}^{-1}}$ and $\bar{h}_{\mathrm{diss}}$ is 279 kJ $\mathrm{mol_{CO_2}^{-1}}$. The packed bed and the RPC are treated as participating media with isotropic, gray and diffuse radiative properties. The radiative source term $\nabla \cdot \boldsymbol{q}_{\mathrm{rad}}$ is computed using the finite volume method for unstructured meshes [97,98] and the radiative flux vector in a control volume, *p*, is evaluated as a discrete sum over *i* angular directions,

$$\boldsymbol{q}_{p,\mathrm{rad}} = \sum_i I_{pi}\boldsymbol{s}_i\,, \tag{12}$$

$$\boldsymbol{s}_i = \int_{\Omega_i} \hat{\boldsymbol{s}}\, d\Omega\,. \tag{13}$$

The packed bed extinction coefficient is determined by applying geometric optics $\left(\frac{\pi d}{\lambda} \gg 1\right)$ for large, opaque, spherical particles with independent scattering [104,105] (see Table 3). Though this value, 330 $\mathrm{m^{-1}}$, is an order of magnitude smaller than the mean extinction coefficient measured for fibrous alumina with fiber diameters of 1–9 μm [108] (similar to the length scale of the fibers in the ceria particles), it is reasonable to anticipate the extinction coefficient of a packed bed of ceria fibers to be much lower than that of the individual particles. The scattering albedo equals 1, in agreement with room temperature radiative property measurements on porous ceria structures [109,110].

Results for the volume-averaged temperatures and the fuel production rates changed by less than 3% for scattering albedo in the range of 0.8–1.

The mass flow rate and the composition of the gases are specified as step inputs to simulate the reduction and oxidation half-cycles for the two reactive elements (eqs. (14) and (15)).

$$\dot{m}_{\text{in}}(t) = \begin{cases} \dot{m}_{\text{sg}} = 0.11 \text{ g s}^{-1} & t \in (0, t_{\text{rd}}] \\ \dot{m}_{\text{ox}} = 0.17 \text{ g s}^{-1} & t \in (t_{\text{rd},} t_{ox}] \end{cases} \tag{14}$$

$$X_{\text{O}_2,\text{in}}(t), X_{\text{CO,in}}(t), X_{\text{CO}_2,\text{in}}(t) = \begin{cases} 10^{-5}, 0, 0 & t \in (0, t_{\text{rd}}] \\ X_{\text{O}_2,\text{eq}}, X_{\text{CO,eq}}, X_{\text{CO}_2,\text{eq}} & t \in (t_{\text{rd},} t_{ox}] \end{cases} \tag{15}$$

During oxidation, the inlet gas composition is the equilibrium composition due to thermal dissociation of CO_2 at the oxidizer inlet temperature. The inlet gas temperatures are established by iterating the gas temperatures at the outlet of the 3-D model domain with the heat exchanger model at time intervals of 10 s. The gases are stipulated to leave the reactive elements at atmospheric pressure and all other field variables at the outflow boundaries are extrapolated from the interior solution domain by applying zero normal derivatives at the boundary. The insulating material surrounding the cavity is not modeled explicitly but rather treated as a 3.5 cm thick layer of alumina with temperature dependent thermal conductivity [111] with an overall heat loss coefficient,

$U = 1 \text{ W m}^{-2} \text{ K}^{-1}$, applied to the external surface (see Figure 4.2). This value is determined by trial and error to match the total thermal loss to the measured values, i.e., about 35% of the absorbed power. To reduce the computational time to reach steady-periodic cycling, the initial flow field, temperature and species concentration distribution

are determined from solutions of the steady transport equations for CO_2 and N_2 flowing through the reactive elements. The initial non-stoichiometry of ceria is established by the equilibrium oxidation state (0.0214) due to thermal dissociation of CO_2 at 1773 K.

Reaction Kinetics

To our knowledge, kinetic expressions for CO_2 splitting by ceria at 1773 K are not available in the literature. In the present study we use a modified form of the kinetic expression developed by Bulfin et al. [112] for oxidation of ceria in an oxygen atmosphere at 773–1273 K. To reduce the number of the morphology dependent reaction rate parameters, the prior model is rearranged to express the rate of generation of oxygen vacancies as a function of the oxidation rate constant, k_{ox},

$$\frac{d\delta}{dt} = k_{\mathrm{ox}}\delta\left(\left(\frac{p_{\mathrm{O_2,eq}}}{p_{\mathrm{ref}}}\right)^n - \left(\frac{p_{\mathrm{O_2}}}{p_{\mathrm{ref}}}\right)^n\right), \tag{16}$$

where,

$$k_{\mathrm{ox}} = A_{\mathrm{ox}}\exp\left(-\frac{E_{\mathrm{ox}}}{R_u T}\right), \tag{17}$$

and $p_{\mathrm{O_2,eq}}$ is known from the thermodynamic data [9]. The values of the reaction order, n and the activation energy, E_{ox}, are fixed at 0.22. and 38 kJ mol^{-1} K^{-1} respectively based on the estimates provided by Bulfin et al. [112] and the temperature, T , is fixed at 1773 K. The volumetric, mass source/sink term for O_2 release/uptake from the ceria particles is

$$\dot{r}_{\mathrm{O_2,ceria}} = \frac{M_{\mathrm{O_2}}}{2M_{\mathrm{CeO_2}}}(1-\phi_{\mathrm{eff}})\,\rho_{\mathrm{CeO_2}}k_{\mathrm{ox}}\delta\left(\left(\frac{p_{\mathrm{O_2,eq}}}{p_{\mathrm{ref}}}\right)^n - \left(\frac{p_{\mathrm{O_2}}}{p_{\mathrm{ref}}}\right)^n\right). \tag{18}$$

Prior work indicates direct thermal dissociation of CO_2 is significant at elevated temperatures [15,113]. The reversible rate of the direct thermolysis of CO_2 is modeled with a rate coefficient, $k_{\mathrm{d,CO_2}}$, maintaining the reaction order of *n* with respect to O_2 resulting in the following dissociation rates for the i^{th} species:

$$\dot{r}_{\mathrm{i,diss}} = \frac{\nu_i M_{\mathrm{i}}}{M_{\mathrm{CeO_2}}} (1-\phi_{\mathrm{eff}})\, \rho_{\mathrm{CeO_2}} k_{\mathrm{d,CO_2}} \left(\left(K_{\mathrm{eq,CO_2}}(T) \frac{p_{\mathrm{CO_2}}}{p_{\mathrm{ref}}} \right)^{2n} - \left(\frac{p_{\mathrm{CO}}}{p_{\mathrm{ref}}} \right)^{2n} \left(\frac{p_{\mathrm{O_2}}}{p_{\mathrm{ref}}} \right)^{n} \right), \tag{19}$$

where ν_i is ½, 1 and -1 for O_2, CO and CO_2 respectively. The net rate of oxygen release due to the dissociation reaction and the reoxidiation of ceria is,

$$\dot{r}_{\mathrm{O_2,net}} = \dot{r}_{\mathrm{O_2,diss}} + \dot{r}_{\mathrm{O_2,ceria}}\,. \tag{20}$$

Because the thermolysis products are anticipated to recombine without a rapid quench, we assume complete recombination. In this case, the resulting molar flow rate of CO at the packed bed outlet is expressed as,

$$\dot{n}_{\mathrm{CO,out}} = \dot{n}_{\mathrm{CO,diss}} - 2\dot{n}_{\mathrm{O_2,net}} \tag{21}$$

The morphology dependent rate coefficients, A_{ox} and $k_{\mathrm{d,CO_2}}$ are determined by modeling the experimental bench top reactor used by Venstrom et al. [15] to obtain global reaction rates of reduction and oxidation of a packed bed of ceria particles at 1773 K. The reaction rate coefficients that yield the best fit of the model predictions with the experimentally measured rates of O_2 and CO production are determined via optimization. The minimization function to determine k_{ox} and $k_{\mathrm{d,CO_2}}$ is a vector sum

(over all gas flow rates) of the root mean square error values normalized by the inlet flow rate,

$$RMSE_{\mathrm{f,\{sg/ox\}}} = \frac{\sqrt{\frac{\sum_{i=1}^{i=N_t}\left(\dot{n}_{\{O_2/CO\},i}^{\mathrm{mod}} - \dot{n}_{\{O_2/CO\},i}^{\mathrm{exp}}\right)^2}{N_t - 1}}}{\dot{n}_{in}}. \quad (22)$$

The range considered for parameter estimation of A_{ox} is 0.01–100 and 0.01–10 for $k_{\mathrm{d,CO_2}}$ with a resolution/accuracy of 0.5 and 0.1 respectively. The selected upper bounds results in species mole fraction and ceria nonstoichiometry within 1% of the thermodynamic equilibrium values at all the gas flow rates considered.

The bench top reactor is a 9.5 mm diameter alumina tube containing ~1 g of 3-5 mm sized, ~65% porous ceria particles heated in a tubular IR imaging furnace [15]. The governing transport equations described in section 3.1 (eq. (4), (6)) for the solar reactor are applied to the isothermal bench top reactor. The model simulates 1000 s of reduction and about 300 s of oxidation for sweep gas and oxidizer molar flow rates of 0.67 $\times 10^{-4}$ to 4 $\times 10^{-4}$ mol s^{-1} g_{ceria}^{-1}. Prior to reduction, the nonstoichiometry for the ceria bed is initialized to the equilibrium value of 0.0214 due to the thermolysis of 100% CO_2 at 1773 K. For the oxidation step ceria nonstoichiometry is initialized based on the experimentally measured CO production rate.

The values for the reaction rate coefficients determined from the model of the bench-top reactor are used in the 3-D reactor model to determine the volumetric mass sinks/sources (eqs. (18)–(20)) and applied in the transport equations (4) and (6). The rate constants evaluated at 1773 K are deemed acceptable because k_{ox} changes by less than 15% over the largest range of temperatures predicted in the reactor.

Solution Procedure

The transport equations are solved using the finite volume method on an unstructured, hexagonal dominant mesh with approximately 600,000 cells for the 3-D reactor model. Mapped or structured cells are used wherever possible and a higher density of cells is present within the reactive elements than in the reactor cavity. Every octant space is discretized into 5×5 control or solid angles and the angles that are not aligned with the mesh boundaries are further pixelated into 3×3 solid angles. Doubling the resolution of the angular discretization on the same spatial mesh increases false scattering, as observed by Martinek et al. [101], and resulted in less than 3% change to the spatially averaged temperature and ceria non-stoichiometry. Increasing the spatial refinement of the mesh to 900,000 cells altered the volume averaged temperature and non-stoichiometry by less than 1%. A first-order Euler implicit scheme is used for time integration with a time step of 1 s. The SIMPLE algorithm is used to couple the pressure and the velocity fields, with second order upwinding for the advection terms in the momentum, energy transport and the radiative transfer equations. The rate of change of ceria nonstoichiometry is implemented as a user-defined scalar transport equation [62] without the advection and diffusion terms. The source terms for mass, momentum, and energy have been linearized appropriately to enforce the positivity criterion [61]. The governing equations are solved with the globally scaled residual values for convergence set as 10^{-8} for continuity, momentum, and species transport equations and 10^{-10} for the energy, intensity and the scalar transport equation. To enable high performance computing, the 3-D reactor mesh is partitioned over eight nodes.

Results

Reaction Kinetics

Figure 4.3 and Figure 4.4 compare the measured rates of O_2 and CO production at 1773 K to those predicted by the model. The best fit kinetics parameters are $A_{\mathrm{ox}} = 1.5$ $\mathrm{mol_O\ mol_{ceria}^{-1}\ s^{-1}}$, which yields k_{ox}= 0.11 $\mathrm{mol_O\ mol_{ceria}^{-1}\ s^{-1}}$, and $k_{\mathrm{d,CO_2}} = 0.3$ $\mathrm{mol_{CO}\ mol_{ceria}^{-1}\ s^{-1}}$. The vector sum of the normalized root mean square error for the gas flow rates simulated is less than 1.5×10^{-3} for the identified rate coefficients. The predicted O_2 production is insensitive to an increase in A_{ox} except for the highest N_2 flow rate considered. This result implies that gas phase mass transport limits reduction rates for slower sweep gas flow rates. The rate of oxidation is impacted by both mass transport and surface kinetics.

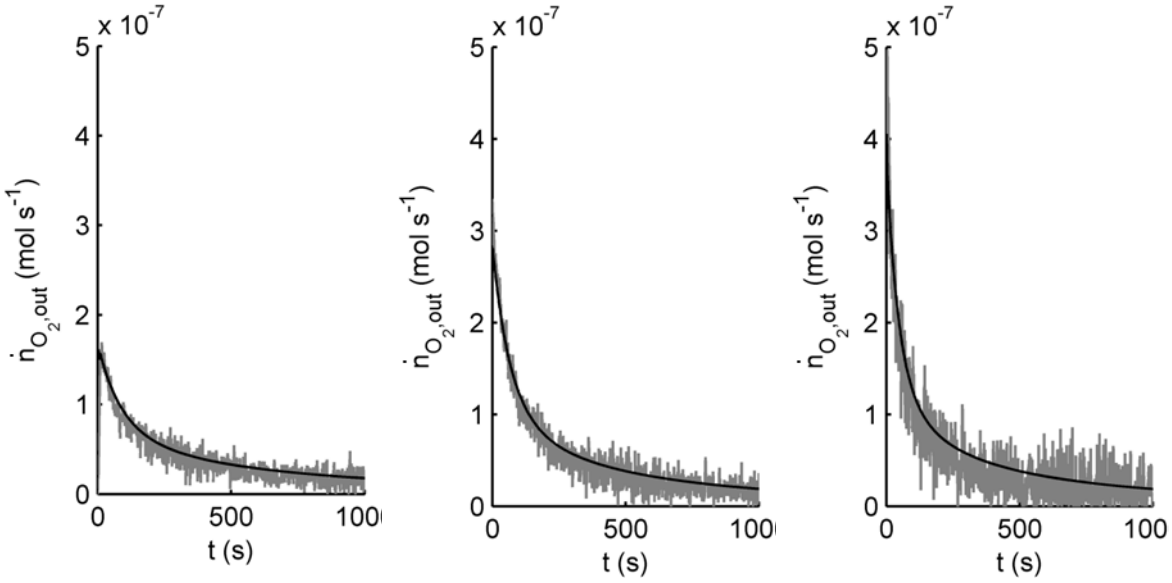

(a) (b) (c)

Figure 4.3 Comparison of measured (grey line) and predicted (black line) rates of O_2 release at 1773 K for N_2 sweep gas (10 ppm O_2) flow rates of (a) 1×10^{-4}, (b) $2\times10^{-4}$and (c) 4×10^{-4} mol s^{-1} g_{ceria}^{-1}.

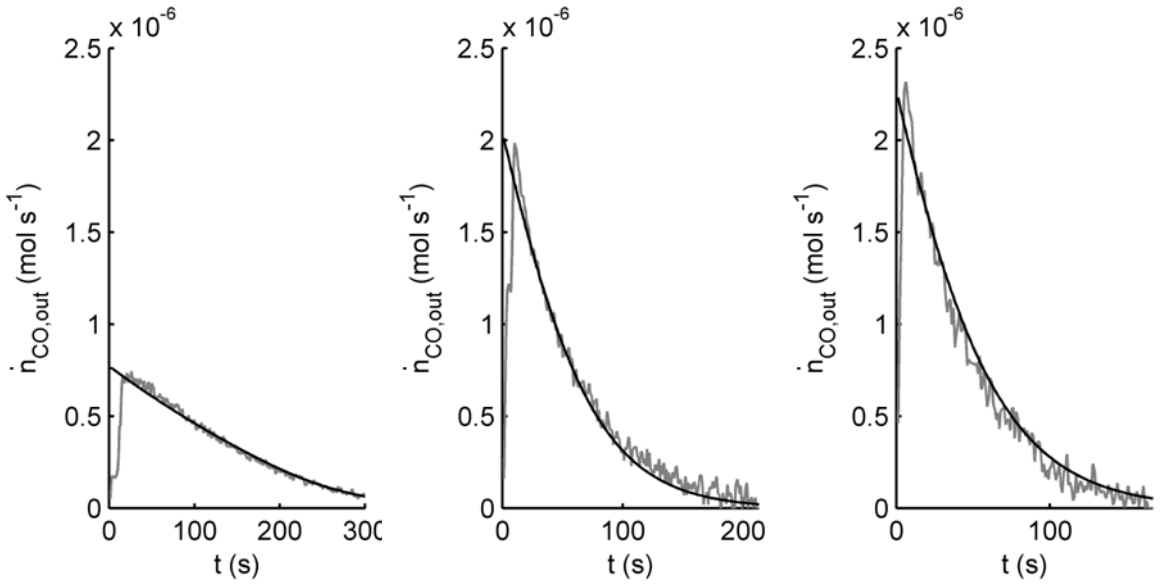

(a) (b) (c)

Figure 4.4 Comparison of measured (grey line) and predicted (black line) rates of CO release at 1773 K with 100% CO_2 flow rates of (a) 0.67×10^{-4}, (b) 3×10^{-4} and (c) 4×10^{-4} mol s^{-1} g_{ceria}^{-1}

Reactor Performance

The transient behavior during steady periodic cycling is presented with an emphasis on transport and chemical processes within the reactive elements. Figure 4.5 shows the distribution of absorbed solar flux on the surfaces of the cavity and six reactive elements based on application of rotational symmetry on the 60° angular sector depicted in Figure 4.2. The overall absorption efficiency, defined as,

$$\eta_{abs} = \frac{\dot{Q}_{\text{solar,abs}}}{Q_{\text{solar}}}, \tag{23}$$

is 99.8%. The reactive elements effectively intercept the incident light and obstruct the direct view of the cylindrical cavity walls by the aperture resulting in 51% absorption of the incident power on the reactive elements and 47% absorption on the cavity surfaces, equally split along the circumference and the back plane. The average flux on a reactive element is 4700 W m^{-2}. The regions of higher flux, 1300–5×10^4 W m^{-2}, are where the tubes are directly illuminated. On the cavity surface, the fluxes vary from 325 to 7880 W m^{-2}. On the back plane of the cavity, the flux distribution is $2\times10^4 \pm 1\times10^4$ W m^{-2}. The localized regions of high flux are consistent with the conical spread of the incident light and the geometric intersection of light with the cavity and reactor tube surfaces

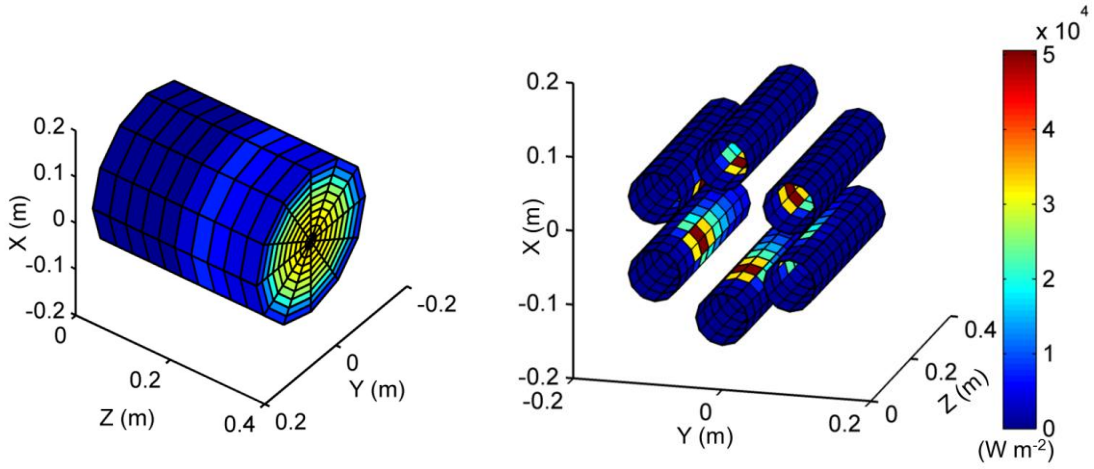

(a) (b)

Figure 4.5 Spatial contours of the absorbed incident solar fluxes for a diffusely incident input solar power of 4.2 kW with a half-cone angle of 37.7° on the surfaces of the (a) cavity and (b) reactive elements.

Spatial Temperature Profiles

Temperature distributions in the cavity and the integrated reactive element/heat exchanger are provided at one instant (Figure 4.6); spatial trends are similar throughout the cycle. The temperature distribution in the cavity including the outer surface of the reactive elements is shown in at the end of reduction/oxidation in RE1/RE2. The area-averaged surface temperature of the cylindrical surface of the cavity is 1786 K. The back plane of the cavity is 1800 K where the absorption of the incident flux is higher (see Figure 4.6 (a)). About half of the input solar power is transferred to the reactive elements by surface-to-surface radiative exchange resulting in average temperatures of 1797 and 1795 K for the reactive elements at the end of reduction and oxidation respectively. Maximum surface temperatures in the reactive elements are at locations of the peak absorbed flux (see Figure 4.5 (b) and Figure 4.6 (b)).

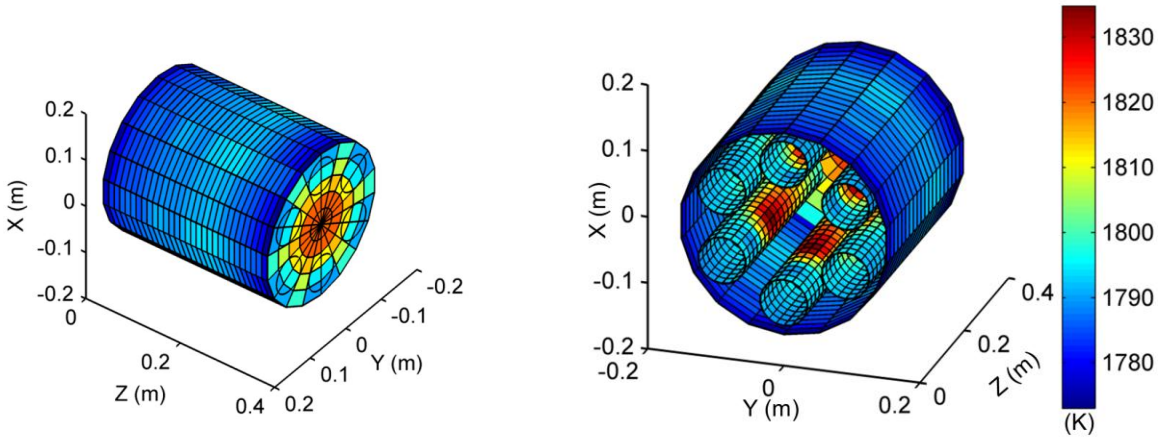

(a) (b)

Figure 4.6 Spatial contours of the surface temperatures for an input solar power of 4.2 kW with a half-cone angle of 37.7° for (a) the cavity and (b) the reactive elements.

Figure 4.7 illustrates the axial temperature profile in the integrated reactive element/heat exchanger at the end of reduction in RE1 (4.7a), and the 3-D temperature distributions in the annulus (4.7b) and the center channel (4.7c) at the end of reduction and oxidation in RE1 and RE2 respectively. Figure 4.7 (a) also compares predicted and measured axial temperatures along the outer surface of the integrated reactive element/heat exchanger. There is excellent agreement along the heat exchanger. Measured data within the cavity are within 10 to 30 K of the predicted temperature. This difference is relatively small compared to the absolute temperature in the cavity. Potential causes for the difference include nonuniform flux at the aperture in the solar simulator, uncertainty in the assumed value for surface optical properties, and measurement uncertainty ($\pm$9 K). As shown in the plot, the N_2 sweep gas entering the reactor is preheated from ambient to 1787 K at the inlet of the particle bed (z = 0 m). The product gas leaves the ceria bed at 1760 K, and exits the heat exchanger at 400 K. The average difference in the bulk gas temperature in the annulus and the centre channel is less than 100 K due to enhanced flow mixing in the porous media and effective radiative transport.

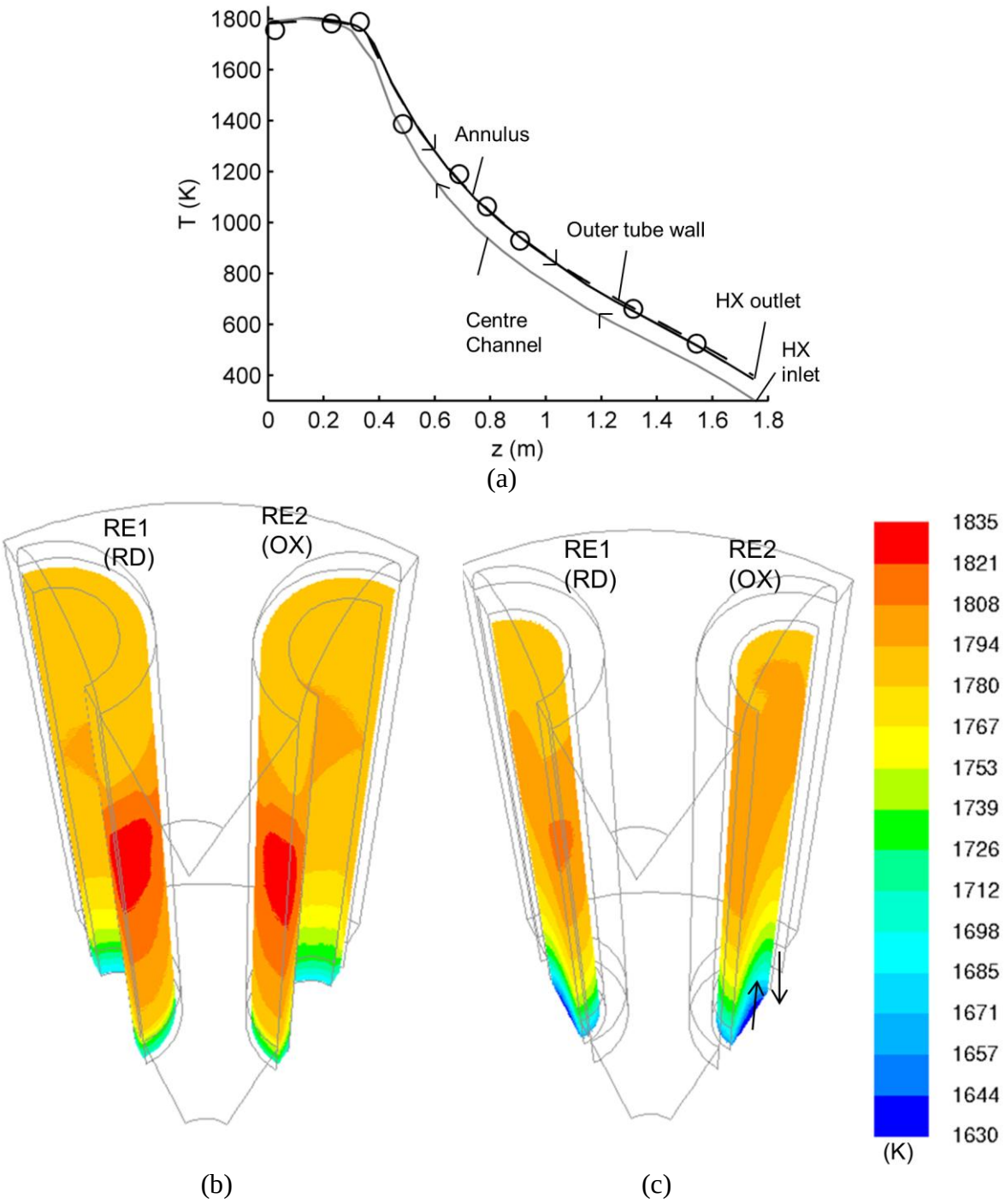

Figure 4.7 Axial distribution of the (a) bulk mean gas temperature (solid lines) and comparison of predicted (dashed line) and measured (open circles) temperatures along the outer surface of the integrated reactive element (RE1)/heat exchanger; 3-D contours of predicted temperatures in RE1 and RE2 in the (b) annulus and (c) centre channel. Mass specific sweep gas and oxidizer flow rates are 0.67 mol s^{-1} g_{ceria}^{-1}. Arrows indicate flow direction.

Based on the axial temperature distribution, the steady periodic heat recovery effectiveness,

$$\varepsilon_{\{\mathrm{sg,ox}\}} = \frac{\bar{h}_{\{\mathrm{sg,ox}\}}\left(T_{\mathrm{c,out}}\right) - \bar{h}_{\{\mathrm{sg,ox}\}}(T_{\mathrm{amb}})}{\bar{h}_{\{\mathrm{sg,ox}\}}\left(T_{\mathrm{h,in}}\right) - \bar{h}_{\{\mathrm{sg,ox}\}}(T_{\mathrm{amb}})}, \tag{24}$$

is 91 to 93% in a cycle. The predicted pressure drop across the integrated reactive element/heat exchanger is 10 kPa during reduction and 15 kPa during oxidation. The pressure drop across the ceria bed results in a 5% drop in the fuel production rate as compared to the reduction and oxidation of ceria at atmospheric pressure. The benefit of heat recovery outweighs this slight decrease in fuel production.

Figure 4.7 (b) and Figure 4.7 (c) reveal that the largest temperature variations are in the stream wise direction, as expected for large axial Peclet numbers ($Pe_{ax} > 4000$). Highly effective radiation from the tube surfaces and within the ceria bed maintains greater spatial uniformity radially and circumferentially. The predicted temperatures and intensity distributions (not shown in the figure) are analyzed to compare the relative contributions of the heat transfer modes in the ceria packed bed. Radiative heat flux vectors are evaluated as in eq. (12) and the convective heat flux vector in the k^{th} direction is obtained by integrating $\nabla_k \cdot \left(\rho_f \boldsymbol{u_k} \sum_i Y_i h_{if}\right)$. Heat transfer in the radial direction is dominated by radiation (~95%), whereas heat transfer in the axial direction is dominated by convection (85%). Solid phase conduction contributes negligibly (< 1%) to heat transfer due to the low bulk thermal conductivity of ceria ($\bar{k}_{\mathrm{s,eff}} = 0.12$ W m^{-1} K^{-1} at 1773 K). Additional plots are provided at the end of this chapter to depict the relative uniformity of temperature in the radial and circumferential directions as compared to the axial direction.

Transient Phenomena

The volume-averaged temperatures and fuel production are shown for two redox cycles (Figure 4.8). The reactive elements behave identically except they are out of phase by the half-cycle time of 100 s. The peak CO production, 2×10^{-4} mol s^{-1}, is at the onset of oxidation (Figure 4.8 (a)) when the ceria is the most reduced and decays to 0.6×10^{-4} mol s^{-1} after 100 s. In the first 25 s of oxidation, the average bed temperature increases from 1791 K by approximately 1 K due to the exothermic reoxidation of ceria and decreases thereafter as the rate of CO production decreases (Figure 4.8 (b)). At the start of reduction, oxygen is released at 0.7×10^{-4} mol s^{-1} and the rate decays as the nonstoichiometry (volume-averaged) of the ceria increases from 0.026 to 0.030. During reduction, the ceria temperature decreases initially, from 1791 to 1790 K, due to the endothermic reduction of ceria. Overall, during steady cycling nearly isothermal conditions are maintained at ~1791 K with time-averaged temperature variations less than 1 K between reduction and oxidation. The cycle-averaged CO production is 3.6×10^{-4} mol s^{-1}. The mass specific, cycle-averaged CO production is 0.1 μ mol s^{-1} g_{ceria}^{-1}. For comparison, during testing the prototype reactor produced 0.09 μ mol_{CO} s^{-1} g_{ceria}^{-1} with slightly lower gas flow rates.

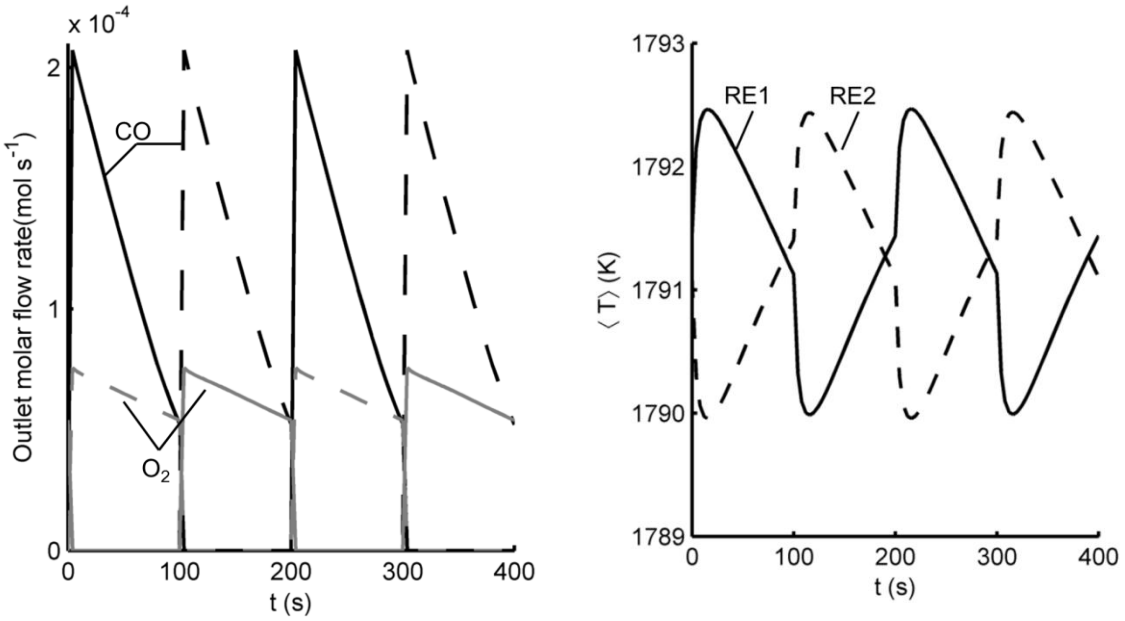

(a) (b)

Figure 4.8 Transient (a) outlet molar production of CO and O_2 with sweep gas and oxidizer flow rates of 0.67×10^{-4} mol s^{-1} g_{ceria}^{-1} and (b) volume-averaged ceria temperatures in RE1 (solid lines) and RE2 (dashed lines). Oxidation occurs from 1–100 s and 101–200 s, and reduction occurs from 101–200 s and 1–100 s in RE1 and RE2 respectively.

Simulations were also performed assuming more reflective surfaces in the cavity. In modeling the incident radiation, emissivities of the alumina insulation and alumina tubes were fixed at 0.3 and 0.4, consistent with data for total normal emittance at 700–1500 K for the porous alumina insulation and spectral emittance at 0.64 μm for the dense alumina tubes [114]. Absorption increases from 350 W to 460 W on the tube surfaces. As a result, the volume averaged temperature of ceria increases from 1791 to 1798 K during reduction and from 1792 to 1799 K during oxidation. The CO production rate increases by 12% to 4×10^{-4} mol s^{-1}. The higher temperature during isothermal operation improves chemical performance by increasing the extent of reduction.

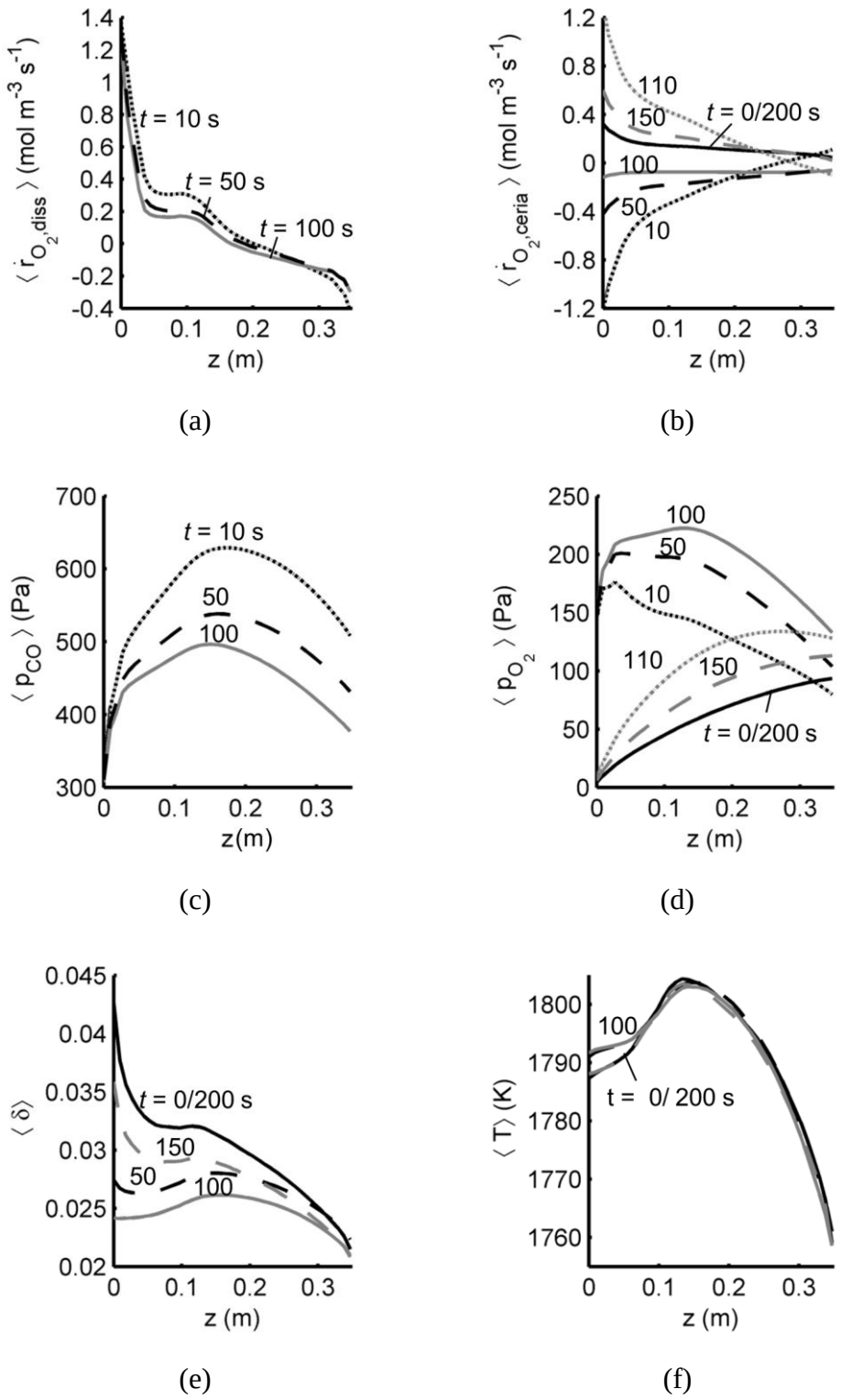

Figure 4.9 Axial and transient variations in the area-averaged (a) rate of oxygen produced due to CO_2 dissociation (b) rate of oxygen produced by ceria (c) CO partial pressure (d) oxygen partial pressure, (e) nonstoichiometry and (f) temperature with 0.67 mol s^{-1} g_{ceria}^{-1} of N_2 and CO_2.

Figure 4.9 depicts the time evolution of the area-averaged rates, partial pressure of O_2 and CO, temperature and the oxidation state of ceria in the streamwise direction for RE1 over one cycle. The data for RE2 follow the same trends. These data illustrate the interrelated transport processes and their effects on reaction rates. At $t = 1$ s, the flow of CO_2 is initiated. The gas flow is switched to N_2 at $t = 101\ s$. First consider oxidation. Figure 9(a) shows the highest rate of dissociation of CO_2 is at the inlet of the bed; the peak dissociation rate is 1.4 mol m^{-3} s^{-1} at t = 10 s. Dissociation slows in the streamwise direction due to the accumulation of thermolysis products. Likewise, the ceria uptake of O_2 decreases along the flow direction (Figure 4.9 (b)). This decrease in the oxidation state of ceria combined with the decrease in the bed temperature (Figure 4.9 (f)) leads to the recombination of dissociation products (indicated by negative values of $\dot{r}_{O_2,\mathrm{diss}}$) and a decrease in the CO partial pressure (Figure 4.9 (c)). For t < 30 s, ceria uptakes oxygen (Figure 4.9 (b)), nearly as fast as CO_2 dissociates. For t > 30 s, the rate of oxygen uptake is slower than dissociation. At the inlet, the rate of oxygen uptake drops from 1.2 mol m^{-3} s^{-1} at t = 10 s to 0.43 mol m^{-3} s^{-1} at t = 50 s, whereas the dissociation rate decreases by only 10% to 1.3 mol m^{-3} s^{-1} over the same duration. Corresponding to the decrease in the rate of uptake of O_2, the nonstoichiometry decreases from 0.028 to 0.025. The transient profiles during reduction are tied closely to the state of the bed at the end of oxidation. As the ceria is reduced, the O_2 partial pressure increases in the axial direction (Figure 4.9 (d)). This increase reduces the driving force for the chemical reaction and O_2 production slows (Figure 4.9 (b)). At t =110 s, a small region near the exit of the bed (z > 0.25 m) is reoxidized due to the higher oxygen partial pressure and lower bed temperature. The O_2 release slows over the course of the half cycle with the fastest decrease where ceria is the

most reduced. The largest swings in ceria nonstoichiometry are at the inlet (Figure 4.9 (e)), where the fastest reaction rates are observed (Figure 4.9 (a,b)).

Temperature variations (see Figure 4.9 (f)) during cycling are influenced primarily by the differences in convective heat transfer rates. The only location where the energy release/consumption by the chemical reactions accounts for the difference in temperature between oxidation and reduction is within 80 mm of the inlet. Here the temperature during oxidation is as much as 5 K higher than during reduction. The rest of the bed experiences a 1–2 K thermodynamically favorable temperature swing due to the higher thermal capacitance of the flow of CO_2 compared to N_2.

The results of the model and interpretation of the bench top data lead us to the conclusion that fuel production is limited by the thermodynamic capacity of the flowing gas to change the oxidation state of the ceria. To support this conclusion, we show the model predictions for ceria nonstoichiometry approaches the thermodynamic equilibrium state of ceria corresponding to the local oxygen partial pressure and temperature (Figure 4.10). The maximum deviation in nonstoichiometry is 15% during reduction and 6% during oxidation. The implications of this result are surface kinetics is rapid relative to gas phase mass transport and the fixed bed flow configuration provides highly effective utilization of the sweep gas and the oxidizer for the chosen material morphology, gas flow rates and the cycle times.

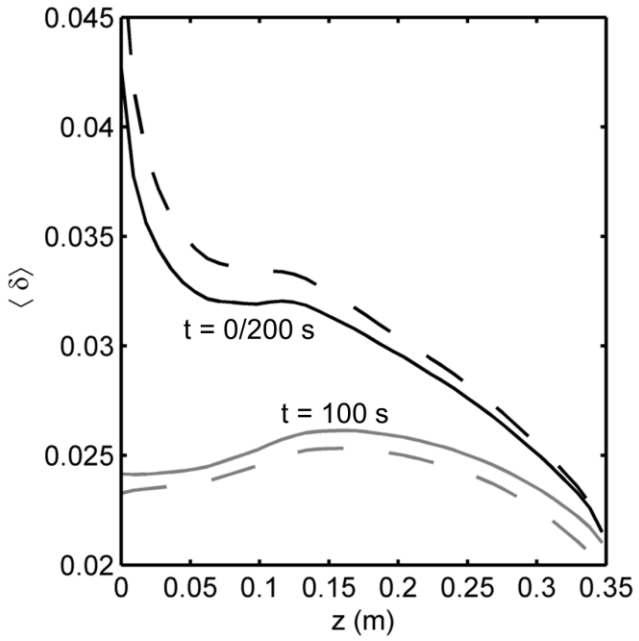

Figure 4.10 Comparison of model predictions (solid lines) of area-averaged ceria bed nonstoichiometry and the equilibrium values (dashed lines) at the end of oxidation and reduction with 0.67 mol s^{-1} g_{ceria}^{-1} of sweep gas and CO_2.

Reactor Efficiency

To discuss the energetic impacts of the selected operating conditions, the overall energy balance of the solar reactor prototype during steady periodic operation is considered during steady periodic operation:

$$\dot{Q}_{\text{solar}} = \underbrace{\sum_{i,\text{out}} I_{\text{ap},i} \left| \boldsymbol{s}_i \cdot \hat{k} \right|}_{\dot{Q}_{\text{rerad}}} - \underbrace{\iint (k_{\text{ins}} \cdot \nabla_r T) \cdot dA_{\text{ins}}}_{\dot{Q}_{\text{loss}}}$$

$$+ \underbrace{\left(\frac{1}{2}\right) \dot{n}_{\text{sg}} \left[\bar{h}_{\text{sg}}(T_{\text{RE,out}}) - \bar{h}_{\text{sg}}(T_{\text{RE,in}}) \right]}_{\dot{Q}_{\text{sg}}} + \underbrace{\left(\frac{1}{2}\right) \dot{n}_{\text{ox}} \left[\bar{h}_{\text{ox}}(T_{\text{RE,out}}) - \bar{h}_{\text{ox}}(T_{\text{RE,in}}) \right]}_{\dot{Q}_{\text{ox}}}$$

$$+ \iiint \underbrace{\frac{\int_t \left(\dot{S}_{\text{rxn,rd}} + \dot{S}_{\text{rxn,ox}} \right) dt}{t_{\text{cycle}}} dV}_{\dot{Q}_{\text{chem}}} \tag{25}$$

At steady state, the input solar power, $\dot{Q}_{\mathrm{solar}}$ on the left hand side is equal to the sum of the heat loss due to reflection and thermal emission, $\dot{Q}_{\mathrm{rerad}}$, the thermal loss to the ambient via natural convection from the aperture and conduction through the insulation, $\dot{Q}_{\mathrm{loss}}$, the sensible energy requiredforthe sweep gas and oxidizer gas, $\dot{Q}_{\mathrm{sg}}$ and $\dot{Q}_{\mathrm{ox}}$, and the energy requirements of the net reaction, $\dot{Q}_{\mathrm{chem}}$. The reradiation loss, $\dot{Q}_{\mathrm{rerad}}$, is calculated from the angular profiles of the outgoing intensity (I_{ap}) distributions at the aperture and equals 880 W. The conduction losses are obtained from a surface integral of the heat fluxes on the outer surface of the insulation and equals 1210 W. The gas phase sensible heating load is 2 kW, 660 W for reduction ($\dot{Q}_{\mathrm{sg}}$) and 1.34 kW for oxidation ($\dot{Q}_{\mathrm{ox}}$). Despite remarkably high heat recovery effectiveness, the sensible heating load approaches 50% of the input power. The chemical energy requirement is computed by time averaging the volume integrals of the energy sources/sinks (eq. (8)) over a cycle and equals 108 W. The magnitude of $\dot{Q}_{\mathrm{chem}}$ is much smaller in comparison to the other energy terms due to the small swings in ceria nonstoichiometry (~0.004) during isothermal cycling.

We define the overall solar-to-fuel efficiency of the reactor as,

$$\eta = \frac{\bar{\dot{n}}_{\mathrm{f}} \cdot \mathrm{HHV}_{\mathrm{f}}}{\dot{Q}_{\mathrm{solar}} + \dfrac{\dot{W}_{\mathrm{sg,sep}} + \dot{W}_{\mathrm{ox,sep}} + \dot{W}_{\mathrm{ox,pump}}}{\eta_{\mathrm{s\to E}}}} \tag{26}$$

where the numerator is the rate at which chemical energy is stored in the fuel. The denominator includes the concentrated solar power plus the solar thermal equivalents of the parasitic work requirements for separation of the sweep gas N_2 from air, separation of the oxidation products, and pumping. The work terms are assumed to be provided by

solar energy with a solar to electric energy conversion efficiency ($\eta_{s\to E}$) of 25%. The energy required for N_2 production in the desired purity (1–10 ppm O_2), $\dot{W}_{sg,sep}$, is 12.1 kJ mol-N_2^{-1} for a cryogenic air separation plant, which delivers the gas at an elevated pressure of 8 bars [85]. The theoretical minimum work with an efficiency factor of 10% is used to calculate the energy costs to separate pure CO from the product stream, $\dot{W}_{ox,sep}$. The power required to pump the oxidizer, $W_{ox,pump}$, through the integrated reactive element/heat exchanger is evaluated assuming an 80% efficient compressor. At mass specific flow rates of 0.67×10^{-4} mol s^{-1} g_{ceria}^{-1}, 5.7 kW is needed to produce pure N_2. The energetic cost to produce N_2 is comparable to the input solar power and is the largest of the parasitic energy terms. Smaller contributions to the parasitic energy are pumping the oxidizer (210 W) across a pressure drop of 15 kPa and CO separation (240 W) in the product stream. Solar-to-fuel conversion efficiency is 0.9% for this process.

Conclusion

Results of a transient three-dimensional model of a 4 kW_{th} solar thermochemical reactor for splitting carbon dioxide via the isothermal ceria redox cycle at 1773 K provide insight to the interactions between transport processes and chemical kinetics and how these interactions impact temperature, pressure, species concentrations, and fuel production. The modeled reactor has two major benefits compared to the prior art. First, it produces fuel continuously on-sun by alternating the reduction and oxidation reactions between six independent reactive elements in 100 s half-cycles. Redox cycling is accomplished by switching the inlet gas between a nitrogen sweep gas for reduction and carbon dioxide for oxidation. As a consequence, the reactor has no high temperature moving parts. Second, heat recovery of the sensible heat of the gases is integral to the

reactor. Each reactive element is a concentric assembly of two alumina tubes. Gases flow into the reactive element through the inner channel and out of the reactor through the annulus. Within the solar cavity, the annulus is filled with porous ceria particles that provide rapid diffusion of oxygen, low pressure drop, and effective heat transport. Outside the solar cavity the tubes are filled with alumina reticulated porous ceramic (RPC) to provide highly effective heat recuperation.

Two challenges in modeling the reactor are the limitation of the available kinetic models for the redox chemistry, particularly for oxidation, and the lack of data for optical surface properties in the solar spectrum at the temperatures of interest. To address the first challenge, we developed reversible reaction rate expressions for the dissociation of CO_2 molecules in addition to the reduction/oxidation reactions in ceria. The rate expression provided by Buffin et al. [112] for oxidation of ceria in an oxygen atmosphere at 773–1273 K was rearranged for simplicity. The necessary reaction rate coefficients were extracted from published global rates obtained in a bench top isothermal reactor at 1773 K [15]. With reference to equations (16) and (19), the kinetic parameters are $A_{\mathrm{ox}} = 1.5$ $\mathrm{mol_O\ mol_{ceria}^{-1}\ s^{-1}}$ and $k_{\mathrm{d,CO_2}} = 0.3$ $\mathrm{mol_{CO}\ mol_{ceria}^{-1}\ s^{-1}}$. To address the second challenge, we explored the relative differences in the reactor performance for reflective versus absorptive cavity surfaces. Higher absorption on the reactor tube surfaces for a reflective cavity increased the volume-averaged ceria temperature, from 1791 to 1799 K yielding a 12% boost in fuel production rate.

The results illustrate the effectiveness of the reactor to carry out the isothermal redox cycle and at the same time expose the thermodynamic limitations of the isothermal approach. Radiative transport is highly effective at achieving high absorption efficiency

and isothermal conditions at the nominal operating temperature of 1773 K. More than half of the incident solar power is absorbed by the surfaces of the reactive elements in which the redox chemistry takes place. The spatially averaged surface temperatures of the reactive elements are closely coupled —1795 K during reduction and 1797 K during oxidation. The volume and time averaged temperature of the indirectly irradiated ceria particles is 1791 K during reduction and 1792 K during oxidation; except for a small region of the ceria bed close to the inlet, a slightly favorable thermodynamically favorable temperature swing is achieved due to the relative differences in the convective cooling capacity of the gases. Even with demonstrated heat recovery effectiveness greater than 90%, increasing the flow rate of the oxidizer further to improve the fuel production rate and the temperature swing is not beneficial due to the additional power required to heat the unreacted CO_2. Moreover, reducing the flow rate of sweep gas, to promote a favorable temperature swing and reduce the energy penalty for N_2 production, will adversely impact the rate of oxygen release from the ceria.

For the design operating conditions, fuel is produced continuously at 3.6×10^{-4} mol s^{-1} with an energetic power of 100 W based on the higher heating value of CO. Spatial and temporal reaction rates and species concentration profiles reveal that the oxygen release/uptake by ceria is strongly influenced by the streamwise rate of advection of the reactants and products. The reaction rates are limited by the thermodynamic capacity of the gas to carry away/deliver products/reactants. Efficient gas utilization and exemplary (91–93% during cycling) gas phase heat recovery effectiveness are noteworthy milestones, especially due to their dramatic impacts on the overall process efficiencies for isothermal ceria cycles.

Supplementary Information

Figure 4.11 shows the cyclic variations of ceria temperature in the radial and circumferential directions in RE1 at three axial planes — z = 0.04, 0.13 and 0.3 m. These plots are provided to supplement the text in Chapter 4 as evidence of the relative uniformity of temperature and nonstoichiometry in the radial and circumferential directions as compared to the axial direction. The radial and circumferential temperature variations are restricted to less than 15 and 30 K everywhere in the bed during steady cycling. The least temperature differences (< 2 K) in the circumferential and radial directions are observed for $0 \leq z < 0.1$ m. Corresponding to the higher nonuniformities of the wall fluxes at $z = 0.13$ m, this axial plane has the largest circumferential temperature variation of 30 K.

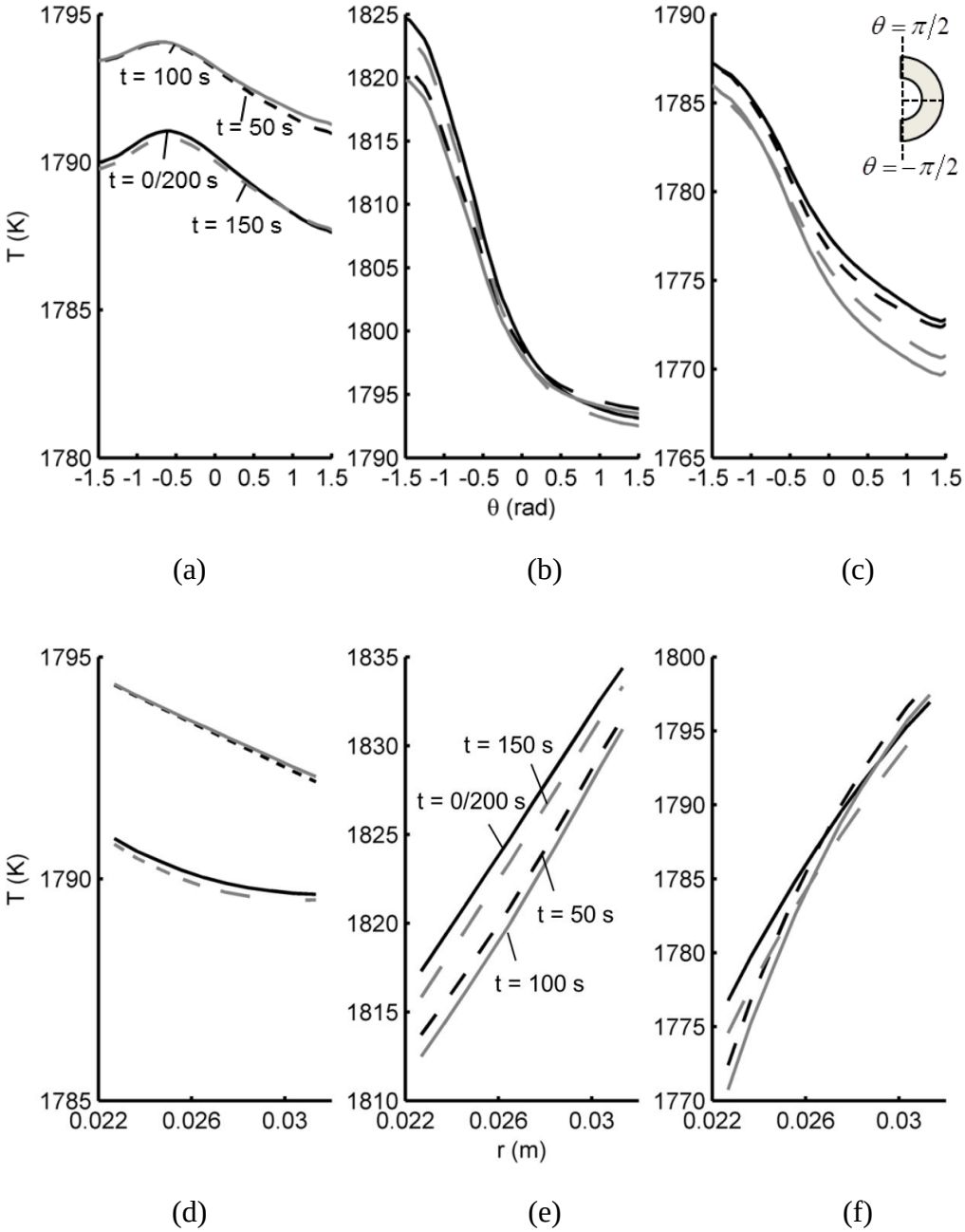

Figure 4.11 Cyclic variations in ceria bed temperature in RE1 in the circumferential direction (a)–(c) at r = 0.026 m and the radial direction (d)–(f) at θ = -1.5 rad at axial locations z = 0.04 m (a,d), z = 0.13 m (b,e) and z = 0.3 m (c,f).

Chapter 5
Summary and Conclusion

Solar energy can be efficiently harnessed and concentrated to split water and/or carbon dioxide to produce H_2 and/or CO, using two-step metal oxide redox cycles, providing a promising pathway to convert abundantly available sunlight into storable and transportable chemical energy forms. To this end, a solar thermochemical reactor to implement a pressure swing, isothermal ceria redox cycle at nominally 1773 K has been developed at the University of Minnesota. The reactor is the first design to produce fuel continuously and implement gas phase heat recovery.

The computational models developed in this dissertation supported the design and characterization of a 4 kW_{th} reactor prototype and the integrated gas phase heat exchanger. The models capture the inherent transients and three-dimensionality of multi-mode transport processes coupled with the heterogeneous chemical reactions in the redox material.

Design and Performance Evaluation of the Heat Exchanger

A steady-state, axisymmetric, conjugate heat transfer numerical model was developed to optimize the alumina RPC morphology and select the size of the counterflow tube-in-tube heat exchangers that were integrated in the reactor prototype. The study in Chapter 2 presented results for 10–30 PPI and 65–90% porosities for the alumina RPC. Larger pore sizes, such as a 5 PPI RPC (pore diameter of 5 mm), were considered only in the centre channel as the continuum approximation may be not be applicable in the annulus that is only 9.1 mm thick. Compared to the existing literature on RPC/foam filled heat exchangers, a distinguishing aspect of the model is the inclusion of

radiative transport in participating media with a numerical scheme (spherical harmonics with the P_1 approximation) that is less restrictive than the "diffusion approximation" and is suitable for the optical thicknesses ($1<\zeta<15$) considered. The P_1 method facilitates consideration of ceramic RPCs, which are typically more scattering than absorbing, i.e. $\omega > 0.5$. An important contribution is the quantification of the relative significance of radiative and conductive transport in the heat exchanger. For any porosity, the larger pores (low PPI) enhance radiative transport and decrease the pressure drop due to decreased inertial and viscous drag forces. Solid phase conduction dominates the overall heat transfer at temperatures below 1000 K and for this reason the lowest porosity considered yields the highest overall heat transfer coefficient (170 W m^{-2} K^{-1} for a 10 PPI RPC with 65% porosity) with the penalty of increased pressure drop. The CFD model of the heat exchanger was coupled to an overall reactor energy balance to consider the tradeoffs between high effectiveness of heat recovery and increased pressure drop on the solar-to-fuel efficiency. A concentric tube assembly filled with 10 and 5 PPI, 85% porous alumina RPC (specific surface areas of 1590 and 790 m^2 m^{-3}) in the annulus and the centre channel was selected with predicted heat recovery effectiveness exceeding 90%.

The actual performance of the heat exchanger during steady operation was determined by applying measured surface temperatures along the length of the integrated reactive element/heat exchanger as boundary conditions to a transient model of the heat exchanger. Model predictions for pressure drop (6.5 and 8.5 kPa during reduction and oxidation) and the gas outlet temperatures (410 K and 395 K) match well with the experimental measurements. The heat exchanger recovered 90–93% of the sensible heat of the sweep and oxidizer gases for gas flow rates of 0.67×10^{-4} mol s^{-1} g_{ceria}^{-1}.

Transport and Chemical Kinetics in the Reactor

To simulate the coupling between fluid flow, heat and mass transfer, radiative transport and chemical reactions, and explore their effects on overall reactor performance, a 3-D, transient, CFD model of the reactor was developed. The model was implemented using Ansys Fluent with modular functions developed to implement the collision based Monte Carlo ray tracing of the incident light in the cavity and the nonstoichiometric redox reactions in ceria. The method of Discrete Ordinates was applied to solve radiative transport in the emission spectrum for the reactor surfaces and the participating media, providing increased flexibility to material morphologies that could be simulated compared to the diffusion approximation that only applies for optically thick media. Applying the Discrete Ordinates or the finite volume method also provides the advantage of simulating the surface-surface radiative heat exchange in the cavity on the same spatial mesh as the CFD model. Surface kinetics for the high temperature oxidation reactions in ceria is not available in literature. An important outcome of this model has been the development of a reaction rate expression and the extraction of the reaction rate coefficients for the CO_2 splitting of ceria at 1773 K. Kinetic parameters were determined by minimizing the differences between experimental measurements of global reaction rates and model predictions for a small-scale, bench-top, isothermal packed bed reactor at 1773 K [15]. With reference to equations (16) and (19) of Chapter 4, the identified rate coefficients are $A_{\mathrm{ox}} = 1.5$ $\mathrm{mol_O\ mol_{ceria}^{-1}\ s^{-1}}$ and $k_{\mathrm{d,CO_2}} = 0.3$ $\mathrm{mol_{CO}\ mol_{ceria}^{-1}\ s^{-1}}$ at 1773 K. The reactor model was integrated with the heat exchanger model to iteratively establish the gas temperatures entering and leaving the numerical modeling domain.

Model results establish that the solar receiver/reactor design facilitates high absorption efficiency of 99.8% with almost half of the input power absorbed on the reactor tube surfaces. Effective radiative surface exchange evens out temperature differences in the reactor tubes undergoing reduction and oxidation. In the ceria particle bed, the spatial and temporal temperature distributions are predominantly influenced by radiation and convective heat transfer except a small region of the bed close to the gas inlet. Results showcase the role of the gases as carriers of thermal energy in addition to their primary role of delivering/carrying away the reactants/products. For a solar input power of 4.2 kW, selected gas flow rates of 0.67×10^{-4} mol s^{-1} g_{ceria}^{-1} and half-cycle times of 100 s, the volume- and time-averaged temperature of the indirectly irradiated ceria particles is 1791 K during reduction and 1792 K during oxidation. For the specified operating conditions, fuel is produced continuously at 0.1 μ mol s^{-1} g_{ceria}^{-1}, comparable to experimentally measured fuel production rate (0.09 μ mol s^{-1} g_{ceria}^{-1}). The fuel production rates are boosted by 12% for a more reflective cavity, owing to higher average ceria temperature (1799–1800 K), which promotes larger reduction extents. Spatial and temporal reaction rates and species concentration profiles reveal that the oxygen release/uptake by ceria depends largely on the stream wise rate of advection of the reactants and products.

Out of the total input power of 4.2 kW, an overall energy budget in the reactor suggests that the sensible heating load is almost 50% of the input power even with gas phase heat recuperation exceeding 90%, about 2 kW is lost as heat due to thermal radiation, conduction and convection, and 100 W is stored in the chemical bonds of CO. Projected solar to fuel efficiency is 0.9% (Chapter 4) that includes commercially relevant

estimates for producing, pumping and processing the effluents and product gases from the reactor. The elevated cost of sweep gas production, 5.7 kW, is at least an order of magnitude larger than the other parasitic energy requirements and reinforces the need to develop energy efficient technologies to produce pure N_2.

The developed model has served as a means to an end to explore the heat transfer–mass transfer–chemistry coupling in the reactor and connects the dots between experimental measurements to physically interpret the various transport processes. Results showcase that the reactor design, material morphology and the operating conditions have been suitably optimized to achieve highly effective gas utilization and gas phase heat recovery.

Future Work

The present work was limited to the determination of reaction rate coefficients at 1773 K and for one specific ceria morphology with an internal porosity of nearly 80% and specific surface area of 0.14 $m^2\ g^{-1}$. However, the methodology developed to extract reaction rate parameters is generally applicable to characterize chemical kinetics from globally measured reaction rates for packed bed/plug flow reactors with large spatial gradients in species concentrations and reaction rates. It would be valuable to the scientific community to estimate the activation energy and the temperature-cum-morphology dependence of the reaction rate coefficients by measuring global rates at other temperatures and for different ceria morphologies. In this way, the existing knowledge base for the chemical kinetics of pure ceria can be greatly improved.

In the current 3-D model of the reactor, convective airflow within the cavity has not been explicitly modeled. The developed model could be extended to include the

complete reactor with all the six reactive elements to obtain the temperature dependence of the convective heat losses. To the author's knowledge heat transfer correlations to determine convective losses in a cylindrical cavity with an array of circumferentially arranged cylinders are not available in the literature.

The computational models developed in this study (reactor and heat exchanger) are effective tools to investigate other solar thermal and thermochemical processes and new redox materials for renewable fuel production. The numerical framework would be especially valuable for physical processes with larger interdependencies of the transport and chemical processes taking place in the redox active material. An example application is the isothermal ceria redox cycle with methane driven reduction of ceria, as proposed by Krenzke et al. [115]. Based on thermodynamic analyses, at least an order of magnitude larger swing in nonstoichiometry is expected than the differences in ceria nonstoichiometry obtained with inert swept reduction. This implies larger impacts of the chemical energy sinks/sources on the transient variations of reactive material temperature. The model developed in this study is ideally suited to evaluate the coupled impacts of the heat and mass transport processes on the overall performance of such a physical system.

References

[1] U.S. Energy Information Administration, World Energy Statistics, 2012.

[2] Muhich C. L., Ehrhart B. D., Al-Shankiti I., Ward B. J., Musgrave C. B., and Weimer A. W., 2015, "A review and perspective of efficient hydrogen generation via solar thermal water splitting," Wiley Interdiscip. Rev. Energy Environ.

[3] Smestad G. P., and Steinfeld A., 2012, "Review: Photochemical and Thermochemical Production of Solar Fuels from H_2O and CO_2 Using Metal Oxide Catalysts," Ind. Eng. Chem. Res., **51**(37), pp. 11828–11840.

[4] Agrafiotis C., Roeb M., and Sattler C., 2015, "A review on solar thermal syngas production via redox pair-based water/carbon dioxide splitting thermochemical cycles," Renew. Sustain. Energy Rev., **42**, pp. 254–285.

[5] Wood D. A., Nwaoha C., and Towler B. F., 2012, "Gas-to-liquids (GTL): A review of an industry offering several routes for monetizing natural gas," J. Nat. Gas Sci. Eng., **9**, pp. 196–208.

[6] Subramani V., and Gangwal S. K., "A Review of Recent Literature to Search for an Efficient Catalytic Process for the Conversion of Syngas to Ethanol," Energy & fuels, **22**(2), pp. 814–839.

[7] Chueh W. C., and Haile S. M., 2010, "A Thermochemical Study of Ceria: Exploiting an Old Material for New Modes of Energy Conversion and CO_2 Mitigation.," Philos. Trans. A. Math. Phys. Eng. Sci., **368**(1923), pp. 3269–94.

[8] Eyring L., 1991, "The binary lanthanide oxides: synthesis and identification," Synthesis of lanthanide and actinide compounds, G. Meyer, and L.R. Morss, eds., Kluwer Academic Publishers, Dordrecht, The Netherlands, p. 201.

[9] Panlener R. J., Blumenthal R. N., and Garnier J. E., 1975, "A thermodynamic study of nonstoichiometric cerium dioxide," J. Phys. Chem. Solids, **36**(11), pp. 1213–1222.

[10] Lapp J., Davidson J. H., and Lipiński W., 2012, "Efficiency of two-step solar thermochemical non-stoichiometric redox cycles with heat recovery," Energy, **37**(1), pp. 591–600.

[11] Furler P., Scheffe J. R., and Steinfeld A., 2012, "Syngas Production by Simultaneous Splitting of H_2O and CO_2 via Ceria Redox Reactions in a High-temperature Solar Reactor," Energy Environ. Sci., **5**(3), pp. 6098–6103.

[12] Chueh W. C., Falter C., Abbott M., Scipio D., Furler P., Haile S. M., and Steinfeld A., 2010, "High-flux Solar-driven Thermochemical Dissociation of CO_2 and H_2O Using Nonstoichiometric Ceria.," Science, **330**(6012), pp. 1797–801.

[13] Furler P., Scheffe J., Marxer D., Gorbar M., Bonk A., Vogt U., and Steinfeld A., 2014, "Thermochemical CO_2 splitting via redox cycling of ceria reticulated foam structures with dual-scale porosities," Phys. Chem. Chem. Phys., **16**(22), p. 10503.

[14] Bader R., Bala Chandran R., Venstrom L. J., Sedler S. J., Krenzke P. T., De Smith R. M., Banerjee A., Chase T. R., Davidson J. H., and Lipinski W., 2015, "Design of a Solar Reactor to Split CO_2 Via Isothermal Redox Cycling of Ceria," J. Sol. Energy Eng., **137**(3), p. 031007.

[15] Venstrom L. J., De Smith R. M., Hao Y., Haile S. M., and Davidson J. H., 2014, "Efficient Splitting of CO_2 in an Isothermal Redox Cycle Based on Ceria," Energy & Fuels, **28**(4), pp. 2732–2742.

[16] Ermanoski I., Siegel N. P., and Stechel E. B., 2013, "A New Reactor Concept for Efficient Solar-Thermochemical Fuel Production," J. Sol. Energy Eng., **135**(3), p. 031002.

[17] Ermanoski I., 2014, "Cascading pressure thermal reduction for efficient solar fuel production," Int. J. Hydrogen Energy, **39**(25), pp. 13114–13117.

[18] Singh A. K., AuYeung N. J., Randhir K., Mishra R., Allen K., Petrasch J., and Klausner J., 2015, "Thermal reduction of iron oxide under reduced pressure and implications on thermal conversion efficiency for solar thermochemical fuel production," Ind. Eng. Chem. Res., p. 150610203735001.

[19] Brendelberger S., and Sattler C., 2015, "Concept analysis of an indirect particle-based redox process for solar-driven H_2O/CO_2 splitting," Sol. Energy, **113**, pp. 158–170.

[20] Krenzke P. T., and Davidson J. H., 2015, "On the Efficiency of Solar H_2 and CO Production via the Thermochemical Cerium Oxide Redox Cycle: The Option of Inert-Swept Reduction," Energy & Fuels, pp. 1045–1054.

[21] Lapp J., Davidson J. H., and Lipiński W., 2013, "Heat Transfer Analysis of a Solid-Solid Heat Recuperation System for Solar-Driven Nonstoichiometric Redox Cycles," J. Sol. Energy Eng., **135**(3), p. 031004.

[22] Lapp J., and Lipinski W., 2014, "Transient Three-Dimensional Heat Transfer Model of a Solar Thermochemical Reactor for H_2O and CO_2 Splitting Via Nonstoichiometric Ceria Redox Cycling," J. Sol. Energy Eng., **136**(3), p. 031006.

[23] Bader R., Venstrom L. J., Davidson J. H., and Lipiński W., 2013, "Thermodynamic Analysis of Isothermal Redox Cycling of Ceria for Solar Fuel Production," Energy & Fuels, **27**(9), pp. 5533–5544.

[24] Roeb M., and Sattler C., 2013, "Isothermal Water Splitting," Science (80)., **341**(6145), pp. 470–471.

[25] Hao Y., Yang C.-K., and Haile S. M., 2013, "High-temperature isothermal chemical cycling for solar-driven fuel production.," Phys. Chem. Chem. Phys., **15**(40), pp. 17084–92.

[26] Ermanoski I., Miller J. E., and Allendorf M. D., 2014, "Efficiency Maximization in Solar-Thermochemical Fuel Production: Challenging the Concept of Isothermal Water Splitting.," Phys. Chem. Chem. Phys., pp. 8418–8427.

[27] Furler P., and Steinfeld A., 2015, "Heat transfer and fluid flow analysis of a 4kW solar thermochemical reactor for ceria redox cycling," Chem. Eng. Sci.

[28] Keene D. J., Davidson J. H., and Lipiński W., 2013, "A Model of Transient Heat and Mass Transfer in a Heterogeneous Medium of Ceria Undergoing Nonstoichiometric Reduction," J. Heat Transfer, **135**(5), p. 052701.

[29] Keene D. J., Lipiński W., and Davidson J. H., 2014, "The effects of morphology on the thermal reduction of nonstoichiometric ceria," Chem. Eng. Sci., **111**, pp. 231–143.

[30] Bala Chandran R., Bader R., and Lipiński W., 2015, "Transient heat and mass transfer analysis in a porous ceria structure of a novel solar redox reactor," Int. J. Therm. Sci., **92**, pp. 138–149.

[31] Hathaway B. J., Bala Chandran R., Sedler S. J., Thomas D., Gladen A., Chase T. R., and Davidson J. H., 2015, "Effect of Flow Rates on Operation of a Solar Thermochemical Reactor for Splitting CO_2 via the Isothermal Ceria Redox Cycle," J. Sol. Energy Eng., **Submitted**.

[32] Garnier J. E., Blumenthal R. N., Panlener R. J., and Sharma R. K., 1975, "A thermodynamic study on CaO- doped nonstoichiometric cerium dioxide," Solid State Commun., **17**(10), pp. iv–v.

[33] Lapp J., Davidson J. H., and Lipiński W., 2012, "Efficiency of two-step solar thermochemical non-stoichiometric redox cycles with heat recovery," Energy, **37**(1), pp. 591–600.

[34] Hao Y., Yang C.-K., and Haile S. M., 2013, "High-temperature Isothermal Chemical Cycling for Solar-driven Fuel Production.," Phys. Chem. Chem. Phys., **15**(40), pp. 17084–92.

[35] Furler P., Scheffe J., Gorbar M., Moes L., Vogt U., and Steinfeld A., 2012, "Solar Thermochemical CO_2 Splitting Utilizing a Reticulated Porous Ceria Redox System," Energy & Fuels, **26**(11), pp. 7051–7059.

[36] McDonald C. F., 1980, "The Role of the Ceramic Heat Exchanger in Energy and Resource Conservation," J. Eng. Power, **102**(2), pp. 303–315.

[37] Lewinsohn C. A., Wilson M. A., Fellows J. R., and Anderson H. S., 2012, "Fabrication and Joining of Ceramic Compact Heat Exchangers for Process Integration," Int. J. Appl. Ceram. Technol., **9**(4), pp. 700–711.

[38] Smyth R., 1997, "The use of high temperature heat exchangers to increase power plant thermal efficiency," IECEC-97 Proceedings of the Thirty-Second Intersociety Energy Conversion Engineering Conference (Cat. No.97CH6203), IEEE, pp. 1690–1695.

[39] Sommers A., Wang Q., Han X., T'Joen C., Park Y., and Jacobi A., 2010, "Ceramics and ceramic matrix composites for heat exchangers in advanced thermal systems—A review," Appl. Therm. Eng., **30**(11-12), pp. 1277–1291.

[40] Li Q., Flamant G., Yuan X., Neveu P., and Luo L., 2011, "Compact heat exchangers: A review and future applications for a new generation of high temperature solar receivers," Renew. Sustain. Energy Rev., **15**(9), pp. 4855–4875.

[41] Ponyavin V., Chen Y., Mohamed T., Trabia M., Hechanova A. E., and Wilson M., 2012, "Design of a Compact Ceramic High-Temperature Heat Exchanger and Chemical Decomposer for Hydrogen Production," Heat Transf. Eng., **33**(10), pp. 853–870.

[42] Meschke F., and Kayser A., 2009, "Plate heat exchanger: Method for its production and its use."

[43] Schmidt J., Scheiffele M., Crippa M., Peterson P. F., Urquiza E., Sridharan K., Olson L. C., Anderson M. H., Allen T. R., and Chen Y., 2011, "Design, Fabrication, and Testing of Ceramic Plate-Type Heat Exchangers with Integrated Flow Channel Design," Int. J. Appl. Ceram. Technol., **8**(5), pp. 1073–1086.

[44] Munro R. G., 1997, "Material Properties of a Sintered α-SiC," J. Phys. Chem. Ref. Data, **26**(5), pp. 1195 – 1201.

[45] Jorgensen P. J., Wadsworth M. E., and Cutler I. B., 1961, "Effects of Water Vapor on Oxidation of Silicon Carbide," J. Am. Ceram. Soc., **44**(6), pp. 258–261.

[46] Warren J. M., 1972, "High temperature oxidation of Silicon carbide," Air Force Institute of Technology.

[47] Wang J., Zhang L., Zeng Q., Vignoles G. L., and Guette A., 2008, "Theoretical Investigation for the Active-to-Passive Transition in the Oxidation of Silicon Carbide," J. Am. Ceram. Soc., **91**(5), pp. 1665–1673.

[48] McDaniel A. H., 2012, Solar hydrogen production with a metal oxide-based thermochemical cycle.

[49] Lu W., Zhao C. Y., and Tassou S. A., 2006, "Thermal analysis on metal-foam filled heat exchangers. Part I: Metal-foam filled pipes," Int. J. Heat Mass Transf., **49**(15-16), pp. 2751–2761.

[50] Zhao C. Y., Lu W., and Tassou S. A., 2006, "Thermal analysis on metal-foam filled heat exchangers. Part II: Tube heat exchangers," Int. J. Heat Mass Transf., **49**(15-16), pp. 2762–2770.

[51] Yang C., Nakayama A., and Liu W., 2012, "Heat transfer performance assessment for forced convection in a tube partially filled with a porous medium," Int. J. Therm. Sci., **54**, pp. 98–108.

[52] Qu Z. G., Xu H. J., and Tao W. Q., 2012, "Fully developed forced convective heat transfer in an annulus partially filled with metallic foams: An analytical solution," Int. J. Heat Mass Transf., **55**(25-26), pp. 7508–7519.

[53] Modest M. F., 2003, "Approximate solution methods for one-dimensional media," Radiative Heat Transfer, Academic Press, pp. 451–456.

[54] Zhao C. Y., Lu T. J., Hodson H. P., and Jackson J. D., 2004, "The temperature dependence of effective thermal conductivity of open-celled steel alloy foams," Mater. Sci. Eng. A, **367**(1-2), pp. 123–131.

[55] Zhao C. Y., Lu T. J., and Hodson H. P., 2004, "Thermal radiation in ultralight metal foams with open cells," Int. J. Heat Mass Transf., **47**(14-16), pp. 2927–2939.

[56] Wu Z., Caliot C., Flamant G., and Wang Z., 2011, "Coupled radiation and flow modeling in ceramic foam volumetric solar air receivers," Sol. Energy, **85**(9), pp. 2374–2385.

[57] Hischier I., 2012, "Experimental and Numerical Analyses of a Pressurized Air Receiver for Solar-Driven Gas Turbines," J. Sol. Energy Eng., **134**(2), p. 021003.

[58] Bader R., Bala Chandran R., Venstrom L. J., Sedler S., Krenzke P., De Smith R. M., Banerjee A., Chase T. R., Davidson J. H., and Lipinski W., 2014, "Design of a Solar Reactor for Splitting CO2 Using Isothermal Redox Cycling of Ceria," J. Sol. Energy Eng.

[59] Banerjee A., Bala Chandran R., and Davidson J. H., 2015, "Experimental investigation of a reticulated porous alumina heat exchanger for high temperature gas heat recovery," Appl. Therm. Eng., **75**, pp. 889–895.

[60] Kaviany M., 1995, Principles of Heat Transfer in Porous Media, Springer-Verlag, New York.

[61] Patankar S., 1980, "Source-Term Linearization," Numerical Heat Transfer and Fluid Flow, M.A. Phillips, and E.M. Millman, eds., Hemisphere Publishing Corporation, pp. 143–145.

[62] ANSYS® Academic Research, 2011, "Ansys Fluent User Defined Functions Guide, Release 14.0."

[63] Markham J. R., Solomon P. R., and Best P. E., 1990, "An FT-IR based instrument for measuring spectral emittance of material at high temperature," Rev. Sci. Instrum., **61**(12), p. 3700.

[64] Hsu P., and Howell J. R., 1992, "Measurements of thermal conductivity and optical properties of porous partially stabilized zirconia," Exp. Heat Transf., **5**(4), pp. 293–313.

[65] Hendricks T. J., and Howell J. R., 1996, "Absorption/Scattering Coefficients and Scattering Phase Functions in Reticulated Porous Ceramics," J. Heat Transfer, **118**(1), pp. 79–87.

[66] Hale M. J., and Bohn M. S., 1992, "Measurement of the radiative transport properties of reticulated alumina foams," Conference: SOLAR `93: American Society of Mechanical Engineers (ASME)/American Solar Energy Society (ASES) joint solar energy conference, Washington, DC.

[67] Modest M. F., 2003, "The Method of Spectral Harmonics (PN-Approximation)," Radiative Heat Transfer, Academic Press, pp. 465–492.

[68] Bhattacharya A., Calmidi V., and Mahajan R., 2002, "Thermophysical properties of high porosity metal foams," Int. J. Heat Mass Transf., **45**(5), pp. 1017–1031.

[69] Calmidi V. V, 1998, "Transport phenomena in high porosity fibrous metal foams," University of Colorado Boulder.

[70] Ergun S., 1952, "Fluid flow through packed bed columns," Chem. Eng. Prog., **48**(2), pp. 89 –94.

[71] Lacroix M., Nguyen P., Schweich D., Pham Huu C., Savin-Poncet S., and Edouard D., 2007, "Pressure drop measurements and modeling on SiC foams," Chem. Eng. Sci., **62**(12), pp. 3259–3267.

[72] Wu Z., Caliot C., Bai F., Flamant G., Wang Z., Zhang J., and Tian C., 2010, "Experimental and numerical studies of the pressure drop in ceramic foams for volumetric solar receiver applications," Appl. Energy, **87**(2), pp. 504–513.

[73] Petrasch J., Meier F., Friess H., and Steinfeld A., 2008, "Tomography based determination of permeability, Dupuit–Forchheimer coefficient, and interfacial heat transfer coefficient in reticulate porous ceramics," Int. J. Heat Fluid Flow, **29**(1), pp. 315–326.

[74] Zukauskas A. A., 1987, "Convective heat transfer in cross-flow," Handbook of single-phase convective heat transfer, S. Kakaç, R.K. Shah, and W. Aung, eds., Wiley, New York.

[75] Wu Z., Caliot C., Flamant G., and Wang Z., 2011, "Numerical simulation of convective heat transfer between air flow and ceramic foams to optimise volumetric solar air receiver performances," Int. J. Heat Mass Transf., **54**(7-8), pp. 1527–1537.

[76] Bhattacharya, A., Calmidi V. V., and Mahajan R. L., 1999, "An Analytical-Experimental Study for the Determination of the Effective Thermal Conductivity of High Porosity Fibrous Foams," Application of Porous Media Methods for Engineered Materials, R.M. Sullivan, ed., pp. 13–20.

[77] Fourie J. G., and Du Plessis J. P., 2004, "Effective and coupled thermal conductivities of isotropic open-cellular foams," AIChE J., **50**(3), pp. 547–556.

[78] Schuetz M. A., and Glicksman L. R., 1984, "A Basic Study of Heat Transfer Through Foam Insulation," J. Cell. Plast., **20**(2), pp. 114–121.

[79] Coquard R., Loretz M., and Baillis D., 2008, "Conductive Heat Transfer in Metallic/Ceramic Open-Cell Foams," Adv. Eng. Mater., **10**(4), pp. 323–337.

[80] Kamiuto K., 2008, "Modeling of Composite Heat Transfer in Open-Cellular Porous Materials and High Temperatures," Cellular and Porous Materials: Thermal Properties Simulation and Prediction, A. Öchsner, G.E. Murch, and M.J.S. de Lemos, eds., Wiley-VCH Verlag GmbH & Co. KGaA, pp. 165–198.

[81] Yaws C., 2010, Transport Properties of Chemicals and Hydrocarbons:, Knovel, New York.

[82] Binnewies M., and Milke E., 2002, Thermochemical Data of Elements and Compounds, Wiley-VCH Verlag GmbH & Co. KGaA.

[83] ANSYS® Academic Research, 2013, "Ansys Fluent Users Guide, Release 15.0."

[84] Meier A., Bonaldi E., Cella G. M., Lipinski W., and Wuillemin D., 2006, "Solar chemical reactor technology for industrial production of lime," Sol. Energy, **80**(10), pp. 1355–1362.

[85] Häring H. W., 2008, "The Air Gases Nitrogen, Oxygen and Argon," Industrial Gases Processing, H.-W. Häring, ed., Wiley-VCH Verlag GmbH & Co. KGaA, Germany, pp. 9–109.

[86] Moran M. J., Shapiro H. N., Boettner D. D., and Bailey M. B., 2010, Fundamentals of Engineering Thermodynmics, Wiley.

[87] Mancini T., Heller P., Butler B., Osborn B., Schiel W., Goldberg V., Buck R., Diver R., Andraka C., and Moreno J., 2003, "Dish-Stirling Systems: An Overview of Development and Status," J. Sol. Energy Eng., **125**(2), p. 135.

[88] Banerjee A., Bala Chandran R., and Davidson J. H., 2015, "Experimental investigation of a reticulated porous alumina heat exchanger for high temperature gas heat recovery," Appl. Therm. Eng., **75**, pp. 889–895.

[89] Bala Chandran R., De Smith R. M., and Davidson J. H., 2015, "Model of an integrated solar thermochemical reactor/reticulated ceramic foam heat exchanger for gas-phase heat recovery," Int. J. Heat Mass Transf., **81**, pp. 404–414.

[90] Venstrom L. J., De Smith R. M., Hao Y., Haile S. M., and Davidson J. H., 2014, "Efficient Splitting of CO2 in an Isothermal Redox Cycle Based on Ceria," Energy&Fuels, **28**(4), pp. 2732–2742.

[91] Cussler E. L., 1997, Diffusion Mass Transfer in Fluid Systems, Cambridge University Press.

[92] Venstrom L. J., De Smith R. M., Bala Chandran R., Boman D. B., Krenzke P. T., and Davidson J. H. D., 2015, "Applicability of an equilibrium model to predict rates of reduction and oxidation in a fixed bed of cerium oxide," Energy & Fuels, **Submitted**.

[93] Abanades S., and Flamant G., 2006, "Thermochemical hydrogen production from a two-step solar-driven water-splitting cycle based on cerium oxides," Sol. Energy, **80**(12), pp. 1611–1623.

[94] James D. L., Siegel N. P., Diver R. B., Boughton B. D., and Hogan R. E., 2006, "Numerical Modeling of Solar Thermo-Chemical Water-Splitting Reactor," Solar Energy, ASME, pp. 221–227.

[95] Diver R. B., Miller J. E., Siegel N. P., and Moss T. A., 2010, "Testing of a CR5 Solar Thermochemical Heat Engine Prototype," ASME 2010 4th International Conference on Energy Sustainability, ASME, pp. 97–104.

[96] ANSYS® Academic Research, 2011, “Ansys Fluent Theory Guide, Release 15.0.”

[97] Raithby G. D., and Chui E. H., 1990, “A Finite-Volume Method for Predicting a Radiant Heat Transfer in Enclosures With Participating Media,” J. Heat Transfer, **112**(2), p. 415.

[98] Chui E. H., and Raithby G. D., 1993, “Computation of radiant heat transfer on a nonorthogonal mesh using the finite-volume method,” Numer. Heat Transf. Part B Fundam., **23**(3), pp. 269–288.

[99] Markham J. R., Solomon P. R., and Best P. E., 1990, “An FT-IR based instrument for measuring spectral emittance of material at high temperature,” Rev. Sci. Instrum., **61**(12), p. 3700.

[100] Krueger K. R., Lipiński W., and Davidson J. H., 2013, “Operational Performance of the University of Minnesota 45 kW e High-Flux Solar Simulator,” J. Sol. Energy Eng., **135**(4), p. 044501.

[101] Martinek J., and Weimer A. W., 2013, “Evaluation of finite volume solutions for radiative heat transfer in a closed cavity solar receiver for high temperature solar thermal processes,” Int. J. Heat Mass Transf., **58**(1-2), pp. 585–596.

[102] Murthy J. Y., and Mathur S. R., 1998, “Finite Volume Method for Radiative Heat Transfer Using Unstructured Meshes,” J. Thermophys. Heat Transf., **12**(3), pp. 313–321.

[103] Kaviany M., 1995, “Fluid Mechanics,” Principles of Heat Transfer in Porous Media, Springer-Verlag, New York, pp. 13–109.

[104] Hulst van de, and Christoffel H., 2012, Light scattering by small particles, Courier Dover Publications.

[105] Singh B. P., and Kaviany M., 1992, “Modelling radiative heat transfer in packed beds,” Int. J. Heat Mass Transf., **35**(6), pp. 1397–1405.

[106] Lee D.-Y., and Vafai K., 1999, “Analytical characterization and conceptual assessment of solid and fluid temperature differentials in porous media,” Int. J. Heat Mass Transf., **42**(3), pp. 423–435.

[107] Kaviany M., 1995, “Conduction Heat Transfer,” Principles of Heat Transfer in Porous Media, Springer-Verlag, New York, pp. 120–122.

[108] Zhang B.-M., Zhao S.-Y., and He X.-D., 2008, “Experimental and theoretical studies on high-temperature thermal properties of fibrous insulation,” J. Quant. Spectrosc. Radiat. Transf., **109**(7), pp. 1309–1324.

[109] Ganesan K., Dombrovsky L. A., and Lipiński W., 2013, "Visible and near-infrared optical properties of ceria ceramics," Infrared Phys. Technol., **57**, pp. 101–109.

[110] Ganesan K., and Lipiński W., 2011, "Experimental Determination of Spectral Transmittance of Porous Cerium Dioxide in the Range 900–1700 nm," J. Heat Transfer, **133**(10), p. 104501.

[111] "Alumina Insulation Type SALI-2" [Online]. Available: http://www.zircarceramics.com/pages/rigidmaterials/specs/sali2.htm.

[112] Bulfin B., Lowe A. J., Keogh K. A., Murphy B. E., Lübben O., Krasnikov S. A., and Shvets I. V., 2013, "Analytical Model of CeO_2 Oxidation and Reduction," J. Phys. Chem. C, **117**(46), pp. 24129–24137.

[113] Muhich C. L., Weston K. C., Arifin D., McDaniel A. H., Musgrave C. B., and Weimer A. W., 2015, "Extracting Kinetic Information from Complex Gas–Solid Reaction Data," Ind. Eng. Chem. Res., **54**(16), pp. 4113–4122.

[114] Toulukian Y., and Dewitt D., 1972, "Thermal Radiative Properties Nonmetallic Solids," New York, pp. 141–176.

[115] Krenzke P. T., and Davidson J. H., 2014, "Thermodynamic Analysis of Syngas Production via the Solar Thermochemical Cerium Oxide Redox Cycle with Methane-Driven Reduction," Energy & Fuels, **28**(6), pp. 4088–4095.